DISSERTATION

SINGLE MOLECULE FLUORESCENCE MEASUREMENTS OF COMPLEX SYSTEMS

Submitted by

Sanaz Sadegh

Department of Electrical and Computer Engineering

In partial fulfillment of the requirements

For the Degree of Doctor of Philosophy

Colorado State University

Fort Collins, Colorado

Summer 2017

Doctoral Committee:

Advisor: Diego Krapf

Michael Tamkun
Edwin Chong
Ashok Prasad

ABSTRACT

SINGLE MOLECULE FLUORESCENCE MEASUREMENTS OF COMPLEX SYSTEMS

Single molecule methods are powerful tools for investigating the properties of complex systems that are generally concealed by ensemble measurements. Here we use single molecule fluorescent measurements to study two different complex systems: $1/f$ noise in quantum dots and diffusion of the membrane proteins in live cells.

The power spectrum of quantum dot (QD) fluorescence exhibits $1/f^{\beta}$ noise, related to the intermittency of these nanosystems. As in other systems exhibiting $1/f$ noise, this power spectrum is not integrable at low frequencies, which appears to imply infinite total power. We report measurements of individual QDs that address this long-standing paradox. We find that the level of $1/f^{\beta}$ noise for QDs decays with the observation time. We show that the traditional description of the power spectrum with a single exponent is incomplete and three additional critical exponents characterize the dependence on experimental time.

A broad range of membrane proteins display anomalous diffusion on the cell surface. Different methods provide evidence for obstructed subdiffusion and diffusion on a fractal space, but the underlying structure inducing anomalous diffusion has never been visualized due to experimental challenges. We addressed this problem by imaging the cortical actin at high resolution while simultaneously tracking individual membrane proteins in live mammalian cells. Our data show that actin introduces barriers leading to compartmentalization of the plasma membrane and that membrane proteins are transiently confined within actin fences. Furthermore, superresolution imaging shows that the cortical actin is organized into a self-similar fractal.

ACKNOWLEDGEMENTS

First and foremost I want to express my sincere appreciation and gratitude to my thesis advisor Dr. Diego Krapf for the continuous support of my Ph.D study and related research, for his patience, motivation, and immense knowledge. Thank you for guiding me to grow as a research scientist.

I would also like to thank the rest of my thesis committee: Prof. Michael Tamkun, Dr. Ashok Prasad, and Prof. Edwin Chong, for their insightful comments and encouragement ans support.

I thank past and present members of Krapf group: Xinran Xu, Jenny Higgins, Aubrey Weigel, Bryce Schroder, Patrick Mannion and Kanti Nepal. The group has been a source of friendships as well as good advice and collaboration. I also thank Phil Fox, Liz Akin, Ben Johnson, Nasim Rad, Mahsa Ghorbani and Elaheh Alizadeh for the stimulating discussions, constant support and friendship.

Great thanks are also due to Leif Anderson for building this LaTeX document class, allowing me to meet the graduate school formatting requirements with no effort on my part.

Last but not the least, I would like to thank my family for all their love and encouragement. For my parents who raised me with love and supported me in all my pursuits. For the unconditional love and support of my brother and sister. And most of all for my loving, supportive, encouraging, and patient husband Farshad whose support during my Ph.D. is so appreciated. This accomplishment would not have been possible without them.

TABLE OF CONTENTS

LIST OF TABLES

LIST OF FIGURES

LIST OF ABBREVIATIONS

QDs	quantum dots	2
PSD	power spectral density	10
ER	endoplasmic reticulum	85
ER/PM	endoplasmic reticulum/plasma membrane	4
TIRF	total internal reflection	27
PALM	photo-activated localization microscopy	5
STORM	stochastic optical reconstruction microscopy	5
SPT	single particle tracking	68
SNR	signal to noise ratio	127
CTRW	continuous time random walks	43
fBM	fractional Brownian motion	43
GFP	green fluorescent protein	90
BFP	barrier-free path	68
ADRB2	adrenergic receptor beta-2	6

CHAPTER 1

INTRODUCTION

In the past few decades single molecule microscopy methods have evolved into extremely successful tools for revealing concealed properties and mechanisms in a broad range of complex systems throughout various scientific disciplines. These methods are particularly useful for analyzing stochastic processes where the state of individual molecules changes. For example, in cell biology, proteins transit between various folded and unfolded states [1, 2, 3], enzymatic reactions occur in multiple conformational sub-states [4, 5], trans-membrane proteins alter between different diffusive states [6, 7, 8], and many other multi-state stochastic phenomena happen, which all are crucial for proper cell functioning. Ensemble measurements, which study the average properties of systems, are unable to distinguish between subpopulations of single molecules in different states. Therefore we need single molecule measurements to identify, sort and study these subpopulations. Here we use single molecule methods to study two different systems which exhibit stochastic alternation between different states: $1/f$ noise in quantum dots with random switching between dark and bright states and diffusion of the membrane proteins in live cells which switches between different modes of motion.

We start with the definition of the $1/f$ noise and related long-standing non-integrability paradox. Then we discuss diffusion on the cell membrane and some of the potential components of cell that can effect the diffusion of the membrane proteins. Lastly, an overview of this thesis is given.

1.1. The $1/f$ noise in intermittent quantum dots

quantum dots (QDs) are very small semiconductor nanocrystals, a few nanometers in diameter, with interesting optical properties. Characteristics such as high photostability, brightness, size-tunable emission and excitation spectra and high quantum yield resulted in widespread applications of QDs ranging from light emitting diodes [9] to biological labeling [8]. QDs show random transitions between dark, "off", and bright, "on", states upon excitation (intermittency or "blinking"). It has been observed that the distribution of waiting times, or sojourn times, in theses states have a heavy tailed distribution which means the tail of the distribution is not exponentially bounded [10, 11, 12]. The underlying mechanism for the blinking phenomenon with power-law sojourn time remains unclear [13]. We are interested in characterizing the statistics of alternation between states which will eventually help us in understanding this heavily studied but still poorly understood system.

An important property of QD intermittency is that its power spectrum, in low frequencies, scales as

$$S(f) \sim \frac{A}{f^{\beta}}, \tag{1}$$

where f is frequency [14]. This type of spectrum, which is usually called $1/f$ noise or pink noise, appears in an extensively large array of physical signals. In fact, $1/f$ noise is so widespread that it is considered ubiquitous [15, 16, 17]. The integral of the power spectral density over a given frequency band computes the average power in the signal over that frequency band. Since the total power of a physical signal can not be infinite and, for $\beta \geq 1$, the power spectrum is not integrable, $\int_0^\infty S(f)\mathrm{d}f = \infty$, the existence of this type of noise is a paradoxical issue [16, 18]. Such behavior led to the suggestion that $1/f$ noise is related to non-stationary processes [15]. However, others dismiss these ideas, for example, by assuming that there exist some low-frequency cutoff f_c under which the non-integrable $1/f$ spectrum should not be observed [19]. Despite very long time measurements, the transition frequency could not been found [20, 21]. Further, measurements of $1/f$ noise in macroscopic systems, where a large number of subunits are intrinsically averaged, do not exhibit any evidence of non-stationarity [22, 23, 17], hence this famous paradox remains open.

In addition to non-integrability of the power spectrum, there is another open question regarding fluorescence intermittency of QDs and any other intermittent systems: theory predicts that the power spectrum of two-state systems with power-law sojourn times remains a random variable in the limit of long time measurements [18]. Thus large fluctuations should be observed between different power spectra of identical particles. Specifically, the distribution of PSD amplitudes converges to a Mittag-Leffler (ML) distribution. Nevertheless, the field is lacking experimental evidence for the predicted large fluctuations in these spectra.

1.2. Single molecule measurements in the plasma membrane of the cells

In mammalian cells, the surface consists of a lipid membrane that not only provides a boundary to enclose cell components, but also controls cellular intake and secretions, and organizes platforms that transmit environmental signals. The diffusive state of the cell membrane proteins can be altered by different mechanisms, including interaction with macromolecular complexes, bouncing against a barrier or getting captured by a well. For example, using single molecule methods, it has been observed that the outer or cortical layer of actin acts as a barrier for the diffusion of trans-membrane proteins, causing formation of transient protein clusters [24, 25, 26]. According to the "picket-fence" model, describing this type of behavior, the mobility of membrane-bound molecules is hindered by proteins anchored to the actin cytoskeleton [27], leading to their temporary confinement and anomalous diffusion [28, 29, 30]. The resulting organization of molecules into specific regions is beneficial for local interactions [31] and also alters diffusion-limited biochemical interactions [32, 33]. In spite of all the evidence that has accumulated over the last 20 years, a direct observation of the dynamic compartmentalization of membrane proteins by underlying actin fences is extremely challenging due to the spatial and temporal resolutions required for its visualization.

Another structure that could be an important player in the alteration of the diffusive dynamics of cell membrane proteins is the endoplasmic reticulum/plasma membrane (ER/PM) junction. In animal cells, ER is the primary storage site for intracellular Ca^{2+} that can be released as Ca^{2+} signals. The generation of Ca^{2+} signals is typically controlled by communication mechanisms between the ER and the surface of the cell, i.e., the plasma membrane (PM) [34]. As a consequence, endoplasmicER/PM contact sites are prevalent structures across different cell types, and they have essential functions in Ca^{2+} signaling and lipid trafficking [35]. The ER/PM junctions also function as trafficking hubs for insertion and removal of plasma membrane proteins suggesting a coupling mechanism between Ca^{2+} signals and protein traffic regulation [36]. Furthermore, it has been observed that the voltage gated potassium channel Kv2.1 aggregates and interacts with the endoplasmic reticulum, dramatically increasing ER/PM junction surface area and structurally changing the junction morphology [37]. Interactions of the potassium channel Kv2.1 with the ER/PM junctions on the cell membrane brings up an interesting question : whether other membrane proteins also interact with the ER/PM junctions.

1.3. Overview of this dissertation

In the second chapter we measure the power spectra of blinking QDs, namely we investigate individual nanoscale systems avoiding ensemble averaging. We address the fundamental question, whether the standard picture of blinking, found also in organic fluorophores, is characterized by a single exponent? We show that the description of QD power spectrum with a single exponent is incomplete since it hides rich physical phenomena. We also show that the power spectrum of blinking dots is nonstationary and ages with experimental time. Roughly speaking, the longer is the observation time, the level of noise decreases. More specifically, the power spectrum ages as t^{-z} where t is the measurement time and $z > 0$ is the aging exponent.

In the third chapter we report more analysis on $1/f$ noise in semiconductor QD fluorescence. We find that the power spectrum of their fluorescent emission remains a random variable even in long time experiments and its distribution converges to a function with finite width.

In chapter 4 we employ superresolution imaging and single-particle tracking of membrane proteins to elucidate the compartmentalization of the plasma membrane by intracellular structures. We track individual potassium channels and find that their diffusion pattern is best modeled by obstructed diffusion instead of fractional Brownian motion. We directly visualize the transient confinement of potassium channels by cortical actin in live cells. In order to characterize the cortical actin meshwork structure, we employ stochastic optical reconstruction microscopy (STORM) and photo-activated localization microscopy (PALM) to obtain superresolution images of the cortical actin in fixed and live cells. We find a non-integer dimension for the actin cortex and a broad distribution of compartment sizes as expected for a self-similar structure. These observations consistently explain the anticorrelated subdiffusive motion of membrane proteins and provide new insights on the hierarchical organization of the plasma membrane.

In chapter 5 we obtain a theoretical form for the MSD of diffusion in a distribution of compartment sizes assuming zero escape probability from the compartments. Then we calculate the MSD for three specific distributions of confinement sizes, namely exponential, power-law and log-normal distributions with linear (one dimensional) and circular (two dimensional) geometries. We also compare our theoretical results with simulations for validation. Finally, we argue that scale-free diffusion observed in several experiments can be explained by the broad distribution of the confinement sizes.

In the last chapter we study the regulation of the cortical actin-myosin meshwork and observed that the inhibition of the myosin proteins decreases the mobility of the Kv2.1/ER/PM junctions. Furthermore, using single particle tracking and imaging Kv2.1 enriched ER/PM junction, we show that two membrane proteins, adrenergic receptor beta-2 (ADRB2) (a G protein-coupled receptor that mediates cellular responses) and the glycoprotein CD4, aggregate at Kv2.1/ER/PM junctions.

CHAPTER 2

$1/F$ NOISE FOR INTERMITTENT QUANTUM DOTS EXHIBITS NONSTATIONARITY AND CRITICAL EXPONENTS

2.1. Introduction

The power spectrum of many natural signals exhibits $1/f$ noise at low frequencies [38, 39]. This noise appears in an extremely broad range of systems that includes electrical signals in vacuum tubes, semiconductor devices, and metal films [40, 23], as well as earthquakes [41], network traffic [42], evolution [43], and human cognition [44]. All these systems are characterized by a power spectrum of the universal form $S(f) \sim A/f^{\beta}$, where the exponent β is between 0 and 2 [40, 45, 46]. The long time that has passed from the first discovery of this phenomenon [47] led to multiple theories, competing schools of thought and many unresolved problems. One of the major problems lies in the fact that the spectrum is not integrable at low frequencies if $\beta > 1$, i.e., $\int_0^\infty S(f)\mathrm{d}f = \infty$. This is a paradoxical issue since the total power cannot be infinite, as implied by the divergence of the integral to infinity. In order to solve this paradox, Mandelbrot suggested that $1/f$ noises are related to non-stationary processes [40]. However, $1/f$ noise in macroscopic systems, where a large number of subunits are intrinsically averaged, do not exhibit evidence of non-stationarity [46], hence this famous paradox remains open. Moreover, these ideas have been often contested, for example, by assuming that there exist some low-frequency cutoff f_c under which the non-integrable $1/f$ spectrum is no longer observed. For this reason, several groups have increased

---

The work presented in this chapter has been performed in collaboration with Prof. Eli Barkai (Bar-Ilan University, Israel). Philip Fox and Elizabeth Akin helped me with imaging QDs in their TIRF setup (Tamkun laboratory,Colorado State University). This chapter has been published in New J. Phys. [48].

the measurement time in an attempt to find this evasive low-frequency cutoff. For example, spectral estimations have been obtained for one cycle in three weeks in operational amplifiers [49] and one cycle in 300 years in weather data [21]. Despite such long measurements, no low-frequency cutoff was found in these systems.

During the last two decades, experimental work has shown that $1/f$ noise is also observed in a vast array of nanoscale systems. For example, such noise was observed in individual ion channel conductivity [50, 51], electrochemical signals in nanoscale electrodes [52], biorecognition processes leading to the formation of a complex [53], and graphene devices [54]. Noise in nanoscale systems is particularly intriguing due to their sensitivity to environmental conditions. Furthermore, the characterization of noise properties in nanomaterials is an important challenge with direct applications in the stabilization of these materials for nanotechnology devices.

A well investigated but still poorly understood case is blinking in nanocrystals. These systems exhibit intermittency, namely random switching between dark and bright states, with sojourn times distributed according to power laws with heavy tails [55, 56, 57]. This power-law behavior was shown by Brokmann et al. [58] to induce unusual phenomena such as ergodicity breaking and non-stationary correlation functions, which are discussed here in the summary. Physical models underlying a power-law sojourn time distribution are based on distributed tunnelling mechanisms or diffusion controlled reactions [56, 59, 60]. Blinking dynamics is usually quantified with an exponent that describes the power law sojourn time (see details below). This characterization is obtained by thresholding the data in order to distinguish between “on” and “off” states. However, thresholding is sometimes scrutinized since the threshold value is rather arbitrary and hence a power spectral analysis is postulated to be a preferred tool [61, 62, 57]. Power spectrum is of course the most typical tool used to quantify noise.

Quantum dot (QD) intermittency has attracted considerable attention due to the intriguing optical properties of zero-dimensional materials as well as the power law statistics of "on" and "off" times [63, 59]. Due to the scale-free properties of power law statistics, intermittency naturally yields a power spectrum of the form $1/f^{\beta}$ [64]. In this report we measure the power spectra of blinking QDs, namely we investigate individual nanoscale systems avoiding ensemble averaging. We address the fundamental question, whether the standard picture of blinking, found also in organic fluorophores, is characterized by a single exponent? We show that the description of QD power spectrum with a single exponent is incomplete since it hides rich physical phenomena. Instead, the power spectrum of these systems is characterized by four exponents denoted β, z, ω, and γ and, importantly, we explain the physical meaning of these critical exponents. The power spectrum of blinking dots turns out to be unusual in the sense that it ages with experimental time. Roughly speaking, the longer is the observation time, the level of noise decreases. More specifically, the power spectrum ages as t^{-z} with $z > 0$ and t is the measurement time. In this sense, the power spectrum is non-stationary, in the spirit of Mandelbrot suggestion [40]. While the focus of this report is on blinking QDs, we believe that the underlying non-stationary behavior describes a large number of self-similar intermittent systems at the nanoscale, including to name a few, liquid crystals [65], biorecognition [53], nanoscale electrodes [52], and organic fluorophores [66].

2.2. Theoretical model

The simplest way to model intermittency is within the assumption of a two-state process. The QD switches between an active state where the intensity of the signal is I_0 to a passive state where the intensity is zero. This model is sketched in Fig. 2.1A. The sojourn times $\{\tau\}$ in states "on" and "off" are independent and identically distributed (i.i.d.) random variables with, for the sake of simplicity, a common probability distribution function $\psi(\tau) \sim \tau^{-(1+\alpha)}$. A particularly interesting situation arises when $0 < \alpha < 1$ because then the mean sojourn time diverges and thus the process lacks a characteristic time. Otherwise, for $\alpha > 1$, the mean sojourn time is finite. Diffusion controlled mechanisms of QD blinking lead to $\alpha = 1/2$, though measurements show deviations from this behavior, suggesting that a wider spectrum of exponents $1/2 < \alpha < 1$ is more suitable. For the two-state process, the system yields a power spectrum

$$S_t(f) \sim \frac{A_t}{f^{\beta}}, \tag{2}$$

with the exponent $\beta = 2 - \alpha$ when $0 < \alpha < 1$ [67, 68, 69, 70]. When the signal is measured over a finite experimental time t, the power spectral density (PSD) is typically estimated using the periodogram method,

$$S_t(f) = \tilde{I}(f,t)\tilde{I}(-f,t)/t, \tag{3}$$

where $\tilde{I}(f,t)$ is the Fourier transform of the intensity, $\tilde{I}(f,t) = \int_0^t I(\tau)\exp(-i2\pi f\tau)\mathrm{d}\tau$. Using this method, it was shown theoretically that the power spectrum decays with experimental time [69]. The time dependence of the spectrum can be found from simple scaling arguments. Because both states are assumed to be identically distributed, the total power is a constant. Thus,

$$\int_{1/t}^{\infty} S_t(f)\mathrm{d}f = A_t \frac{(1/t)^{-\beta+1}}{|\beta - 1|} = \text{const}, \tag{4}$$

where integration is performed from $1/t$, which is the lowest measured frequency. Therefore,

$$A_t \sim t^{-z} \tag{5}$$

with $z = \beta - 1$. Given the relation $\beta = 2 - \alpha$, we have

$$z = 1 - \alpha. \tag{6}$$

The exponent z is termed the aging exponent. The time dependence of the power spectrum reflects the non-stationarity of the process as it indicates that the longer the observation time, the smaller the amplitude of the power spectrum. In other words, the longer one observes the system, the QD gets trapped in longer and longer dark or bright states, thus the switching rate is effectively reduced and $1/f$ noise goes down. To the best of our knowledge, these predictions were not yet experimentally tested. This simple theoretical model bears non-negligible limitations in the analysis of QD intermittency. First, the system is assumed to consist of two identical states. Second, noise in the experimental system, beyond the switching events, is neglected [Fig. 2.1(a), (b)]. As we shall see in our results, these simplifications fail to capture some of the observed physics. However, these theoretical predictions are an excellent starting point in the analysis of blinking power spectrum.

2.3. Results

Figure 2.2(a) shows the first 600 seconds of the normalized intensity trace of a typical QD. Usually, QD blinking is analyzed by using a threshold that defines bright and dark states [55, 56, 58]. As mentioned, the threshold determination is rather arbitrary, and in that sense power spectrum analysis is preferred [62]. In agreement with previous observations,

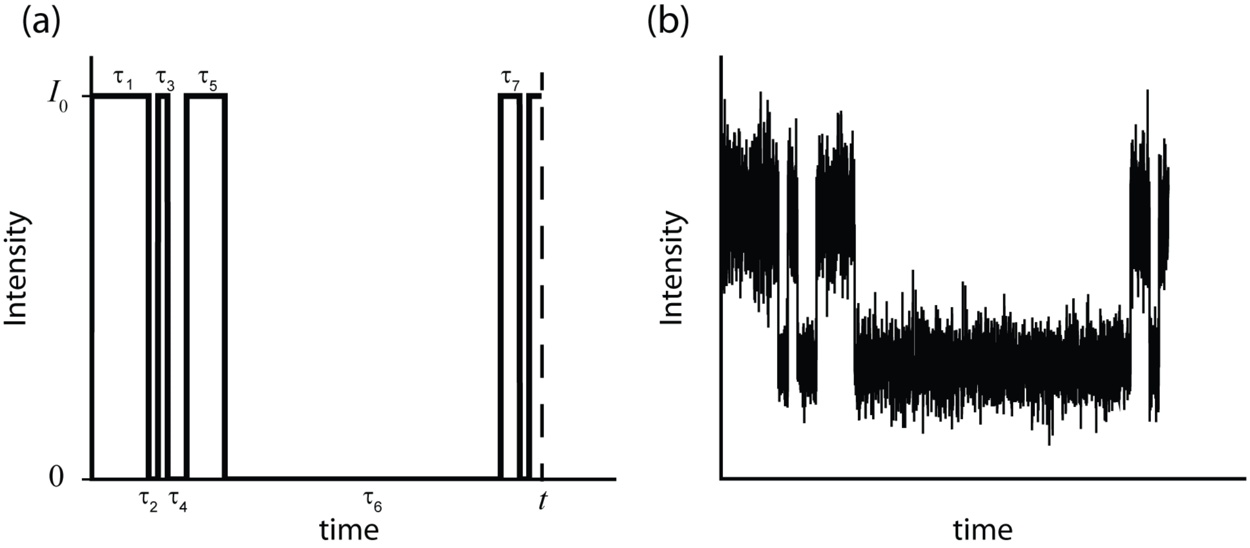

FIGURE 2.1. Simplified model for QD intermittency. (a) An individual QD alternates between states "on" and "off" with intensities I_0 and zero. The sojourn times are τ_j where j is respectively odd and even for "on" and "off" states. The measurement time is t. (b) Additional Gaussian noise in the "on" and "off" levels is depicted so that the intensity in these states is not constant but it fluctuates around the mean.

the distribution of "off" times is well described by a power law $\psi_{\text{off}}(\tau) \sim \tau^{-(1+\alpha)}$; whereas, the distribution of "on" times shows truncated power-law behavior $\psi_{\text{on}}(\tau) \sim \tau^{-(1+\alpha)} e^{-\tau/\tau_{\text{on}}}$ [56]. In our data we find $\alpha = 0.63 \pm 0.10$ and $\tau_{\text{on}} = 8.5$ s, a time scale that will soon become important.

A representative power spectrum from an individual QD is shown in Fig. 2.2(b). The experimental time of the time trace employed in the computation of this spectrum is 1311 s, i.e., the whole available time. Since the normalized intensity is dimensionless, the PSD has units of Hz^{-1}. Figure 2.2(c) shows power spectral densities obtained from averaging the spectra of $1,200$ individual QDs for experimental times of 10 and 1311 s. The spectrum of the long-time trace exhibits two regimes with distinctive $1/f^{\beta}$ behavior. For frequencies below a transition frequency f_T we have $S_t(f) \sim f^{-\beta_<}$ with $\beta_< = 0.76 \pm 0.02$ ($n = 1,200$ traces) while above this frequency we have $S_t(f) \sim f^{-\beta_>}$ with $\beta_> = 1.393 \pm 0.002$. The separation into two regimes is caused by the cutoff that characterizes the "on"-time distribution. Hence, the transition frequency f_T is, not surprisingly, of the order of $1/\tau_{\mathrm{on}}$. We will soon compare our experimental findings with the theory for $\beta_>$ and $\beta_<$, but let us first discuss the transition frequency.

2.3.1. The transition frequency f_T. The existence of a transition frequency implies that the measurement time is crucial. The PSD of the short-time trace (Fig. 2.2(c) with $t = 10$ s) displays $1/f^{\beta}$ spectrum with a single spectral exponent $\beta_>$. On the other hand, long enough measurements yield the transition to a different behavior. Importantly, an observer analyzing short-time traces would reach the conclusion that the power spectrum is non-integrable, since $\beta_> > 1$. If we wait long enough we eventually observe integrable $1/f$ noise, since $\beta_< < 1$. In some sense we are lucky to observe this transition: it is detected since the cutoff time τ_{on} is on a reasonable time scale.

Previously, Pelton et al. have reported a transition frequency in the power spectrum of blinking QDs [71]. However, that transition has a different nature from the one reported here. In our measurements, a cutoff in "on" sojourn times introduces a transition from $1/f^{2-\alpha}$ to $1/f^{\alpha}$ at low frequencies, i.e., long time behavior, with f_T of the order of 0.06 Hz. On the other hand, Pelton et al. find a high frequency transition, i.e., short time behavior, where the spectrum shifts from $1/f^{2-\alpha}$ to $1/f^{2}$ at frequencies above the transition. This high frequency transition was found to be of the order of 100 Hz. The transition to $1/f^{2}$ spectrum was interpreted as short time carrier diffusion yielding, at high frequencies, the power spectrum characteristic of Brownian motion [71].

2.3.2. Spectral exponents $\beta_<$ and $\beta_>$. Both exponents $\beta_<$ and $\beta_>$ are related to α. The exponents measured in this study are reported in Table 1 for the benefit of the reader.

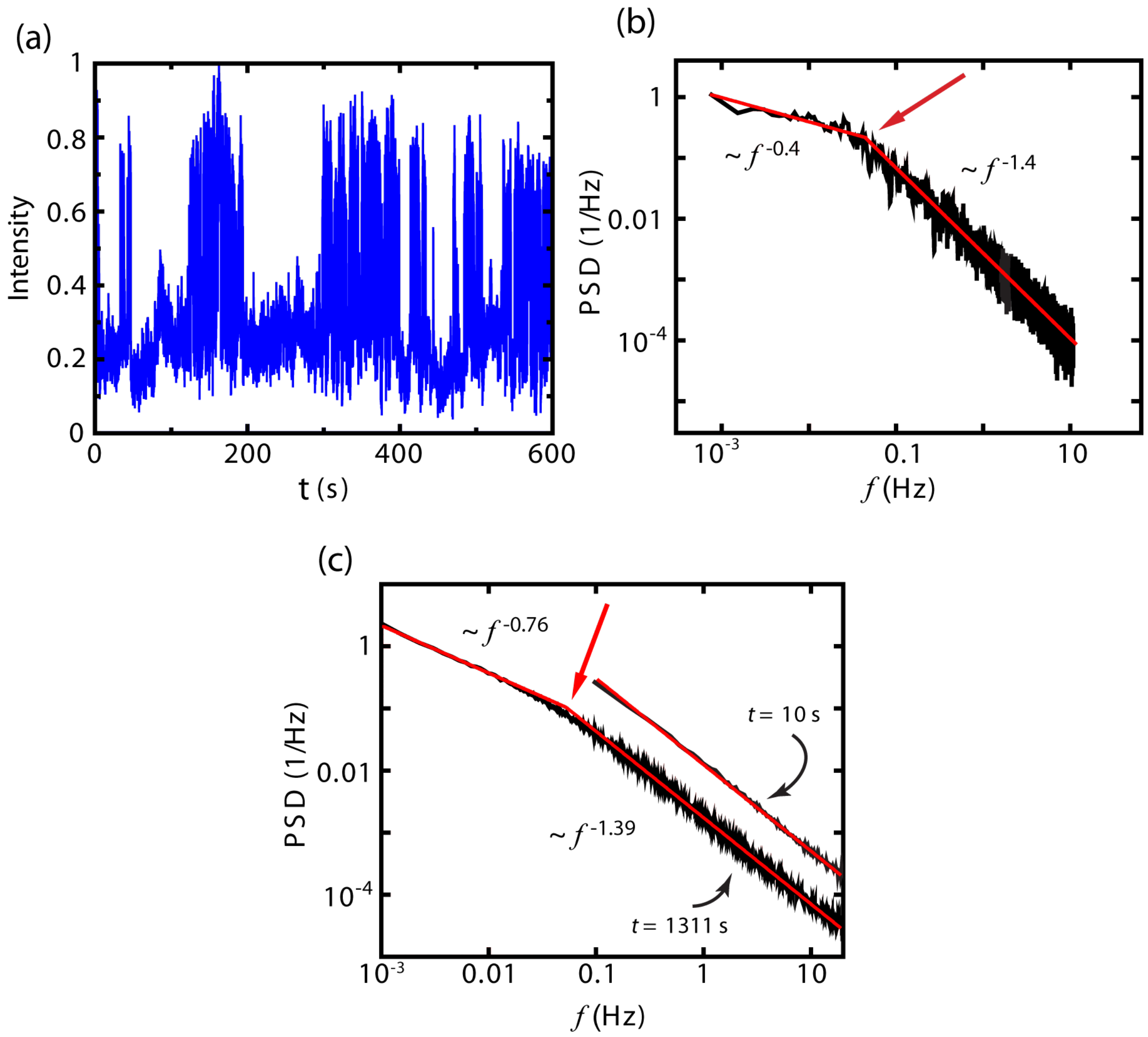

FIGURE 2.2. Power spectral density of QDs fluorescence emission. (a) Normalized fluorescence intensity of an individual CdSe-ZnS QD, i.e., maximum intensity is unity. (b) PSD of the emission from a single QD measured for 1311 s. (c) Average PSD from the emission of $1,200$ individual QDs. The experimental times are 10 and 1311 s. The short-time spectrum is shifted for clarity. The lines show linear regression of the log-log plot for high and low frequencies according to Eq. (2), and the red arrows point to the transition frequency f_T.

For frequencies $f > f_T$, the cutoff time is of no evident relevance and both states are effectively distributed with power law statistics $\psi(\tau) \sim \tau^{-(1+\alpha)}$. In this regime, theory predicts $\beta_> = 2 - \alpha$ as mentioned above. Since $\alpha = 0.63 \pm 0.10$, we expect $\beta_> = 1.37 \pm 0.10$,

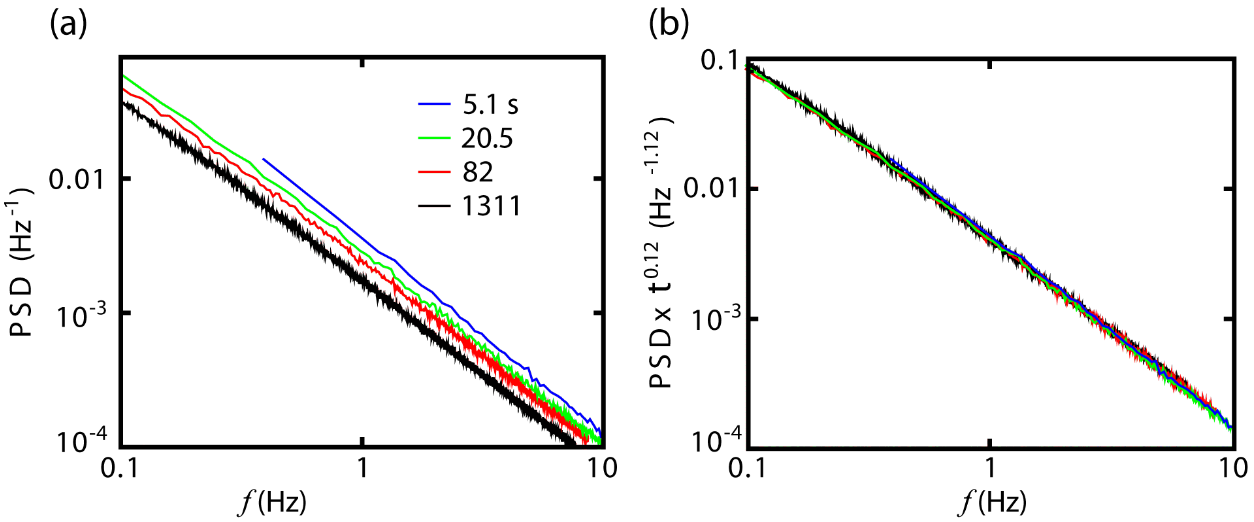

FIGURE 2.3. Aging of the power spectrum. (a) Average of 1200 QD power spectral densities for four different experimental times: 5.1, 20.5, 82, and 1311 s. (b) When the power spectral density is multiplied by an aging factor t^z with $z = 0.12$, where t is the experimental time, the spectra collapse to a single trace.

which is similar to the measured exponent. In contrast, for $f < f_T$ we must consider the effect of the cutoff time. Thus, we define a modified model, which includes a cutoff in the distribution of "on" times, so that the probability density functions of "on" and "off" sojourn times are different. The important feature of this model is that the mean "on" sojourn time is finite, which modifies the underlying exponents that describe the power spectrum. For this case, one finds $\beta_< = \alpha$. Experimentally we find $\beta_< = 0.76 \pm 0.02$ while $\alpha = 0.63 \pm 0.10$, so small deviations are found. The theoretical sum rule $\beta_< + \beta_> = 2$ is insensitive to the value of α provided that $\alpha < 1$, since this implies the divergence of the mean "off" sojourn time, which is the main condition for the observed self-similar behavior.

2.3.3. Aging exponent z. Since the "off" sojourn times are scale free, i.e., mean time is infinite, we expect the amplitude of the power spectrum A_t to depend on measurement time. Figure 2.3(a) shows averaged power spectra computed for trajectory lengths of 5.1, 20.5, 82, and 1311 s. As the experimental time t increases, the magnitude of the PSD is not constant but it decreases. To the best of our knowledge, this is the first experimental report explicitly showing that $1/f$ noise in nanoscale systems ages and the concept of stationary $1/f$ noise, so popular in a vast literature, breaks down. Figure 2.3(b) shows that the PSD data collapse to a single master trace when multiplied by $t^{0.12}$. According to the theory [69], the power spectrum amplitude scales as $A_t \sim t^{-z}$ with the exponent $z = 1 - \alpha$ both below and above the transition frequency. Thus we expect $z = 0.37 \pm 0.10$, which is slightly larger than the measured value of the aging exponent $z = 0.12$. We will address this deviation with simulations showing that additional noise in the "on" state (see Fig. 2.1) is important.

2.3.4. The zero frequency exponent ω. Next, we define the spectrum at zero frequency with

$$S_t(0) = S_t(f)|_{f=0} = \frac{(\int_0^t I(\tau) d\tau)^2}{t}, \tag{7}$$

and the corresponding exponent $S_t(f)|_{f=0} \sim t^{\omega}$. Notice that $S_t(0)/t$ is merely the square of the time average $\int_0^t I(\tau)\mathrm{d}\tau/t$ and its experimental evaluation does not require a fast Fourier transform. For stationary and ergodic processes with non-zero mean intensity we have normal behavior $\omega = 1$. On the other hand, if $\omega < 1$ the average intensity decays to zero. As shown in Fig. 2.4(a), our measurements yield $\omega \simeq 0.85$, which is a second indication of non-stationarity.

In our system, for long experimental times, the "on" time distribution displays a cutoff and thus the mean "on" time is finite. Therefore, the expected area under the intensity time trace can be estimated to be

$$\langle \int_0^t I(\tau)\mathrm{d}\tau \rangle = \langle n \rangle \tau_{\mathrm{on}} I_{\mathrm{on}}, \tag{8}$$

where I_{on} is the intensity in the "on" level and $\langle n \rangle$ is the average number of renewals up to time t, i.e., the number of switchings, which is known to increase as t^{α} for waiting "off" times distributed according to power laws [72, 73]. Hence we see that theoretically $S_t(f)|_{f=0} \sim t^{2\alpha-1} \simeq t^{0.26}$. Within this model, $\omega = 2\alpha - 1 = 0.26$. The measurements in Fig. 2.4(a) give $\omega = 0.85$, which is surprising since we expect that, at least for long times compared with τ_{on}, the cutoff in the "on" times dictate the behavior of the zero frequency spectrum. We will soon remove this mystery by detailed consideration of the effects of noise in the "on" and "off" states using numerical simulations. What becomes clear is that the standard description of blinking systems with a single exponent α, so popular in the literature, does not describe aging accurately and needs to be expanded. Namely, in our measurements, ω is not obtained from α in a straightforward way. Hence the standard picture of these systems is challenged.

2.3.5. The crossover frequency $f_c \sim t^{-\gamma}$. The transition between the zero frequency spectrum $S_t(0)$ and the small but finite frequency behavior $S_t(f) \sim f^{-\beta}$, defines a crossover or cutoff frequency f_c. A crossover frequency is many times assumed to be time independent, though its observation may require extremely long measurement times. For example, in spin glasses the inverse of the cutoff frequency was estimated to be of the order of age of the universe [46], and hence it cannot be directly investigated. Given that the PSD ages, we hypothesize the cuttoff frequency also changes with experimental time. We investigate the time dependence of f_c within our observation window, which is long in the sense that we measure thousands of transitions between "on" and "off" states. In order to estimate f_c, we extrapolate Eq. (2) to the intersection with the zero-frequency spectrum, given by Eq. (7), as shown in Figs. 2.4(b) and 2.4(c). According to the two state model with i.i.d. sojourn times,

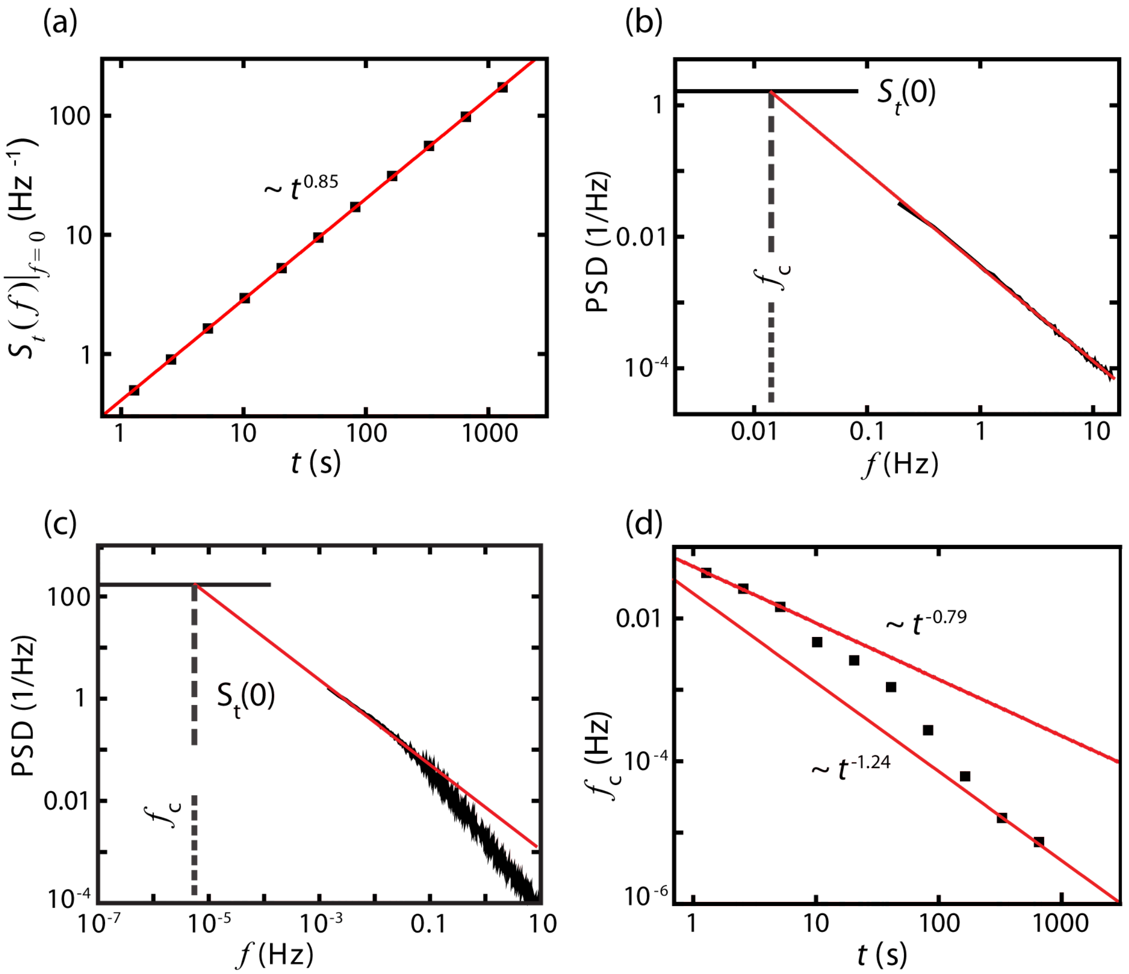

FIGURE 2.4. Additional critical exponents describing QD intermittency. (a) Zero-frequency spectrum vs. experimental time. (b-c) Examples showing how the crossover frequency f_c is found from the average power spectrum. The horizontal line shows $S_t(0) = S_t(f)|_{f=0}$. The crossover frequency f_c is found by extrapolating $S_t(f) \sim A_t f^{-\beta}$ to the intersection with $S_t(0)$. In b the experimental time is $t = 5.1$ s, thus $S_t(f) \sim A_t f^{-\beta_>}$. On the other hand, in c the time is $t = 1311$ s, thus the spectrum shows two different frequency regimes, with $S_t(f) \sim A_t f^{-\beta_<}$ for $f < f_T$. Note that f_c shifts by more than three orders of magnitude between 5.1 and 1311 s. (d) Crossover frequency vs. experimental time. We find that $S_t(0) \sim t^{\omega}$ with $\omega = 0.85$ and, for short times, $f_c \sim t^{-\gamma}$ with $\gamma = -0.79$.

$f_c \sim t^{-\gamma}$, and $\gamma = 1$ [69]. Again this behavior can be derived using scaling arguments. First, we use idealized models, which, by noting that at the crossover frequency $A_t f_c^{-\beta} = S_t(0)$, give $t^{-z} f_c^{-(2-\alpha)} \sim t$ for short times and $t^{-z} f_c^{-\alpha} \sim t^{2\alpha-1}$ for long times. Surprisingly, these scaling arguments predict $f_c \sim 1/t$ for all times, independent of τ_{on}. Hence, in this case

$\gamma = 1$. However, since we already observed deviations in ω and z from the idealized two-state model, we now use a more general approach using scaling arguments. Here, a second scaling approach relates the various exponents that characterize the process. As before, we employ the relation $A_t f_c^{-\beta} = S_t(0)$, which yields $t^{-z} f_c^{-\beta} \sim t^{\omega}$ from the definitions of the various critical exponents. Thus we find

$$\gamma = \frac{\omega + z}{\beta}. \tag{9}$$

Using measured values for ω, z, and β, we have $\gamma = 0.70$ for short times (see Table 1, $\omega = 0.85$, $z = 0.12$, and $\beta_{>} = 1.39$) and $\gamma = 1.27$ for long times ($\beta_{<} = 0.76$).

For short times, we observe in experiments that the crossover frequency scales with experimental time as $f_c \sim t^{-0.79}$ (Fig. 2.4(d)). Thus $\gamma = 0.79$, which is in good agreement with our general scaling argument approach (Eq. 9) and is consistent with the other critical exponent measurements. For longer measurement times, as seen in Fig. 2.2(c), the low frequency spectrum shifts from $S_t(f) \sim 1/f^{\beta_{>}}$ to $S_t(f) \sim 1/f^{\alpha}$ where $\beta_{>} > \alpha$. As a consequence of this effect, a transition is observed roughly on the cutoff time τ_{on} and f_c decays faster, namely, $\gamma > 1$ for $t > \tau_{\text{on}}$. The behavior can be qualitatively understood, by comparing Figs. 2.4(b) and 2.4(c). As the slope of the power spectrum becomes less steep, the crossover is rapidly shifted to smaller frequencies. The value for γ at long times is difficult to estimate from our measurements, but it is roughly $\gamma = 1.24$. Again, this value is consistent with the measured values of ω and z as predicted by scaling arguments (Eq. 9).

2.3.6. Numerical simulations. Deviations between experiments and theory can arise from at least three sources: experimental noise, finite measurement time, and model assumptions not being realistic. Recall that the models neglect any physical noise beyond the switching events (see Fig. 2.1A) and only attempt to solve for convergences in the long time limits. In particular, the intensity in the "on" and "off" states are not constant; the signal is always fluctuating. To address this issue we turn to numerical simulations. We estimated the four exponents β, ω, γ, and z based on numerical simulations. In simulations we add noise to the 0/1 signal (idealized model). Hence, simulations provide additional insight on the analysis. The performed simulations are: PL: Power law; PLN: Power law with noise; PLC: Power law with cutoff (truncated "on" times); and PLCN: Power law with cutoff and noise.

Initially, we generated time series of on/off states with random waiting times drawn from a power-law distribution $\psi(\tau) = \alpha t_0^{\alpha}/(\tau + t_0)^{-(1+\alpha)}$. The constant t_0 was chosen to be equivalent to the experimental binning time, $t_0 = 20$ ms, and $\alpha = 0.63$. We refer to this simulation as PL. In order to add Gaussian noise to the realizations (PLN), the "on" and "off" intensities were transformed at each sampling time into normal random variables $N(0.7, 0.04)$ and $N(0.2, 0.0064)$, respectively. The sampling time was chosen to be 20 ms. The variance difference reflects the increased level of noise in the "on" state due to shot noise. To simulate sojourn times distributed according to a power law with cutoff (PLC), the "on" times were drawn from a distribution $\psi(\tau) \sim \tau^{-(1+\alpha)}\exp(-\tau/\tau_{\text{on}})$ and $\tau \geq t_0$. The cutoff time was chosen to be $\tau_{\text{on}} = 15$ s. Additionally, we performed simulations with both cutoff "on" times and added noise (PLCN). Once noise is added the sojourn time distributions change and estimations of α and τ_{on} generally shift toward lower values. Therefore we chose $\tau_{\text{on}} = 15$ s in our simulations instead of 8.5 s as measured in experiments.

The combination of a cutoff time and Gaussian noise has significant effects on the zero-frequency spectrum $S_t(0)$ and the crossover frequency f_c [Fig. 2.5]. In these simulations, $f_c \sim t^{-\gamma}$ with $\gamma < 1$ at short times and $\gamma > 1$ at times $t > \tau_{\text{on}}$, as observed in the experimental

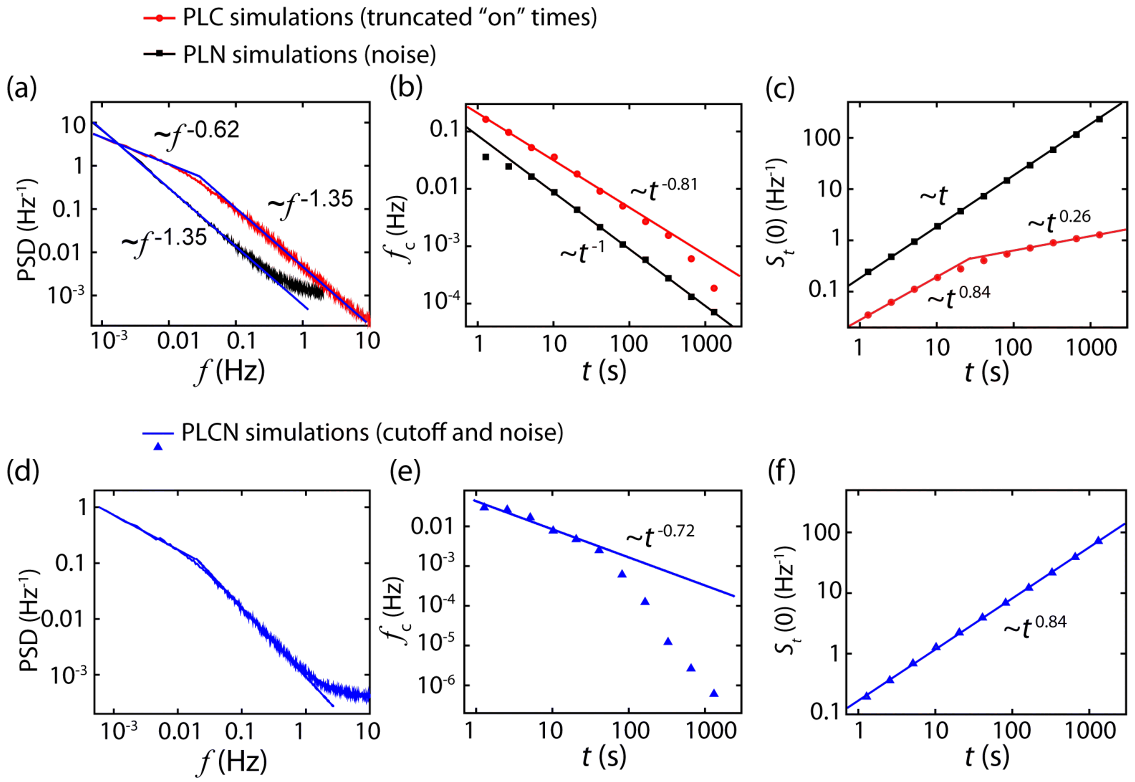

FIGURE 2.5. Numerical simulations. Three types of simulation results are shown: power law with noise (PLN), power law with cutoff (PLC), and power law with cutoff and noise (PLCN). (a) Average PSD for PLN and PLC. (b) Crossover frequencies f_c vs. realization time. (c) Zero-frequency spectra $S_t(f)|_{f=0}$ vs. realization time. The data corresponding to simulations with cutoff time are shifted down ten fold for clarity. (d) Average PSD for PLCN. (e) Crossover frequencies f_c vs. realization time. (f) Zero-frequency spectra $S_t(f)|_{f=0}$ vs. realization time.

data, and the zero frequency spectrum scales as $S_t(0) \sim t^{0.84}$ as well. Table 1 summarizes the exponents found in both experimental data and numerical simulations. Simulation results from a power law distributed two-state model with i.i.d. sojourn times and without noise (PL) are also shown in the Table along with this model's theoretical predictions. We observe that, while basic non-stationary features of $1/f$ noise agree with recent theory [69], our experimental work shows that introducing noise in the "on"/"off" levels and a finite mean "on" sojourn time is crucial for a complete picture of the power spectrum of blinking QDs.

TABLE 2.1. Exponents that describe $1/f$ noise for QD emission (experimental data) and simulations. Results from numerical simulations of two dichotomous random processes are shown: power-law distributed waiting times (PL) and power law with cutoff in "on" times and noise (PLCN). The exponents describe the power spectrum, aging, crossover frequency, and zero-frequency spectrum.

			Experimental data	Numerical simulations	
		Theory	QD	PL	PLCN
$\beta_>$	$S_t(f) \sim 1/f^{\beta}$	$\beta_> = 2 - \alpha$	1.39	1.38	1.35
$\beta_<$		$\beta_< = \alpha$	0.76	NA	0.62
z	$A_t \sim 1/t^{z}$	$z = 1 - \alpha$	0.12	0.36	0.31
γ	$f_c \sim 1/t^{\gamma}$	$\gamma = 1$	0.79[a]	0.99	0.72[a]
ω	$S_t(0) \sim t^{\omega}$	$\omega = 1$[b]	0.85	0.99	0.84

[a] These results hold for $t < \tau_{\text{on}}$. For longer times $\gamma > 1$.

[b] For long times we have $\omega = 2\alpha - 1$.

As seen in Table 2.1, the addition of noise and cutoff on the "on"-time distribution modifies the exponents in such a way that now we obtain better agreement between simulations and measurements. Jeon et al. discussed theoretically the strong influence of noise on the evaluation of physical parameters from data exhibiting power law distributed sojourn times [74]. While that work focused on diffusion of individual molecules in living cells, we can infer the relevance of noise also in our blinking system. Roughly speaking, when power law sojourn times are so broad, the system remains in a state (e.g, "off") for a time that is of the order of the measurement time. Therefore, the noise level in this long state is of utmost importance for a detailed analysis.

2.4. Discussion

Our data show that the power spectrum of blinking quantum dots crucially depends on measurement time. We present the first experimental evidence for Mandelbrot's suggestion that $1/f$ noise is related to non-stationary signals. Our measurements were performed at the nanoscale by measuring single particles, thus removing the problem of averaging a large number of particles, typically found in macroscopic systems. The most common description of macroscopic $1/f$ electronic noise, commonly referred to as the McWhorter model [54, 46], stems from the observation that a superposition of Lorentzian spectra with a broad distribution of relaxation times yield $1/f$ noise. If this philosophy would hold at the nanoscale, by probing an individual molecule, one would expect to measure a Lorentzian spectrum with a well-defined relaxation time. This scenario is not found for blinking quantum dots. Instead, $1/f$ is observed at the nanoscale. Further, the noise exhibits clear non-stationary behavior, i.e., dependence on measurement time. We quantify this non-stationarity with critical exponents. In particular, the aging exponent z shows that the amplitude of the noise decreases as a power law with time. This effect should also be found in other intermittent systems.

The key finding in our work shows that $1/f$ power spectrum of intermittent QDs decays with experimental time, i.e., it ages, and thus the spectrum does not converge in long time measurements as typically assumed for standard stochastic processes. These results agree with previous observations that analyzed blinking in semiconductor quantum dots as a non-stationary process [58, 75]. The description of non-stationary $1/f^{\beta}$ noise we present is vastly different from traditional approaches that characterize it with a single exponent. Besides β, three additional exponents give the dependence on the measurement time. These exponents describe aging of the power spectrum $A_t \sim t^{-z}$, the zero-frequency spectrum $S(f)|_{f=0} \sim t^{\omega}$, and the low cutoff frequency $f_c \sim t^{-\gamma}$. Importantly, the appearance of a transition frequency due to a finite mean "on" sojourn time, modifies the underlying exponents that describe the power spectrum.

In an observation time t, the total power of the process is $\int_{1/t}^{\infty} S_t(f)\mathrm{d}f$ where $1/t$ is the lowest measured frequency. For a process with power spectrum $S(f) = A/f^{\beta}$ with $1 < \beta < 2$

the total power diverges as time increases, due to the low frequency behavior. In contrast, if $S(f) = A/f^{\beta}$ and $0 < \beta < 1$, the total power diverges due to the high frequency behavior of the spectrum. We observe that in QDs, two different phenomena limit the increase of total power. First, below the transition frequency f_T, we find $\beta < 1$ due to the cutoff in the "on" sojourn times and hence the spectrum is integrable at low frequencies. For large frequencies $\beta > 1$ hence it is integrable also at high frequencies. Second, as the observation time progresses, the amplitude of the power spectrum decreases with $A_t \sim t^{-z}$, so that $S_t(f) \to 0$ in the limit $t \to \infty$. Both these findings maintain the total power finite. More precisely, if one measures for times that are shorter than τ_{on} and hence the transition to an integrable spectrum is not detected at low frequencies, the decrease of the spectrum with time ensures that the total area under the power spectrum does not diverge. This will become particularly important in the limit of weak laser field excitation and low temperatures, where τ_{on} becomes extremely large [56] and a single regime in the power spectrum holds for all observable time scales, i.e., the transition frequency f_T is not observed within the available frequency range. We measure the total power by integrating the power spectral density as defined above and indeed, we obtain a finite value which is not diverging, i.e. it is bound, though convergence is slow (Fig. 2.6). The aging of the spectrum ensures that total power of the system will not diverge, hence, our observations help in removal of a long-standing paradox of physics [40].

By resorting to numerical simulations, we find that a model that includes both a cutoff in "on" sojourn times and noise in each state (PLCN model) describes more accurately the experimental results obtained. These simulations emphasize the influence of noise within the "on" and "off" states and power low with a cut-off distribution. However, the value of the aging exponent z still remains somewhat far from our experimental observations. The aging

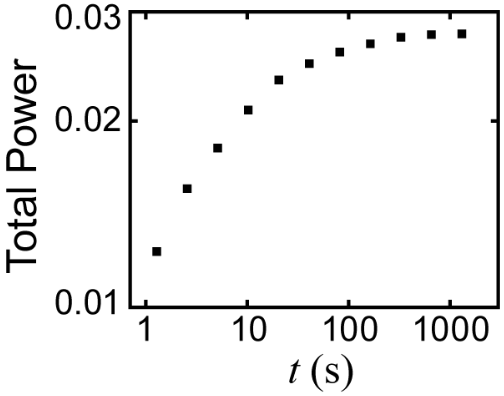

FIGURE 2.6. Total power vs. experimental time in blinking QDs. The total power is found by integrating over the power spectrum $\int_{1/t}^{\infty} S_t(f)\mathrm{d}f$. The power increases to a finite value, showing that the total power is bounded.

exponent in simulations is estimated to be $z = 0.31$, while in experiments $z = 0.12$. We can speculate there are two reasons responsible for the observed discrepancy. First, these models still assume the existence of solely two levels. Recent experiments point to the existence of intermediate states in the emission from core-shell QDs [76, 77]. The occurrence of multiple states has been described both in terms of blinking processes that are faster than the time resolution of the experiment (as is the case in our experiments) [78] and in terms of multiple physical states within the core-shell quantum dot [77, 79]. Nevertheless, the main aspects of the non-stationarity described here are expected to hold for the multiple level system as long as at least one of the states is governed by a scale-free power law distribution. Second, a different phenomenon that could affect the measured critical exponents is noise in the QD levels that is not Gaussian. The influence of non-Gaussian noises can of course have striking consequences in the properties of a stochastic process.

In our approach the exponents were analyzed in a way that is reminiscent of critical behavior, with scaling relations showing the exponents are dependent on each other and with different behaviors below and above a transition frequency $f_T \simeq 1/\tau_{\text{on}}$. These results are relevant to a broad range of systems displaying power law intermittency [80, 81, 65, 53, 52].

Further, power law sojourn times, which is the basic ingredient leading to the observed non-stationary spectrum in blinking quantum dots, are widespread and are found in glassy systems [82, 83] and anomalous diffusion in live cell environments and other complex systems [84, 85, 86, 87, 88]. Therefore, the measured exponents could be a general feature of many noisy signals. Finally, the traditional characterization of blinking quantum dots with a single exponent α is shown to be limited and to hide interesting physics described by different critical exponents.

2.5. Conclusions

Our experiments show how the analysis of noise in blinking quantum dots reveals rich physical behavior described by four critical exponents. This is vastly different from traditional approaches that characterized power spectrum of $1/f^{\beta}$ noise with a single exponent β. The exponent z describes the aging of the spectrum with measurement time, showing a decrease of the noise level as the measurement time increases. The exponent β describes the $1/f^{\beta}$ noise as in many previous studies, however we find two such exponents $\beta_{<}$ and $\beta_{>}$, below and above the transition frequency f_T. The zero frequency exponent ω describes the time average of the intensity, which is essentially related to ergodicity and yields further information on the non-stationarity of the process. The exponent γ describes the crossover from zero frequency to $1/f^{\beta}$. We hope that our work will promote measurements of exponents of $1/f^{\beta}$ spectrum, since they reveal the true complexity of the observed phenomena.

2.6. Experimental methods: quantum dot imaging

Core-shell CdSe-ZnS quantum dots were purchased from Life Technologies (Qdot 655, Invitrogen). In order to avoid aggregation, the QDs were dispersed in a 1% (w/v) bovine serum albumin solution to a final concentration of 1 nM. A 20-μL drop of this solution was placed on a glass coverslip (Warner Instruments, Hamden, CT) that had been cleaned by sonication in acetone and ethanol. After a 10-minute incubation period the coverslip was thoroughly rinsed with deionized water and dried with nitrogen. We recorded the fluorescence from 1,200 QDs for 22 min at room temperature in a Nikon Eclipse Ti total internal reflection (TIRF)/widefield fluorescence microscope. QDs were excited by a 488-nm laser line and the emission was collected with a bandpass filter. Images were acquired in a frame-transfer electron multiplying charge-coupled device (EMCCD iXon DU-897, Andor, Belfast UK) at 50 frames per second (exposure time of 20 ms).

QD intensities were measured using an automated algorithm implemented in LabView, which computes the total intensity of each QD. Due to spatial inhomogeneities in excitation power and dot-to-dot variations in quantum yield, different QDs can have varying fluorescence intensities. Thus, we normalize the data so that all intensities lie between zero and one, allowing us to work with a more convenient dimensionless intensity system. For this purpose, we first subtract the minimum value of the intensity along each QD trace and then divide it by the maximum (after subtraction) intensity value.

CHAPTER 3

FLUCTUATIONS OF $1/F$ NOISE IN INTERMITTENT QDS

3.1. Introduction

In the previous chapter we showed that the PSD of QD emission exhibits aging and the ensemble averaged PSD depends on experimental time, in agreement with theoretical predictions for the non-stationarity of $1/f$ spectra in intermittent systems. Also we observed two regimes with different $1/f$ behavior for frequencies greater or less than a transition frequency f_T. The existence of a transition frequency is due to the cutoff in the "on"- time distribution. Both regimes exhibit $1/f^{\beta}$ with $\beta > 1$ for $f > f_T$ and $\beta < 1$ for $f < f_T$. Given that $\beta < 1$ for low frequencies the spectrum is integrable and the non-integrability paradox of $1/f$ noise is solved.

We observed that the sojourn times of QD emission is power-law distributed. Power-law statistics lead to diverging moments and, therefore, the time-averaged observables remain random variables in the long time limit. Theory predicts that the power spectrum of two-state systems with power-law sojourn times also remains a random variable in the limit of long measurements [18]. Thus large fluctuations should be observed between different power spectra of identical particles. Nevertheless, the field is lacking experimental evidence for the predicted large fluctuations in these spectra.

In this chapter we report experiments on $1/f$ noise in semiconductor QD fluorescence. We find that the power spectrum of their fluorescent emission remains a random variable even in long time experiments and its distribution converges to a function with finite width.

The work presented in this chapter has been performed in collaboration with Prof. Eli Barkai (Bar-Ilan University, Israel).

3.2. Results

Similar to chapter 2, the core-shell CdSe/Zns nanocrystals (Qdot 655, Invitrogen) were deposited on glass coverslips and excited by a 488-nm laser line. We recorded the room temperature fluorescence from 470 QDs for long times (22 min) at 50 frames per second. Due to spatial variations, different QDs can have varying intensities while they are in the on state. For normalization purposes, we first subtract the minimum value of the intensity along each QD trace and then divide it by the maximum (after subtraction) intensity value. This procedure assures all intensities lie between zero and one. Figure 3.1(a) shows the first 10 s of the normalized intensity trace of five individual QDs. Both "on" and "off" states are accompanied by experimental noise with non-negligible contributions to the power spectrum. In order to study the component of the PSD originating from transitions between "on" and "off" states, we thresholded the intensity of QD emission and considered each time trace as a sequence of zeros and ones such that $I_2(t) = 1$ if $I(t) \geq I_{\mathrm{th}}$ and $I_2(t) = 0$ if $I(t) \leq I_{\mathrm{th}}$[89]. In chapter 2 we used an arbitrary threshold value, but here we apply a more sophisticated method in order to evaluate the threshold value. As shown in Fig. 3.2, we fitted two Gaussian to the histogram of individual QD normalized intensities, which are usually two overlapping normal distributions centered at "on" or "off" levels, then we chose the threshold to be the intersection point of these two Gaussian. Figure 3.1(b) shows the thresholded intensity traces for the same QDs shown in Fig. 3.1(a). The distribution of "off" times derived by this method is well described by a power law $\psi_{\mathrm{off}}(\tau) \sim \tau^{-(1+\alpha_1)}$; whereas, the distribution of "on" times shows truncated power-law behavior $\psi_{\mathrm{on}}(\tau) \sim \tau^{-(1+\alpha_2)} e^{-\tau/\tau_{\mathrm{on}}}$. For our data, 470 QDS, we found $\alpha_1 = 0.64$, $\alpha_2 = 0.5$ and $\tau_{\mathrm{on}} = 5.5$ s [Fig. 3.3(a), (b)].

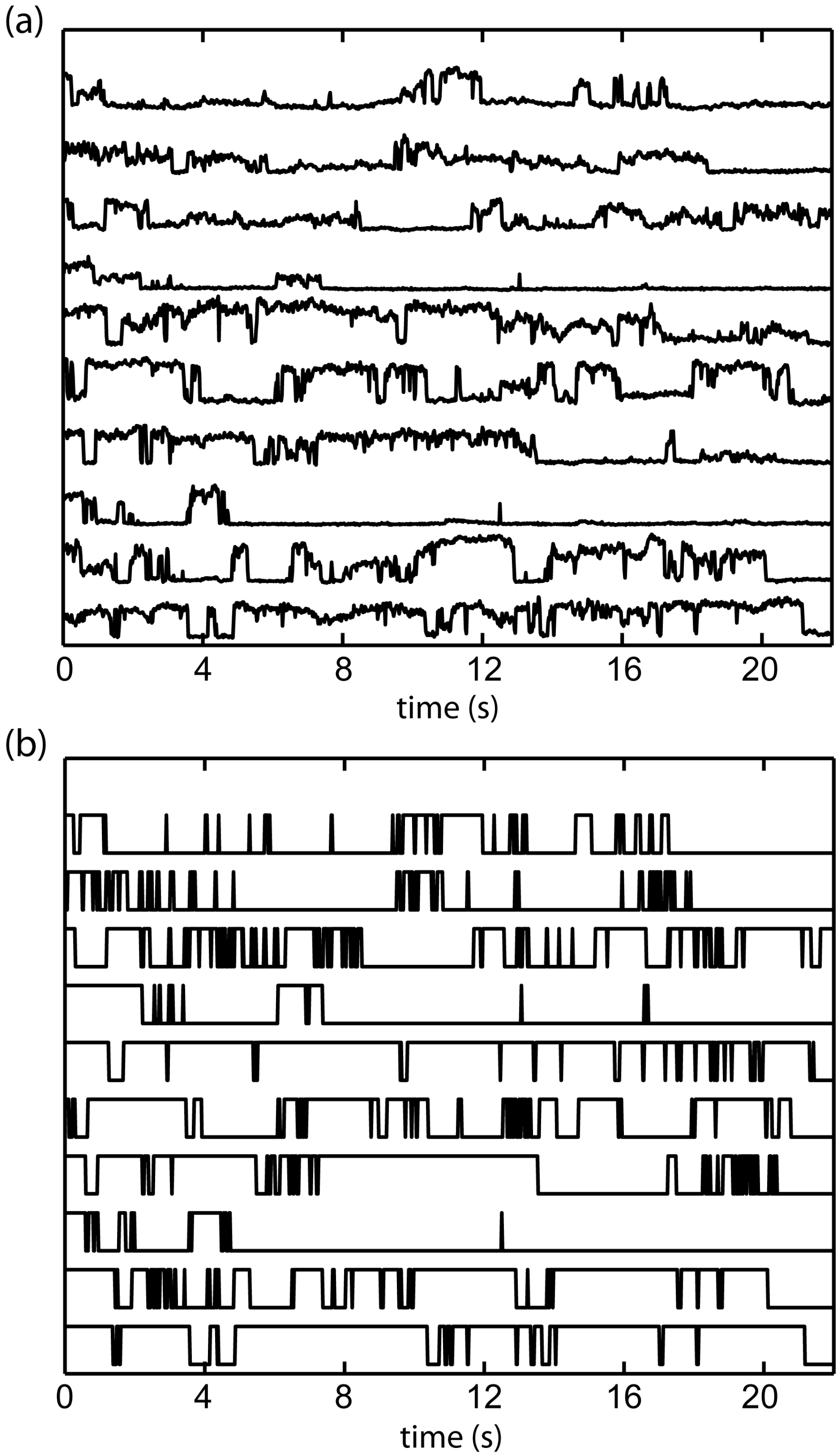

Figure 3.1. Intensity of individual QD fluorescence emission. (a) Fluorescence intensity from five individual quantum dots as a function of time. All intensities are between zero and one and are shifted by a constant value. (b) Time series of the same five QDs after thresholding the intensities.

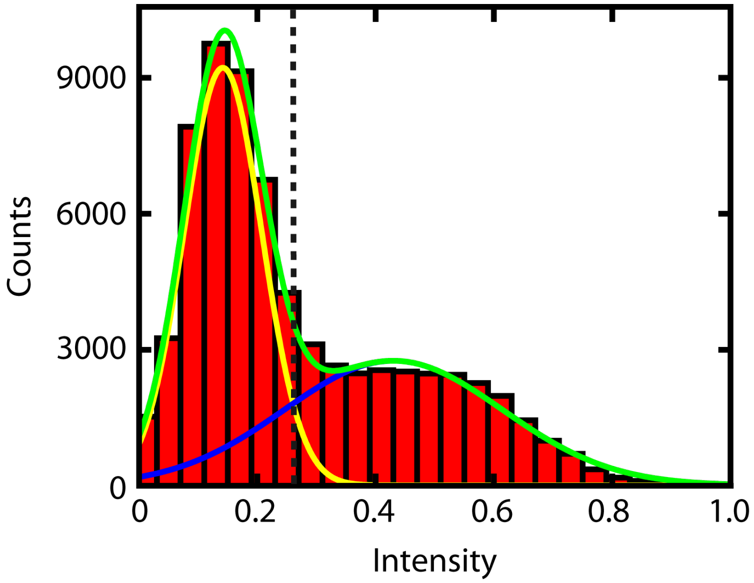

Figure 3.2. Thresholding the intensity of QDs fluorescence emission. Histogram of normalized intensities of one QD fluorescence emission with two Gaussian fits, the threshold has chosen to be the intersection point of these two Gaussian (black dashed line).

Since, similar to chapter 2, signal is measured over a finite experimental time t, the PSD is estimated using Eq. 3. We observed two regimes of PSD with different $1/f$ behavior for frequencies greater or less than a transition frequency f_T [Fig. 3.4(a)]. This result is in agreement with our previous observations shown in the chapter 2. Both regimes exhibit $1/f^{\beta}$ with $\beta > 1$ for $f > f_T$ and $\beta < 1$ for $f < f_T$. Although the PSDs of different QDs have similar exponents for two regimes, their amplitudes exhibit a broad scatter [Fig. 3.4(b), (c)]. The high frequency domain exponents in all measured 470 QD traces are observed to be similar with a mean $\beta = 1.41$ and a standard deviation 0.06 and for low frequencies the average exponent is $\beta = 0.89$ with a standard deviation 0.32 [Fig. 3.4(d)].

For ergodic systems individual PSDs converge to the ensemble-averaged PSD in the long time limit. In our measurements, the amplitude of the PSD shows large fluctuations. In order to investigate these fluctuations, we consider the amplitude A of the PSD, $S(f) = A/f^{\beta}$, and we examine the distribution of the PSD amplitude, A, and also the normalized PSD

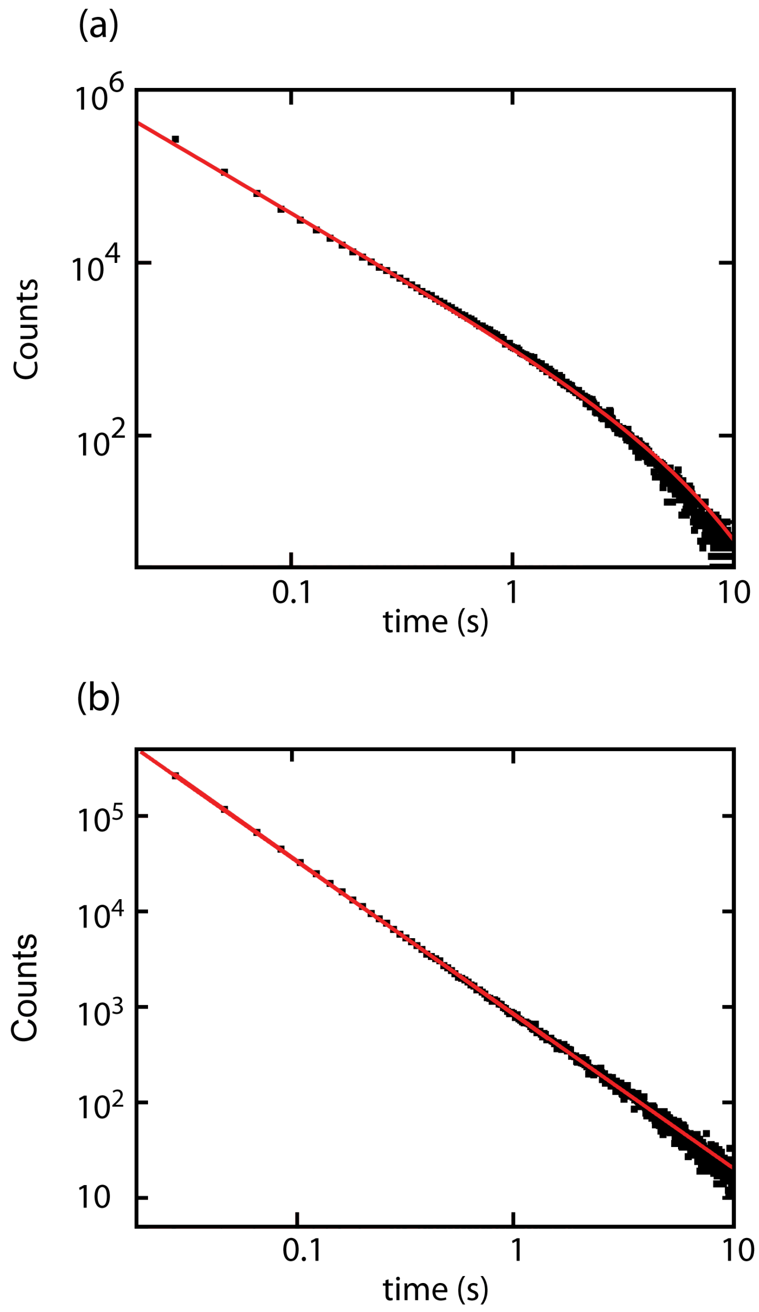

FIGURE 3.3. Distribution of sojourn times. (a) Distribution of "on" times for 470 QDs. The red line shows the following fit: $\psi_{\text{on}}(\tau) \sim \tau^{1.5} e^{-\tau/5.5}$. (b) Distribution of "off" times for 470 QDs. The red line shows the following fit: $\psi_{\text{off}}(\tau) \sim \tau^{-1.64}$.

amplitude $\xi = A/\langle A \rangle$, where the angle brackets represent ensemble average. To estimate A in the low and high frequency regime, we select the section of the PSD before and after the transition frequency respectively. As shown in Fig. 3.5(a) and (b) , we observe a broad

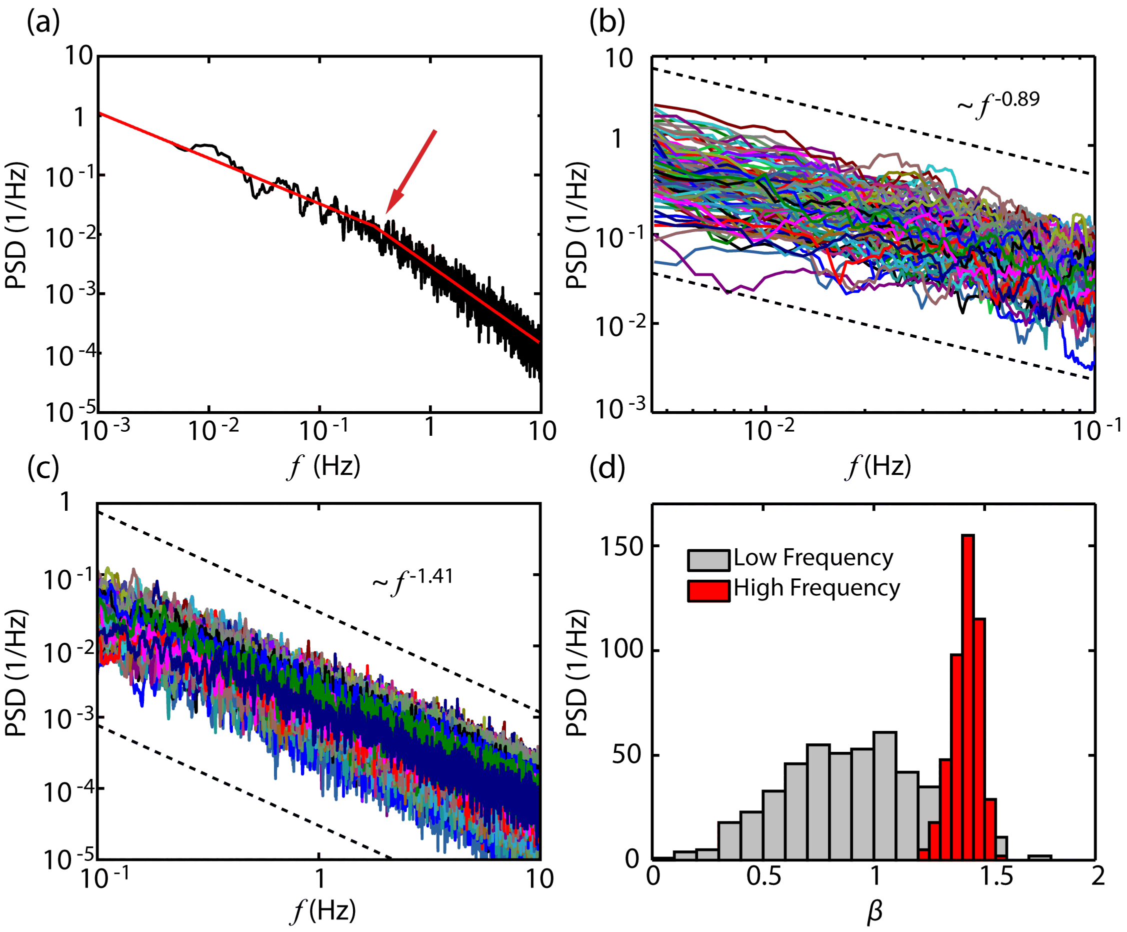

FIGURE 3.4. Variations of power spectral density of QDs fluorescence emission. (a) PSD of the emission from a single QD. The red lines show linear regression of the log-log plot for high and low frequencies, and the arrow points to the transition frequency f_T (b) Power spectral density of the 100 individual QDs at low frequency region ($f < f_T$) calculated for experimental time: 1311 s. (c) Power spectral density of the same 100 individual QDs at high frequency region ($f > f_T$) calculated for experimental time: 1311 s. (d) Distribution of the exponent of PSD of individual QDs fluorescence emission, β, calculated for high and low frequency regimes.

distribution of PSD amplitudes for both regimes. We also looked at the distribution of the PSD amplitude for different measurement times. If the process were ergodic, the PDF of ξ would converge to a delta-function centered at one by increasing the measurement time. However, as shown in Fig. 3.5(c), the distribution of normalized PSD amplitudes for high frequency regime converges to a distribution with finite variance, which is a consequence of weak ergodicity breaking. Since transition to low frequency regime only happens for long

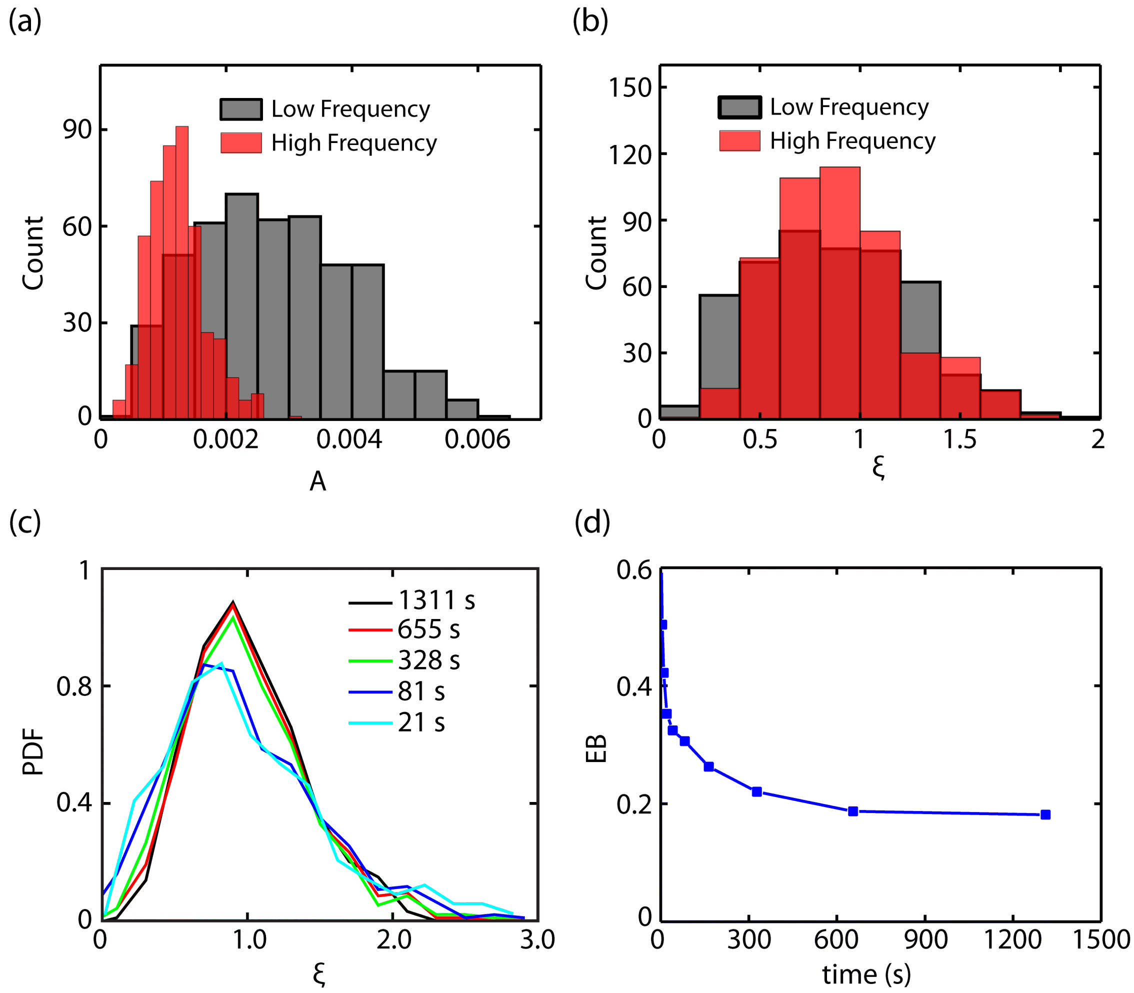

Figure 3.5. The spectra of different quantum dots scatter broadly. (a) Histogram of the PSD amplitude, A, of QDs intensity traces calculated for experimental time: 1311 s, for low and high frequency regimes. Each count is computed from the spectrum of a single quantum dot trace. (b) Histogram of the normalized PSD amplitude, $\xi = A/\langle A \rangle$, calculated for experimental time: 1311 s, for low and high frequency regimes. (c) Histogram of the normalized PSD amplitude, measured over different experimental times (d) Ergodicity breaking parameter, Eq. 10, as a function of experimental.

measurements, $t > 500s$, we were not able to look at the amplitude distribution convergence for the low frequency regime.

The variance of the distribution of ξ is usually called the ergodicity breaking (EB) parameter [90]

$$\mathrm{EB} = \frac{\langle A^2 \rangle - \langle A \rangle^2}{\langle A \rangle^2}. \tag{10}$$

Figure 3.5(d) shows that the EB parameter first decreases with time and then converges to a finite value. It has been shown that for a one dimensional CTRW with power-law waiting times, $\psi \propto \tau^{-(1+\alpha)}$, the EB parameter is related to the power-law exponent, α, by

$$\mathrm{EB} = \frac{2\Gamma^2(1+\alpha)}{\Gamma(1+2\alpha)} - 1, \tag{11}$$

where $\Gamma(z)$ is the gamma function [90]. For the distribution of the amplitudes of the power spectrum of QDs, we have $\mathrm{EB} = 0.41$ for $\alpha = 0.63$. Our experimental results show the EB parameter converges to $\mathrm{EB} \simeq 0.18$.

Furthermore, it has been shown that the distribution of ξ for a renewal process with power-law sojourn times, $\psi \propto \tau^{-(1+\alpha)}$, converges to a Mittag-Leffler (ML) distribution :

$$(\xi_1, \xi_2, ..., \xi_n) \to Y_\alpha(\eta_1, \eta_2, ..., \eta_n) \tag{12}$$

where the η_i are independent random variables with a unit mean and the pre-factor Y_α is a random variable of normalized Mittag-Leffler distribution with exponent α whose moments are $\langle Y_\alpha^n \rangle = n!\Gamma(1+\alpha)^n/\Gamma(1+n\alpha)$. We observe in our experimental results that the distributions of $A/\langle A \rangle$ can not be approximated by ML distribution [Fig. 3.6] and, the α value for closest ML distribution, $\alpha = 0.82$, is different than theoretical prediction, which is 0.64 for our case.

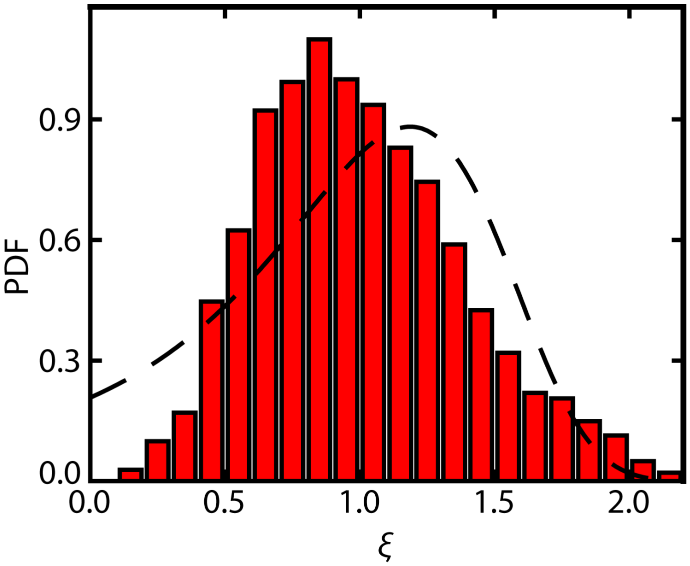

Figure 3.6. Distribution of normalized amplitude of PSD. Distribution of normalized amplitude of PSD for 1311 s total experimental time. Dashed line is the closest ML distribution with $\alpha = 0.82$.

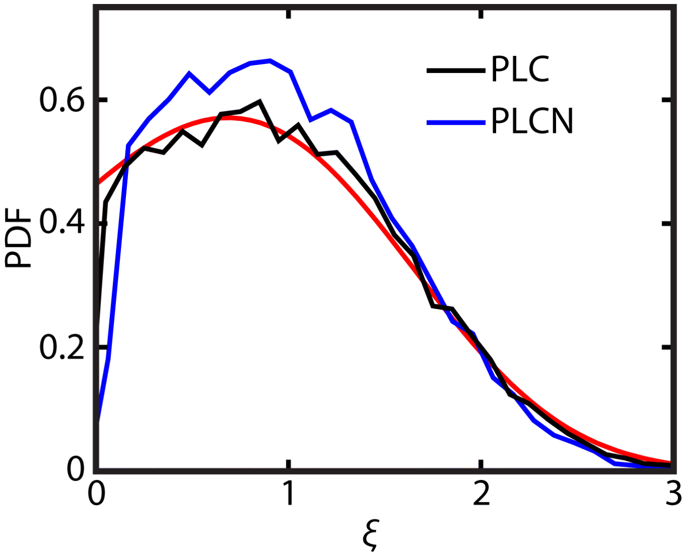

Figure 3.7. Normalized PSD amplitude of numerical simulation. Histogram of the normalized PSD amplitude of 1311 s time trace for two simulated models. In the first model, the "on" times are exponentially truncated. In the second model Gaussian noise is added to each realization of the first model. Histogram of the normalized PSD amplitude of 1311 s time trace for both models. The red line shows the Mittag-Leffler distribution for $\alpha = 0.63$.

As mentioned before, both "on" and "off" levels are accompanied by Gaussian noise [Fig. 3.3(b)]. Also the "on" times distribution is not a power-law and has an exponential cutoff. We hypothesized that the Gaussian noise and/or cutoff in waiting times can explain the observed deviation from theoretical predictions. In order to study the extent of Gaussian noise in $1/f$ fluctuations, we compare our experimental results to simulations that include the effects of truncation in the sojourn times and noise. In the simulation (power law with cutoff, PLC), the "on" times were drawn from a distribution $\psi(\tau) \sim \tau^{-(1+\alpha)}\exp(-\tau/\tau_{\mathrm{on}})$ with $\tau_{\mathrm{on}} = 15$ s and the "off" times were drawn from a power-law distribution with $\alpha = 0.63$. In the second case, we performed simulations with cutoff and added Gaussian noise to each point in the time series (PLCN). For PLC, the distribution of ξ converges to ML distribution with $\alpha = 0.63$ [Fig. 3.7] indicating that the truncation in the sojourn times of one of the states does not alter distribution of fluctuations of $1/f$ noise. This is expected because the "off" times are power law distributed and thus the process is scale-free for times longer than the truncation time. For PLCN, some deviations from theoretically predicted ML distributions are observed, albeit these deviations are much smaller than those seen in [Fig. 3.5(b)]. These results suggest that simple Gaussian noise or cutoff of the "on" times cannot explain the discrepancies between experiment and the theory of intermittent two state processes. Thus non-Gaussian noise effects are assumed to cause the observed discrepancies. Non-Gaussian noise may be in part caused by binning. The smallest dwell time is usually orders of magnitude smaller than the exposure time, which results in averaging over several "on" and "off" times and, in turn, generates artificial intermediate states.

3.3. Discussion

In summary, by considering the QDs intermittent fluorescence as a system with power law distributed sojourn times showing $1/f$ noise, we observed weak ergodicity breaking in $1/f$ noise. We find that the power spectrum of their fluorescent emission remains a random variable even in long time experiments and its distribution converges to a function with finite width. Our data indicates that deviations of the EB parameter from theoretically predicted value and distribution of PSD amplitude from ML can not be explained by simple Gaussian noise in the on/off levels.

CHAPTER 4

THE PLASMA MEMBRANE IS COMPARTMENTALIZED BY A SELF-SIMILAR CORTICAL ACTIN MESHWORK

4.1. Introduction

The plasma membrane is a complex fluid where lipids and proteins continuously interact and generate signaling platforms in order to communicate with the outside world. One of the key mechanisms by which membrane molecules search reaction sites is based on lateral diffusion. Quantitative imaging methods, such as single-particle tracking [91, 30, 92], spatiotemporal image correlation spectroscopy [93], fluorescence correlation spectroscopy (FCS) [94, 95], and STED-FCS [96], show that the dynamics of proteins and lipids in the plasma membrane often deviate from normal diffusion. In particular, the mean square displacement (MSD) does not grow linearly in time as expected for Brownian motion [97, 98, 99, 100]. This behavior suggests processes that hinder diffusion. Since the formation of protein complexes is governed by diffusion-mediated encounters, hindered diffusion plays fundamental roles in cell function.

Unveiling the underlying mechanisms leading to the observed anomalous diffusion on the cell membrane is critical to understanding cell behavior. Anomalous diffusion in the plasma membrane can be caused by macromolecular crowding [102], transient binding [86], heterogeneities [103, 104], and membrane compartmentalization by the underlying cytoskeleton

---

The work presented in this chapter has been performed in collaboration with Prof. Michael Tamkun (Colorado State University). Jenny Higgins initially worked on this project. She performed the initial experiments which some of the results are used here, she also wrote several codes for data analysis and developed some of the experimental protocols. Patrick Mannion helped with experiments and data analysis. Kv2.1 and Kv1.4 plasmids used in this project were provided by Tamkun lab (Colorado State university). PALM reconstruction code was provided by Dr. Keith Lidke (University of New Mexico). Dr. Maxime Dahan (Institut Curie, Paris) provided the plasmids to express ABP-tdEos. This chapter has been published in Phys. Rev. X [101]

[105, 30]. In recent years it has become evident that a single mechanism cannot account for the complex dynamics observed in the plasma membrane [100]. It has been shown that interactions with clathrin coated pits (CCPs) cause anomalous diffusion and ergodicity breaking [86, 106]. However, it was observed that this process coexisted with a different anomalous diffusion mechanism attributed to diffusion within a fractal topology. Experimental evidence for the organization of the plasma membrane by the cortical actin cytoskeleton has been provided by measurements in cell blebs, spherical protrusions that lack actin cytoskeleton [107], and in the presence of actin-disrupting agents [25, 26, 108]. The picket-fence model explains these observations by postulating that the mobility of membrane-bound molecules is hindered by the actin-based cytoskeleton in close proximity to the plasma membrane, leading to transient confinement [27, 28, 29, 30]. Confinement and segregation of membrane components can have important physiological properties in allowing the formation of functional domains on the cell surface. However, in spite of the vast evidence that has accumulated over the last two decades, a direct observation of the dynamic compartmentalization of membrane proteins by underlying actin fences is challenging due to the spatial and temporal resolutions required for its visualization.

Here we employ superresolution imaging and single-particle tracking of membrane proteins to elucidate the compartmentalization of the plasma membrane by intracellular structures. We track individual potassium channels and find that their diffusion pattern is best modeled by obstructed diffusion instead of fractional Brownian motion. We directly visualize the transient confinement of potassium channels by cortical actin in live cells. In order to characterize the cortical actin meshwork structure, we employ stochastic optical reconstruction microscopy (STORM) to obtain superresolution images of the cortical actin in fixed cells. We find a non-integer dimension for the actin cortex and a broad distribution of compartment sizes as expected for a self-similar structure. These observations consistently explain the anticorrelated subdiffusive motion of membrane proteins and provide new insights on the hierarchical organization of the plasma membrane.

4.2. Results

4.2.1. Kv1.4 and Kv2.1 ion channels undergo subdiffusion in the plasma membrane.

Voltage-gated potassium channels Kv1.4 and Kv2.1 were expressed in human embryonic kidney (HEK) cells, labeled with quantum dots (QDs) [86], and imaged using total internal reflection fluorescence (TIRF) microscopy at 50 frames/s, so that individual molecules could be detected on the cell surface. Kv1.4 and 2.1 are similar in size, 654 and 853 amino acids, respectively, but share less than 20% overall amino acid identity [109]. They are placed into distinct gene subfamilies because of this low identity. They are most similar within a central core domain composed of six transmembrane alpha helices and the ion conducting pore. In contrast, they share no amino sequence identity within the cytoplasmic N- and C-terminal regions; each Kv1.4 subunit has 402 cytoplasmic amino acids while the Kv2.1 subunits have 624. Both channels exist as homotetrameric structures giving the functional channel 24 membrane spanning domains and a total of either 1608 or 2496 cytoplasmic amino acids. Figure 4.1(a) shows representative trajectories of Kv1.4 channels. The motion of the ion channels was initially evaluated in terms of their time-averaged MSD,

$$\overline{\delta^2(\Delta)} = \frac{1}{T-\Delta}\int_0^{T-\Delta} |\mathbf{r}(t+\Delta) - \mathbf{r}(t)|^2 \mathrm{d}t, \tag{13}$$

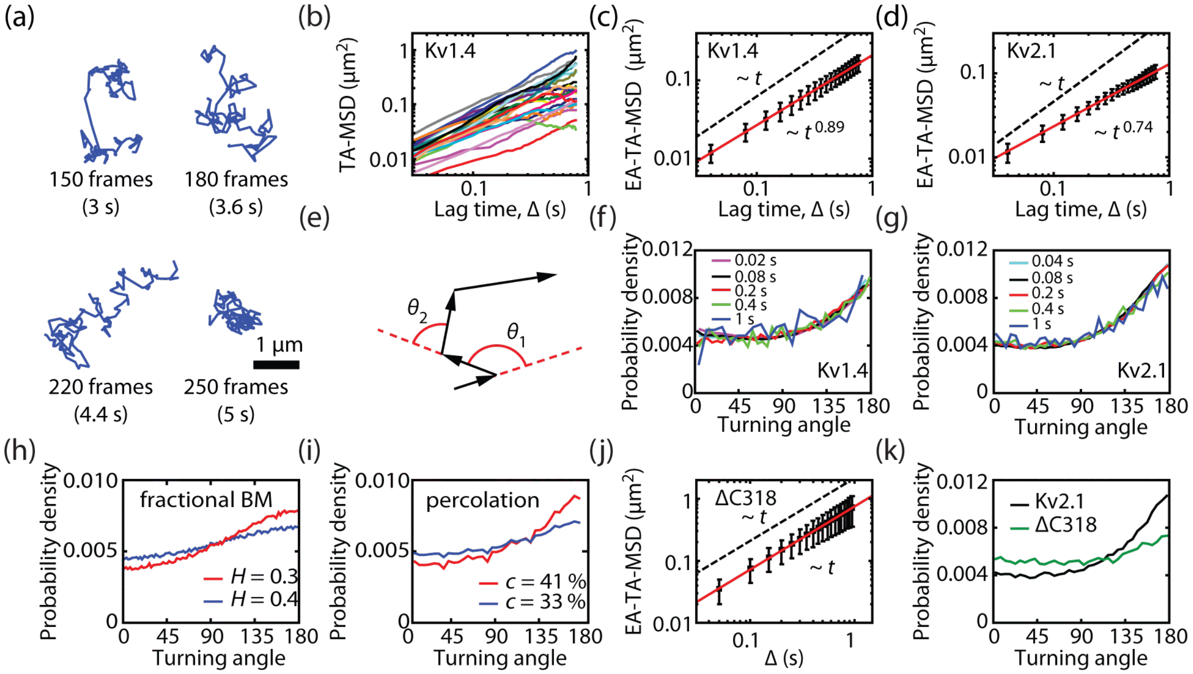

Figure 4.1. Voltage-gated potassium channels Kv2.1 and Kv1.4 undergo subdiffusion in the plasma membrane. (a) Four Kv1.4 representative trajectories obtained by single-particle tracking. (b) Time averaged MSD as a function of lag time Δ for 20 individual Kv1.4 trajectories. (c) Ensemble average time averaged MSD averaged over 1,312 Kv1.4 trajectories ($n = 10$ cells). (d) EATAMSD averaged over 6,385 Kv2.1 trajectories ($n = 14$ cells). The dashed lines in b and c are visual guides for linear behavior (free diffusion), i.e., $\left\langle\overline{\delta^2(\Delta)}\right\rangle \sim \Delta$. Error bars show standard deviation. (e) Sketch illustrating the construction of turning angles from a particle trajectory. (f)-(g) Turning angle distributions for Kv1.4 (10 cells, 1,312 trajectories) and Kv2.1 (14 cells, 6,385 trajectories). Turning angle distributions are constructed for lag times between 20 ms and 1 s. (h) Turning angle distributions for fractional Brownian motion simulations with Hurst exponents 0.3 and 0.4. (i) Turning angle distribution for simulations of obstructed diffusion with obstacle concentrations 33% and 41%. (j) MSD averaged over 3,114 ΔC318 trajectories ($n = 5$ cells). The dashed lines is visual guides for linear behavior (free diffusion). Error bars show standard deviation. (k) Turning angle distributions for Kv2.1 and ΔC318 (5 cells, 3,114 trajectories) measured with lag time of 200 ms.

where T is the total experimental time, $\mathbf{r}$ the particle position, and Δ the lag time, i.e., the time difference over which the MSD is computed. When a particle displays Brownian diffusion, the MSD is linear in lag time, i.e., $\overline{\delta^2(\Delta)} \sim \Delta$. In contrast, anomalous diffusion is characterized by a different MSD scaling, namely MSD $\sim \Delta^{\alpha}$, where α is the anomalous exponent. Anomalous diffusion is classified as subdiffusion when $0 < \alpha < 1$ and superdiffusion when $\alpha > 1$. Figure 4.1(b) shows the MSD of 20 individual trajectories. The MSDs of Kv1.4 as well as Kv2.1 channels show subdiffusive behavior, albeit with large apparent fluctuations. Figures 4.1(c) and 4.1(d) show the MSDs averaged over 1,312 Kv1.4 ($n = 10$ cells) and 6,385 Kv2.1 ($n = 14$ cells) trajectories, respectively, $\left\langle \overline{\delta^2(\Delta)} \right\rangle$. Throughout the manuscript we employ overlines to denote time averages and brackets to denote ensemble averages. The anomalous exponent α of Kv1.4 was found to be 0.89 and that of Kv2.1 was 0.74, indicating subdiffusion in both cases.

Several distinct mathematical models lead to subdiffusion [98, 99, 100]. Among the most well-accepted types of subdiffusion in biological systems, we encounter (i) obstructed diffusion, (ii) fractional Brownian motion (fBM), and (iii) continuous time random walks (CTRW). Both fBM [110, 111] and obstructed diffusion [112, 113, 114] are models for subdiffusive random walks with anticorrelated increments that have been extensively used in live cells. fBM describes the motion in a viscoelastic fluid [115, 116], which can be caused by macromolecular crowding [117, 118]. fBM is a generalization of Brownian motion that incorporates correlations with power-law memory. It is characterized by a Hurst exponent H that translates into an anomalous exponent $\alpha = 2H$. Obstructed diffusion describes the motion of a particle hindered by immobile (or slowly moving) obstacles, e.g., percolation. As the concentration of immobile obstacles increases, the availability of space decreases. Near a critical concentration known as percolation threshold, the obstacles form a fractal with dead ends in all length scales. In particular, the reduction of the available space results in anomalous diffusion with a recurrent exploration pattern. A CTRW is a generalization of a random walk where a particle waits for a random time between steps [119]. When the waiting times are asymptotically distributed according to a power law such that the mean waiting time diverges, the CTRW is subdiffusive. These three models describe very distinct physical underlying mechanisms but they can yield similar sublinear MSD scaling, particularly in obstructed diffusion and fBM models. Thus the MSD analysis is insufficient to elucidate the type of random walk.

Different tests beyond the MSD have been employed to distinguish among types of subdiffusive random walks, including p-variations [120], first passage probability distribution [121], mean maximal excursion [122], Gaussianity [123], and fractal dimensions [124]. Here we employ the distribution of directional changes, i.e., the turning angles, a tool that probes correlations in the particle displacements and has been shown to contain information on the complexity of a random walk [88]. Figure 4.1(e) illustrates the construction of turning angles from a particle trajectory. In simple Brownian motion, the turning angles are uniformly distributed. Contrastingly, when the steps are correlated the distribution of turning angles is not uniform [88]. Figures 4.1(f) and 4.1(g) show the distribution of turning angles of Kv1.4 and Kv2.1 for different lag times (1,312 Kv1.4 tracks, 10 cells and 6,385 Kv2.1 tracks, 14 cells). Both distributions peak at $\theta = 180^\circ$ indicating the particles are more likely to turn back than to move forward. In other words, Kv channels have a preference to go in the direction from where they came rather than to persist moving in the same direction. This property is a fingerprint of subdiffusive random walks with anticorrelated increments. Besides the shape of the distribution, the dependence on lag time bears valuable information. Strikingly, we observe that the distribution is independent of lag time, i.e., we measure the same distribution of directional changes whether the lag time is 20 ms or 1 s.

We examined numerical simulations of fBM and obstructed diffusion and found that they have distinctive fingerprints in their distribution of directional changes. Figure 4.1(h) shows the distribution of directional changes for subdiffusive fBM simulations with Hurst exponents $H = 0.3$ and 0.4. Even though the distributions peak at 180°, the probability density function is clearly different from the experimental data [Figs. 4.1(f) and 4.1(g)]. In Kv measurements, the turning angle distributions increase sharply as θ approaches 180° and most of the deviations from a uniform distribution are above 90°. However, fBM gives rise to a gradual increase that takes place mainly in the range $45° < \theta < 135°$. Further, the turning angles of fBM reach a plateau, in contrast to our measurements. Conversely, obstructed diffusion, strongly resembles our experimental results. Figure 4.1(i) shows the turning angle distribution for obstructed diffusion simulations in a square lattice with obstacle concentrations 33% and 41% [114]. Note that 41% is slightly above the percolation threshold. These results show that the motion of Kv channels in the plasma membrane is better modeled by percolation, i.e., obstructed diffusion, rather than motion in a viscoelastic medium, i.e., fBM.

Potential obstacle candidates for obstructed diffusion in the plasma membrane are the cortical cytoskeleton, lipid rafts, and extracellular glycans. By evaluating the MSD and turning angle distribution of ΔC318, a mutant in which the last 318 amino acids of the C-terminus of Kv2.1 channel had been deleted [125], we found that the anticorrelated diffusion originates from interactions with intracellular structures. We observed that ΔC318 channels diffuse freely in the plasma membrane, $\alpha = 1$ with a diffusion coefficient $D = 0.19\ \mu\text{m}^2/\text{s}$ [Fig. 4.1(j), n=3114 tracks, 5 cells]. Further, the distribution of turning angles of ΔC318 was flattened, as expected for Brownian diffusion [Fig. 4.1(k)], indicating the intracellular

C terminal domain of Kv2.1 plays a key role in the anticorrelations within the particle trajectory. Even though the distribution of turning angles in the ΔC318 mutant is close to that in Brownian motion, a small peak is still noticeable at 180° suggesting additional complexities in the plasma membrane.

In contrast to Kv1.4, which is homogeneously distributed on the cell membrane, a subpopulation of Kv2.1 channels forms micron-sized clusters that localize to endoplasmic reticulum (ER)-plasma membrane junctions [36, 37]. Thus, we expect both the ER and the cortical cytoskeleton introduce intracellular interactions with Kv2.1 channels. To identify the origin of the observed anticorrelated diffusion, we analyzed the motion of non-clustered Kv2.1 channels, i.e., the channels that reside outside ER-plasma membrane junctions. We labeled Kv2.1 channels both with green fluorescent protein (GFP) and QDs [37]. While all the channels were labeled with GFP, only a small fraction included QDs in order to enable both single-particle tracking and cluster identification [fig. 4.2]. We observed that the distribution of directional changes of non-clustered channels is indistinguishable from that of the overall population [fig. 4.3]. Thus, we can exclude interactions with the ER as the cause for anticorrelated subdiffusion. These observations suggest that diffusion is hindered by intracellular components, possibly the cortical cytoskeleton, in agreement with a membrane-skeleton fence model [30].

We observed that the distribution of turning angles were independent of lag times [Figs. 4.1(f) and 4.1(g)] within the probed spatial and temporal scales. These observations indicated the anticorrelated subdiffusion of Kv channels did not have an evident characteristic time scale. This type of random walk is consistent with diffusion on a self-similar structure, i.e., a fractal subspace. In order to visualize the difference between diffusion on

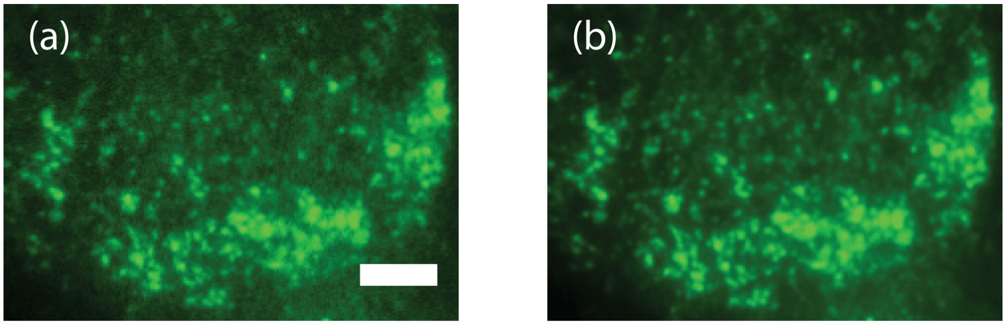

Original

Framed averaged

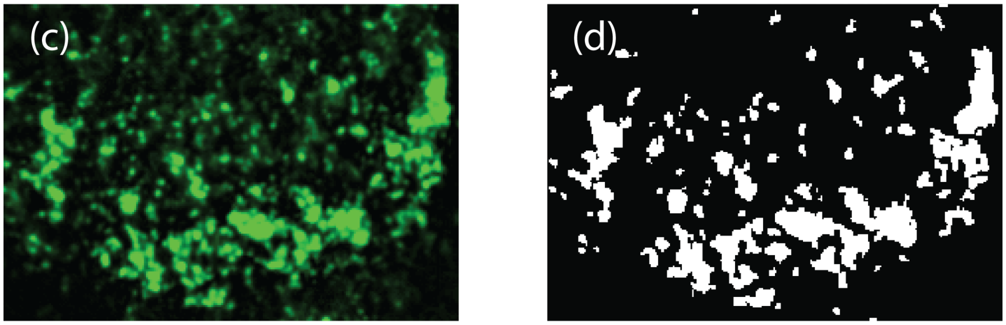

Top-hat filtered

Thresholded

FIGURE 4.2. Detection of Kv2.1 clusters. (a) TIRF image of GFP-Kv2.1. Bright spots show Kv2.1 clusters, which colocalize to endoplasmic reticulum-plasma membrane junctions [36, 37]. (b) The images are framed-averaged over 50 frames in order to increase signal-to-noise ratio. (c) Background noise is reduced using a top-hat filter. (d) Kv2.1 clusters are detected by thresholding the filtered image. Scale bar is 5 μm.

a fractal structure, and diffusion on a meshwork with a characteristic length scale, we performed simulations of motion of a particle in the presence of permeable fences that introduce compartments with a well-defined length scale [Fig. 4.4]. In these simulations, we observed that the distribution of turning angles is not time invariant; the peak at 180° grows as we increase the lag-time up to a characteristic time, and then it decays when the lag-time increases further [Figs. Fig. 4.4(b) and Fig. 4.4(c)]. Thus, hop-diffusion with a narrow distribution of confinement sizes exhibits a time-dependent turning angle distribution (with a well-defined characteristic time scale), in contrast to our experimental results where the turning angle distribution is time-invariant.

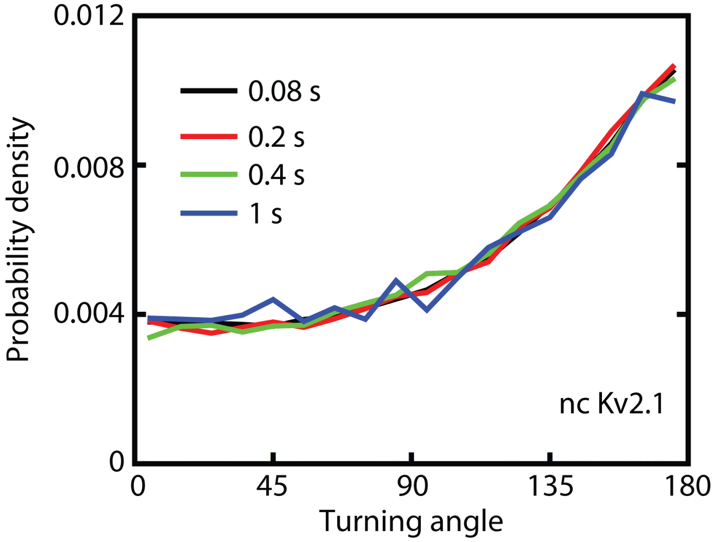

FIGURE 4.3. Turning angle distributions for non-clustered Kv2.1 channels.Turning angle distributions for non-clustered Kv2.1 channels, i.e., channels that lie outside of endoplasmic reticulum-plasma membrane junctions (5 cells, 2,851 trajectories).

4.2.2. Cortical actin transiently confines Kv1.4 and Kv2.1 channels. We observed that Kv channels undergo obstructed diffusion as shown in Fig. 4.1. The ΔC318 mutant data indicated that hindering of the particle motion originated within cytoplasmic structures in close proximity to the plasma membrane, in agreement with previous experimental evidence of transient confinement by the actin-based cytoskeleton [107, 126, 127, 29, 128, 108]. Thus we examined the cortical actin as a candidate for the observed obstructed diffusion in the plasma membrane.

We imaged the cortical actin in live HEK cells using the photoactivatable probe tdEosFP [129] via an actin binding peptide (ABP) that reversibly binds to F-actin [130]. Previous studies showed that expression of ABP-tdEosFP does not affect the organization of the cytoskeleton [130, 131]. By activating a sparse subset of ABPs and individually localizing their center with high precision, we generated photoactivated localization microscopy (PALM) reconstructed images using localizations from 100 frames (2 s), yielding a smooth video of the

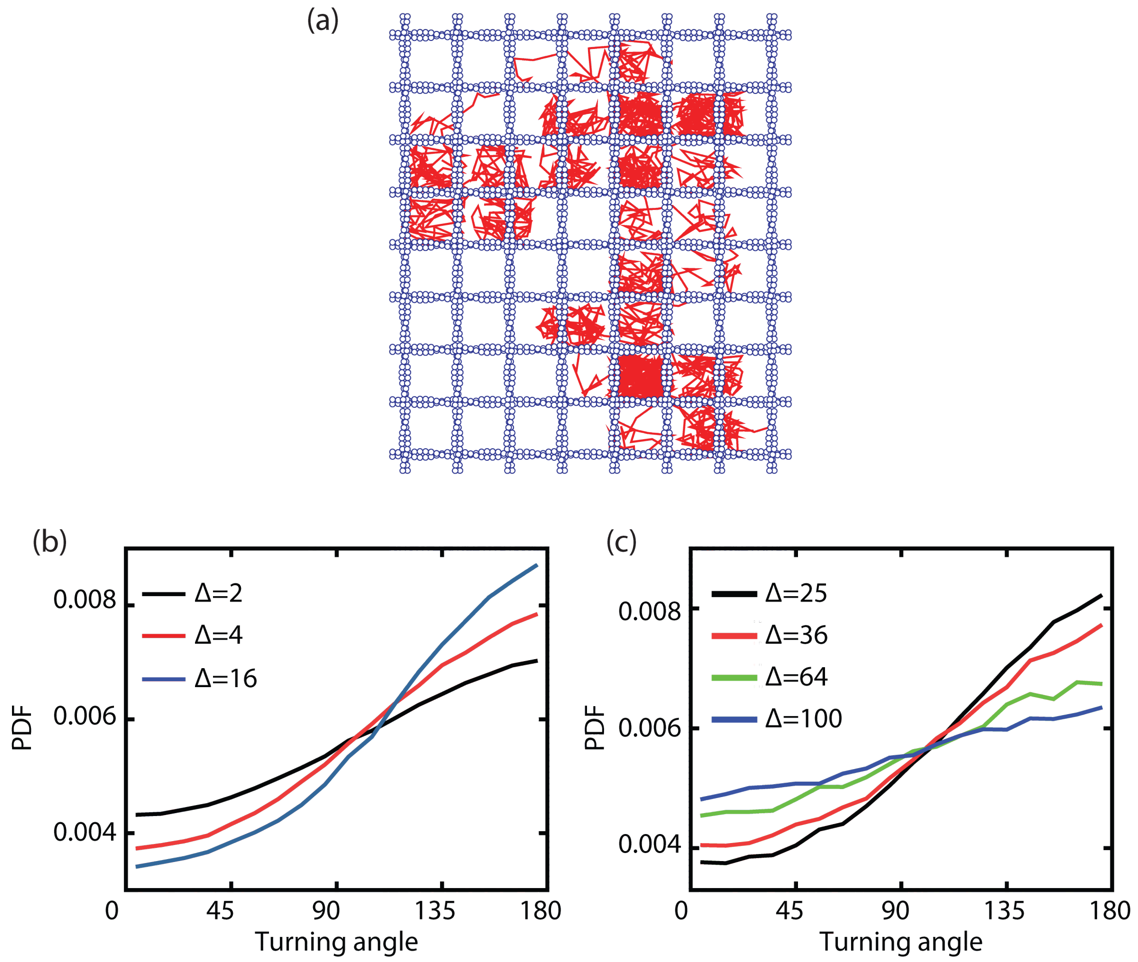

FIGURE 4.4. Simulations in a permeable fence model. (a) An example of a numerical simulation for random walks in the presence of permeable fences. The fences are sketched as actin filaments. The random walk simulation is performed off-lattice with step sizes drawn from a normal distribution with standard deviation $\sigma = 5$ in both x and y directions. the fences are placed a distance of 20 units from each other. All trajectories are 10,000 steps. The fences are permeable with 5% probability of permeation. Turning angle distributions are calculated for 1,000 trajectories for lag times (b) $\Delta = 2, 4, 16$, and (c) $\Delta = 25, 36, 64, 100$.

dynamic actin meshwork. The dissociation of ABP-tdEosFP occurs with a time constant on the order of 40 s [130], thus the exchange within 2-s imaging is negligible.

Figure 4.5(a) shows a representative PALM reconstruction of actin. Although the number of localizations in 100 frames is not adequate to fully resolve the cortical actin and some faint fluorescent single-filament structures might be missed in the images, we could use the

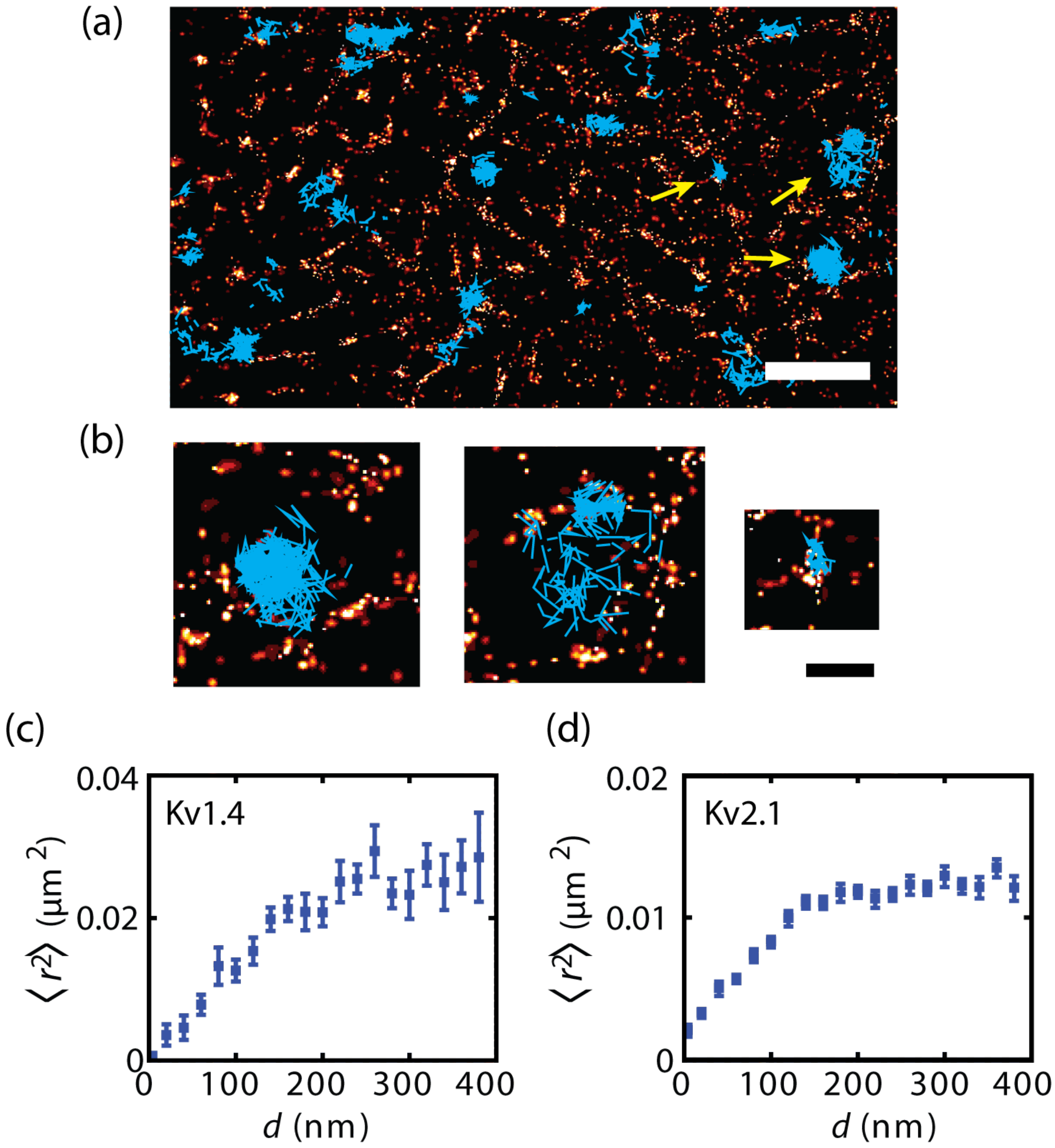

FIGURE 4.5. Cortical actin transiently confines Kv channels. (a) Trajectories of individual Kv2.1 channels (shown in cyan) overlaid on actin PALM image (shown in red). Scale bar 2 μm. (b) Enlargements of the areas indicated with yellow arrows in a. Scale bar is 500 nm. The left trajectory shows confinement in a large compartment, the middle one shows hoping between two compartments and the right one shows confinement in a nanoscale domain. (c)-(e) Mean square displacements $\langle r^2 \rangle$ covered by Kv1.4 and Kv2.1 and ΔC318 channels in 200 ms as a function of their maximum distance from nearest actin feature. Error bars indicate standard errors.

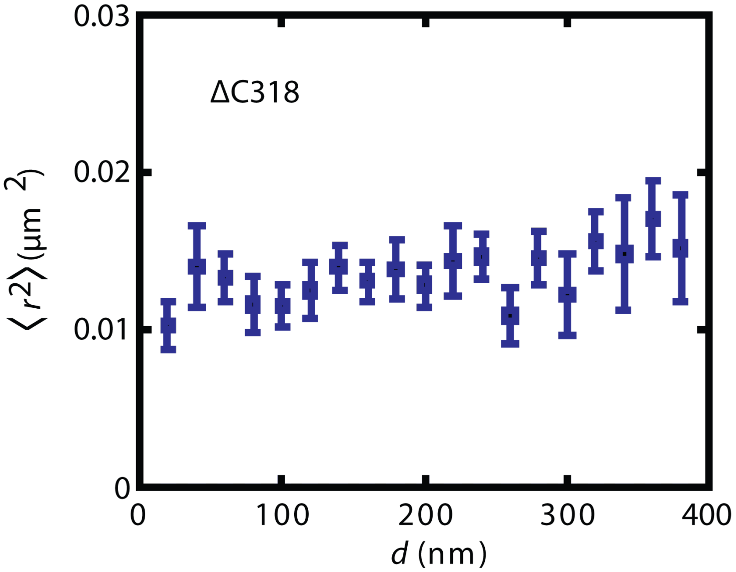

FIGURE 4.6. Cortical actin does not confines ΔC318 channels. Mean square displacements $\langle r^2 \rangle$ covered by ΔC318 channels in 200 ms as a function of their maximum distance from nearest actin feature. Error bars indicate standard errors.

reconstructed PALM image to study the interactions of the potassium channels with the actin cortex in live cells. Previous breakthrough experiments have reported simultaneous imaging of cortical actin cytoskeleton and single-particle tracking [128, 132, 133]. Here, to the best of our knowledge, we perform for the first time simultaneous single-particle tracking measurements and imaging cortical actin with superresolution.

In order to find out whether actin-delimited domains as identified by PALM hinder the diffusion and compartmentalize the cell surface, we imaged and tracked Kv1.4, Kv2.1 channels on the cell surface while simultaneously imaging the cortical actin. Channels often remained confined within the areas enclosed by actin indicating actin acted as a barrier to channel diffusion. To visualize the confined diffusion of the channels, we show Kv2.1 channel full tracks for one movie (2000 frames) on the last reconstructed image of the cortical actin in Figs. 4.5(a) and 4.5(b). However, this visualization method suffers from overlaying long trajectories on a single reconstruction image of the actin meshwork.

In addition to being constrained by actin structures, some trajectories exhibit confinement within small nanoscale domains that do not appear to be enclosed by actin. We have previously shown that Kv channels exhibit frequent immobilizations when the channels are captured within clathrin-coated pits [106]. Thus, the cortical actin cytoskeleton is evidently not the sole mechanism by which the mobility of Kv channels is hindered. In order to deal with these complexities, we evaluated the MSDs as a function of actin proximity.

Given that actin hinders channel motility, we expect the particles to explore smaller areas when they are confined within smaller compartments. To test the actin fence hypothesis, we overlaid channel trajectories on the corresponding PALM image of actin obtained in 2 s, a time scale in which the actin structure is fairly persistent [supplementary video 1], with a sliding time window 0.2 s. For example, trajectories of the channels from 0 to 2 s were overlaid on the first reconstructed actin frame and the trajectories in the interval 200 ms to 2.2 s were overlaid on the second actin PALM frame. Then we partitioned the trajectories into 200-ms intervals and classified each segment according to the maximum distance d of the particle to the nearest actin feature, calculated using an Euclidean distance map algorithm. We evaluated the ensemble-averaged MSD $\langle r^2 \rangle$ of all the segments located at a specific distance away from actin, i.e., we averaged the squared displacements in 200 ms of the particles transiently located a given distance from actin. Figures 4.5(c) and 4.5(d) show the MSD as a function of distance-to-actin for Kv1.4 and Kv2.1. For both channels we observed that as molecules dwell closer to actin their MSD decreases.

As a control of our method, we performed the same experiment and analysis for ΔC318 channels. Because of lack of intracellular domain, these channels should not have any interaction with the cortical cytoskeleton. We observed that the MSD of ΔC318 channels is independent of distance from actin [Fig. 4.6], which proves the effect of intracellular structure in the transient confinement of Kv channels.

4.2.3. Visualization and characterization of Fractal structure of actin in fixed cells. When imaging live cells with PALM, the number of frames used in the reconstruction is restricted by the cell dynamic nature. A low number of frames results in insufficient detected particles to accurately determine the structure, also having a deleterious effect on resolution. In contrast, very high spatial resolution can be obtained in fixed cells by collecting data over long times [134, 135, 136]. Therefore, we used TIRF-STORM to visualize the compartments formed by cortical actin in fixed cells. Actin was labeled with phalloidin conjugated to Alexa Fluor 647, which binds actin filaments with high specificity without significantly enlarging them [136]. A total of 50,000 frames where used in the reconstruction. In our STORM reconstructions we observed both thick and thin actin structures, Fig 4.7(a). The finest structures that we observed had a cross section standard deviation of 20 nm (FWHM=48 nm). Figure 4.7(d) shows the average cross section profile of 20 lines aligned by the center of each line. The thickness of these lines in the reconstruction is governed by the localization accuracy, 20 ± 8 nm (mean ± SD, Fig. 4.8), which sets a lower bound on STORM resolution. Thus we are unable to determine whether these structures are individual filaments (10 nm in diameter) or actin bundles.

We employed a watershed segmentation algorithm [137] to identify actin-delimited compartments in the STORM reconstructions [Figs. 4.7(b) and 4.7(c)] across the whole cell. The average percentage of the watershed meshwork covered by actin was $84 \pm 4\%$ (mean ± SD, n=9 cells). Figure 4.7(e) shows the distribution of compartment areas ($n = 2,500$ compartments). The areas of the compartments are fitted well by a log-normal distribution,

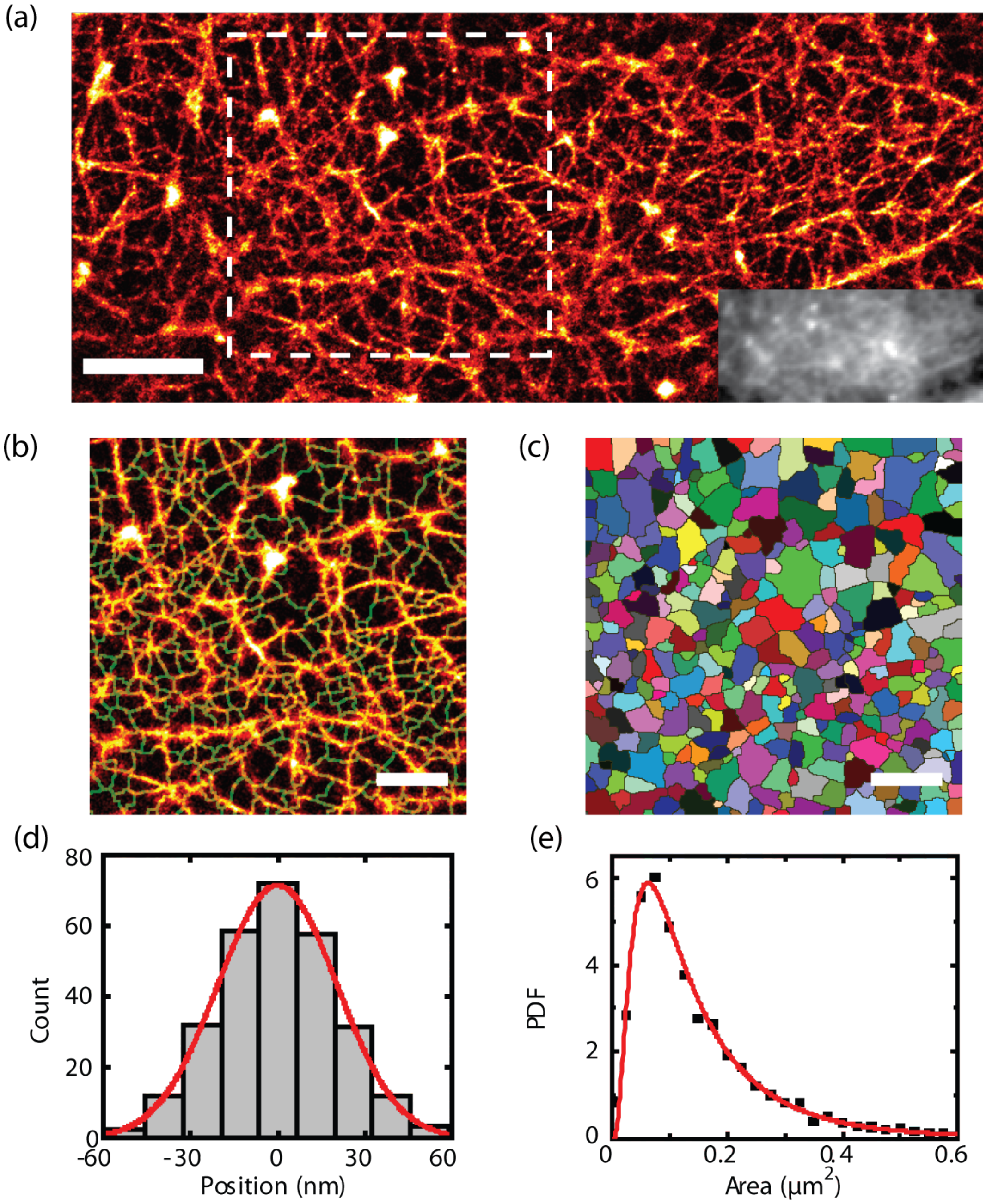

Figure 4.7. Characterizations of actin compartments. (a) Superresolution STORM image of the cortical actin in a HEK cell represented in false colors. The inset shows the TIRF image of the same field of view. Scale bar is 2 μm. (c) Average cross-sectional profile of 20 filaments aligned by the center of each line. Red line, Gaussian fit with FWHM of 48 nm. (d) Watershed segmentation (shown in green) of the boxed area in a overlaid on the STORM image. (e) Compartments determined by watershed are designated with different colors. Scale bars in c and d are 1 μm. (e) Distribution of compartment areas for fixed cells (9 cells, n=2,500 compartments). Red line is a log-normal distribution with the shape parameter $\sigma = 0.8$ μm.

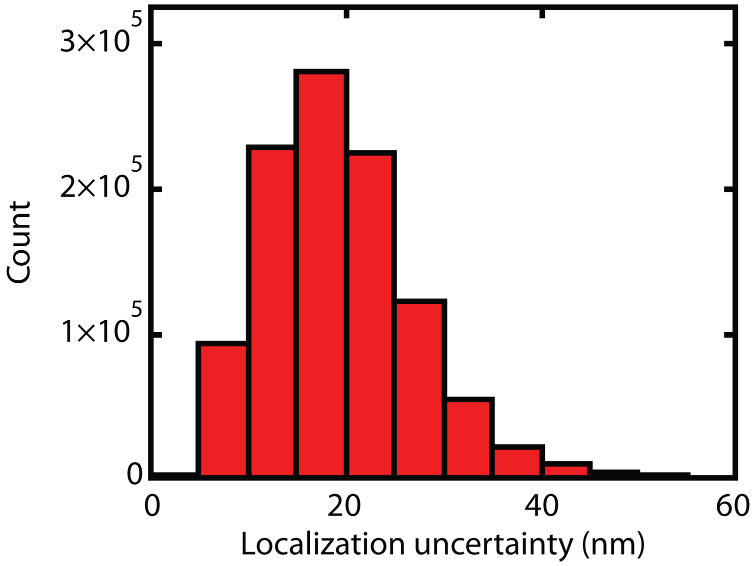

FIGURE 4.8. Localization uncertainty. Histogram of the localization uncertainties for one actin STORM reconstruction using Alexa Fluor 647-phalloidin.

which is a subexponential heavy-tailed distribution in the sense that it decays more slowly than any exponential tail [138]. The log-normal distribution is in good agreement with Kolmogorov's model for the distribution of particle sizes after repeated breakage [139, 140]. When a particle is divided into fragments in such a way that the fragment proportions are independent of the original particle size, a log-normal distribution emerges in the particle sizes after random repeated fragmentation. Analogously, actin-delimited compartments are split into smaller compartments by growing actin filaments and thus their distribution is predicted to be log-normal.

In addition to the compartment area distribution, the relation between perimeter and area contains valuable information. Perimeter-area relations have been extensively used to investigate the properties of complex planar shapes [141, 142]. As expected, we observe that areas and perimeters of the different compartments are highly correlated [Fig.4.9(a)]. This correlation indicates shape homogeneity among different compartments [143]. Furthermore, the area exhibits the same scaling over the whole observed range, $A \sim L^{1.8}$, where A and L

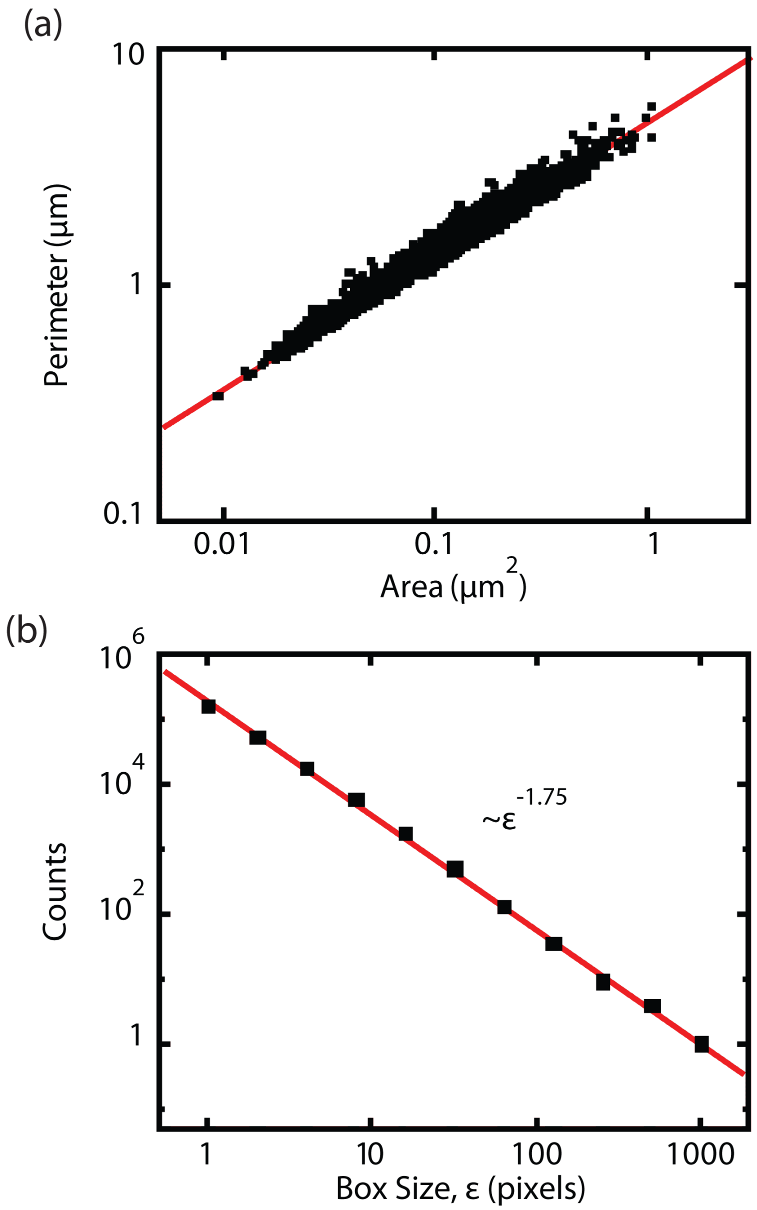

FIGURE 4.9. Probing fractality of the cortical actin meshwork. (a) Double logarithmic scatter plot of compartment perimeter vs compartment area. The fitted curve corresponds to the equation $= 0.55x + 0.68$ (Pearson correlation coefficient= 0.98). (b) Representative example of box counting algorithm in one cell where the exponent yields $d_f = 1.75$.

are compartment area and perimeter, indicating the same statistical character at different scales, and suggesting that compartments formed by cortical actin are scale-invariant in the observed range. Such scale invariance is a hallmark of a self-similar fractal structures.

Fractals are characterized by scaling properties governed by a non-integer dimension d_f, i.e., an anomalous dependence of the "mass" on the linear size of the system with $M \sim l^{d_f}$. In a regular object such as a line, square, or cube, we would refer to its mass M as the length, area or volume, respectively. In these regular cases the mass scales as $M \sim l^d$, where the l is the linear size and $d = 1, 2, 3$ is the spatial dimension. On the other hand, fractals such as a Sierpinsky gasket or a percolation cluster differ from Euclidean spaces and display a fractional dimension [141, 144]. Usually the capacity dimension is obtained using a box-counting algorithm that quantifies the mass scaling. In brief, the structure is placed on a grid, the number of occupied "boxes" are counted, and the process is iterated for finer grids. The number of occupied boxes scales as $N \sim \epsilon^{-d_f}$, where ϵ is the box length. Figure 4.9(b) shows the computation of the fractal dimension of the cortical actin meshwork from the STORM image in a representative cell. The box counting analysis shows the actin structure exhibits statistical self-similarity over more than three decades. Our data indicate the fractal dimension of the meshwork is $d_f = 1.75 \pm 0.02$ ($n = 9$ cells).

4.3. Discussion

Our current understanding of the plasma membrane is that of a complex partitioned fluid where molecules often undergo anomalous diffusion and can be segregated according to their function. We observe that K^+ channels perform a random walk with antipersistent nature, i.e., a random walk with an increased probability of returning to the site it just left. However elucidating the mechanisms that cause anomalous diffusion is not trivial because several different subdiffusion models lead to similar MSD scaling. The analysis of K^+ channel motion is further complicated by the occurrence of immobilizations with power law sojourn times, which introduce deviations from Gaussian functions in the distribution of displacements

[86, 106]. Thus, we cannot employ Gaussianity-based tests to distinguish among complex antipersistent random walks. We find that the distribution of directional changes provides a robust test for the type of random walk. The measured channel trajectories are shown to be well described by obstructed diffusion but not by fBM.

We observed that the Kv2.1 intracellular domain played a key role in the anomalous diffusion, in agreement with previous observations showing that the depth at which a membrane protein extends into the cytoplasm determined how frequently it encountered mechanical barriers [127]. The obvious candidate to obstruct the motion of proteins with large intracellular domains is the actin cytoskeleton. Thus, we visualized the cortical actin with high temporal and spatial resolution and evaluated its effect on membrane protein dynamics. Considering that some faint single-filament actin structures might not be accurately detected by PALM imaging, we can miss some interactions between actin and membrane proteins. Notwithstanding, we found that Kv channels are transiently confined by permeable actin fences, confirming existing models for membrane compartmentalization as an organizing principle of the actin cytoskeleton [30]. By studying the diffusion of Kv2.1 channels outside ER-plasma membrane junctions, we verified that the observed subdiffusion is not due to interactions with ER. Other intracellular components such as intermediate filaments could also hinder protein diffusion and further compartmentalize the cell membrane, but these cytoskeletal filaments were not studied in the present work. Previous single-particle tracking works using lipids labeled with 40-nm gold nanoparticles have observed the compartmentalization of the plasma membrane of HEK293 cells, with 70-nm mean compartment size [91]. However, this compartmentalization occurs with molecules having virtually no cytoplasmic domains and with a residence time close to 3 ms. At time scales above 50 ms, gold-labeled lipids were found to exhibit Brownian diffusion with an effective diffusion coefficient $D = 0.41\ \mu\text{m}^2/\text{s}$ [91], similar to our observations for ΔC318 Kv2.1 mutant.

Ion channels are observed to undergo anticorrelated anomalous diffusion over at least two orders of magnitude in time. In terms of percolation theory, this hints the cell surface is maintained close to criticality, i.e., near the percolation threshold. However, this hypothesis seems highly unlikely. A more feasible explanation stems from the emergence of a scale-invariant structure under the plasma membrane. We directly observed that, within the probed spatial scale, the actin cortex has in fact a self-similar nature. It is possible to speculate that actin fractality develops from its branching structure. Hierarchically branched structures have a fractal dimension d_f such that $R_b = R_r^{d_f}$, where R_b is the bifurcation ratio and R_r is the length-order ratio [145]. The bifurcation ratio can be interpreted as the average number of branches that emerge after a bifurcation and the length-order ratio is defined as the ratio between incoming branch length and the length of the emerging branches until the next bifurcation [146]. Actin branching is driven by the Arp2/3 complex [147] with a bifurcation ratio $R_b = 2$. Here we measure a meshwork fractal dimension $d_f = 1.75$, which can arise from a branching pattern with $R_r = 1.5$ or, in other words, the daughter branch being on average 1/3 shorter than the mother branch. The fractal dimension of the cytoskeleton is in line with a broad range of fractal geometries found in biology ranging from the lung alveoli to subcellular structures such as mitochondrial membranes and the endoplasmic reticulum [141].

We propose that the fractal nature of the actin cortex is employed by the cell to organize the plasma membrane. The complexity of this structure leads to a hierarchical organization with domains in multiple length scales and the development of nested compartments. Such a dynamic hierarchical organization facilitates the active segregation of domains with different functions and the maintenance of reactants near reaction centers. Furthermore, the fractal nature of the cortical actin has broad implications for anomalous diffusion, for instance it could bridge the gap between the plasma membrane hop diffusion models and diffusion in a fractal that leads to anomalous dynamics over broad time scales. We foresee that a self-similar cytoskeleton structure also influences active actomyosin-mediated organization of the plasma membrane [148] in such a way that these processes can take place over multiple length scales.

In conclusion, our findings show that the plasma membrane is compartmentalized in a hierarchical fashion by a dynamic cortical actin fractal. We find that the anomalous diffusion of potassium channels is best modeled by obstructed diffusion or diffusion in a fractal. By combining PALM imaging with single-particle tracking we were able to directly visualize the hindering effect of cortical actin on the diffusion of the membrane proteins. We characterized the compartments formed by cortical actin using superresolution imaging in fixed cells and found evidence for the self-similar topology of this structure.

4.4. Materials and methods

4.4.1. Cell transfection and labeling. HEK 293 cells (passage 42-49; American Type Culture Collection) were cultured in phenol red Dulbeccos Modified Eagles Medium (DMEM), supplemented with 10% fetal bovine serum (FBS; Gibco) at 37 °C. Transfection was performed in a 0.2-cm gap cuvette via electroporation using a 110 V, 25 ms pulse (Genepulser Xcell; BioRad Laboratories) with: 3 μg of BirA and either 3 μg of Kv2.1-loopBAD, Kv1.4-loopBAD or Kv2.1-ΔC318-loopBAD as previously described [149]. Cells were transfected to express a Kv2.1 or Kv1.4 construct with an extracellular biotin acceptor domain that, when coexpressed with a bacterial biotin ligase, results in biotinylated Kv channels on the cell surface [149]. For live-cell actin imaging cells were transfected with 3 μg of ABP-tdEos. ABP is the actin-binding sequence of ABP140 from *S. cerevisiae* consisting of 17 amino acids [130, 131]. Kv2.1-loopBAD-GFP (3 μg) was employed to identify Kv2.1 clusters on the cell surface. Cells were incubated overnight in phenol red free DMEM with 10% FBS at 37 °C and imaged 12-24 hours after transfection. Transfected cells were cultured and imaged on round, glass-bottom dishes coated with Matrigel (BD Biosciences). Prior to imaging, the medium was replaced with HEK imaging saline (146 mM NaCl, 4.7 mM KCl, 2.5 mM $CaCl_2$, 0.6 mM $MgSO_4$, 1.6 mM $NaHCO_3$, 0.15 mM NaH_2PO_4, 0.1 mM ascorbic acid, 8 mM glucose, and 20 mM HEPES, pH 7.4).

For single-particle tracking, biotinylated channels were labeled with QDs. Cells were incubated for 10 minutes in HEK imaging saline with 1 nM streptavidin-conjugated QD705 or QD655 (Invitrogen) and 10 mg/mL bovine serum albumin (BSA) [86] at 37 °C. Following incubation the cells were rinsed again six times with HEK imaging saline to ensure the removal of any unbound QDs. The diameter of the QDs is in the range 10-15 nm, thus given that Kv channels are similar in size to the QDs, it is highly unlikely that the Kv:QD stoichiometry is higher than 1:1. We have previously shown that QD conjugation does not alter Kv diffusion [86, 106].

4.4.2. Live cell imaging. Imaging was performed in an objective-based TIRF microscope built around an IX71 Olympus body. An antireflection-coated achromatic 400-mm lens focused the beams on the back aperture of the objective (100x PlanApo N.A. 1.45; Olympus). The position of this focusing lens was manually adjusted so that TIRF was achieved. The laser power before the objective was 20 mW for the blue laser, and 80 mW for the yellow laser.

To maintain an appropriate density of activated molecules, the intensity of the activation laser was adjusted between 0.01 and 0.1 mW using neutral density (ND) filters. Typically, the laser power was increased as the density of photoactivatable fluorophores decreased during imaging. Fluorescence emission was captured in an electron multiplying charged-coupled device (EMCCD, iXon DU-888, Andor). Images were acquired using IQ2.3 software (Andor) at 50 frames per second. The emissions of the ABP-tdEos (or GFP) and the QDs were separated with a Cairn Optosplit II (Cairn Research) using a dichroic beam splitter (Semrock). Sample temperature was kept at 37 °C using objective and stage heater (Bioptechs). A 405 nm laser was used to activate the photoswitchable tdEos fluorophore, while 473 nm and 561 nm lasers were used to excite it in its inactive and active states, respectively. Setup detail in supplementary information.

4.4.3. Single-particle tracking. QD labeling was controlled so that QDs remained at low density to allow for single-particle tracking [86]. Particle detection and tracking were performed in MATLAB using u-track [150].

4.4.4. Distribution of turning angles. We define the turning angle $\theta_t(\Delta)$ at time t and lag time Δ, from successive displacements $\boldsymbol{\delta}(t,\Delta) = \boldsymbol{r}(t+\Delta) - \boldsymbol{r}(t)$

$$\theta_t(\Delta) = \arccos\left(\frac{\boldsymbol{\delta}(t,\Delta)\cdot\boldsymbol{\delta}(t+\Delta,\Delta)}{|\boldsymbol{\delta}(t,\Delta)|\,|\boldsymbol{\delta}(t+\Delta,\Delta)|}\right), \tag{14}$$

where the angles are defined between 0° and 180°.

4.4.5. PALM reconstruction. Post-imaging processing was implemented in MATLAB using a script provided by Keith Lidke [151]. A sliding time window of 2 s was used in the

PALM reconstruction so that the image is refreshed at every frame yielding a smooth video (supplementary Video S1).

4.4.6. Euclidean distance maps. Euclidean distance maps (EDMs) were employed to calculate the distance from a Kv channels to actin at any given time. EDMs were generated from a binary image, where the features of interest were set to 1 and the background pixels were set to 0. The algorithm created a new image where each pixel had a pixel value that corresponded to the Euclidean distance of that pixel from the nearest feature. Thus, pixels that neighbored actin structure were assigned a pixel value of 1, pixels that neighbored pixels with value 1 were assigned a value of 2, etc. [152].

4.4.7. Analysis of ion channel displacement as a function of actin-based confinement. The distance of Kv channels from actin was calculated at each point of their trajectories using Euclidean distance mapping (EDM) [152]. Then the squared distance traveled by the channel in 200 ms was obtained. A 2D histogram of the channel displacement vs its maximum distance from actin during the same time was constructed, with bin size equal to 20 nm for EDM and 2000 nm^2 for the squared displacement. To investigate the correlation between mean square displacement and actin confinement, we averaged the square displacement for all the channels that were located within a given distance range from actin ($d \pm 10$ nm).

4.4.8. Kv2.1 cluster detection. GFP-Kv2.1 images were segmented in order to identify the areas covered by ER-plasma membrane junctions [37]. To increase signal to noise ratio, the videos were frame averaged so that one image is obtained every 50 frames (1 s). Visual inspection indicated Kv2.1 clusters did not change size or location over this time scale. Since background noise was not homogeneous across the cell, we applied a top-hat filter to reduce local variations in intensity. At last, the filtered image was thresholded to identify

Kv2.1 clusters. A representative image and the corresponding processing steps are shown in supplementary Fig. S2. Using the binary image of GFP-Kv2.1 clusters we split the trajectories of individual QD-Kv2.1 into regions inside or outside the clusters.

4.4.9. Numerical simulations. Obstructed diffusion was modeled by a Monte Carlo simulation in a square lattice. Obstacles were placed on the lattice at random sites drawn from a uniform distribution. The random walk was implemented in MATLAB using a "blind ant" algorithm [114]. A walker is placed in the center of the lattice and it is only allowed to move into non-blocked sites. If the chosen site (any of the four adjacent sites) is blocked, the walker remains at the original position and the clock ticks independent of whether the jump is successful. A lag time $\Delta = 500$ steps was employed to lessen the effect of the matrix geometry. When $\Delta = 1$ step, only four angles are possible. Even when $\Delta = 500$ steps, small artifacts can be seen around $0°, 45°, 90°, 135°$, and 180° due to the square symmetry.

For the fence models, random walk simulations were performed off-lattice with step sizes drawn from a normal distribution with standard deviation $\sigma = 5$ in both x and y directions. Fences were placed a distance of 20 units from each other as illustrated in supplementary Fig. S3. Each time a tracer attempted to cross a fence it remained in place with probability 95%, i.e., the permeability of the fences was set to 5%.

Fractional Brownian motion was generated in MATLAB using the function $wfbm$ in two independent dimensions.

4.4.10. Image registration. To determine the offset between the left (QD) and the right (tdEosFP) image channels, a white light image of immobilized 1-μm polystyrene beads (Polysciences, Warrington, PA) was obtained prior to imaging cells (supplementary Fig. S5a). Beads were localized in both channels with an accuracy of 8 nm through a cross-correlation algorithm implemented in LabView (National Instruments, Austin, TX). Since each bead appeared in both sides of the image, the offset was determined from the differences in their x and y locations. This process revealed astigmatism induced by the dichroic mirror used to split the imaging channels. In order to overlay the channels, a linear fit of the bead correction was employed to adjust the localization of the tdEosFP (supplementary Fig. S5b).

4.4.11. Cell fixation and labeling. Cells were plated on Matrigel coated 35 mm petri dishes. After 12 hours the cells were fixed and labeled according to established protocols known to preserve the actin cytoskeleton [153, 136]. Cells were first fixed for 12 min using a solution of 0.3% glutaraldehyde and 0.25% Triton X-100 in cytoskeleton buffer (CB, 10 mM MES, pH 6.1, 150 mM NaCl, 5 mM EGTA, 5 mM glucose and 5 mM $MgCl_2$), and then postfixed for 15 min in 2% glutaraldehyde in CB. The sample was treated with freshly prepared 0.1% $NaBH_4$ for 7 min to reduce background fluorescence. Actin filaments were labeled with Alexa Fluor 647-phalloidin (Invitrogen A22287) overnight at 4 °C. A concentration of 0.5 μM phalloidin in phosphate buffered saline (PBS, pH 7.4) was used. To minimize the dissociation of phalloidin from actin, the sample was briefly washed once with PBS and then immediately mounted for imaging. Imaging buffer was 50 mM Tris-HCl (pH 8.0), 10 mM NaCl, 10% glucose, 0.56 mg/ml glucose oxidase, 34 μg/ml catalase, 10% glucose, and 1% β-mercaptoethanol.

4.4.12. Fixed cell imaging. Image stacks were obtained using the same setup as live cell imaging. A continuous illumination of 638 nm laser was used to excite the Alexa Flour 647. The laser power before the objective was 30 mW. To maintain an appropriate density of activated molecules, 405 laser was used for some movies. Fifty thousand (50,000) frames were collected to generate a super-resolution image.

4.4.13. STORM reconstruction. Post-imaging processing, including drift correction using autocorrelation function, was performed with ThunderSTORM, an ImageJ plugin [154]. Each reconstruction was obtained using $50,000$ frames (imaged at 50 frames/s).

4.4.14. Characterization of compartments. We employed watershed segmentation [137] to identify and characterize compartments as seen by STORM. Once watershed images were generated, compartment areas were found using MATLAB function *regionprops*. The watershed principle can be understood by considering an image to be a topographic region of valleys and hills. First the region is flooded, filling the valleys and, as they overflow, the water follows a path along the nearest minima. Watersheds create lines that follow the path of the water. The results are effective at segmenting an image based on the intensity information. The watershed algorithm has been previously applied to fluorescence imaging, particularly in the segmentation of cell nuclei [155, 156]. We use watershed segmentation to outline actin-based compartments. Watersheds were generated from STORM images of the actin cytoskeleton. Images were segmented via thresholding and converted to binary images using ImageJ. Watersheds were then generated in MATLAB. This image processing yielded compartment outlines based on the available actin cytoskeleton information.

4.4.15. Fractal dimension. The fractal dimension of the actin cortex was computed using a box-counting algorithm. The thresholded binary actin image was placed on a grid of square boxes of size ϵ and the number of occupied boxes was counted. The process was repeated for grids of boxes with different sizes. The number of occupied boxes scales as

$$N \sim \epsilon^{-d_f}, \tag{15}$$

where d_f is the capacity dimension, or simply the fractal dimension.

4.4.16. Statistics. Results show mean and s.e.m. unless indicated otherwise. All experimental results were obtained from multiple different dishes and days. The number of distinct imaging regions, i.e., different cells is indicated in the text. P values were calculated using Origin software with two-tailed Students *t*-test and and results with P value ¡0.01 were considered as statistically significant.

CHAPTER 5

CONFINED LATERAL DIFFUSION: ROLE OF THE DISTRIBUTION OF CONFINEMENT SIZES

5.1. Introduction

In the previous chapter we showed that the cell plasma membrane is compartmentalized by the cortical actin skeleton. We observed that the size of the compartments formed by actin have a log-normal distribution [Fig. 4.7(e)]. Although this was the first direct observation of the compartmentalization of the plasma membrane in live cells, there are other excellent experimental characterization of the cell membrane compartments. Compartments were studied for various cell types by either segmenting trajectories obtained by single particle tracking (SPT) to different modes of motion [157, 158, 30], measuring barrier-free path (BFP) by dragging the membrane proteins across the cell surface with a laser tweezers until they encountered a barrier [159, 160], or directly observing the membrane skeleton by electron microscopy [161].

Table 5.1 summarizes some of the key experimental results obtained for various cell types using different techniques. As discussed in the previous chapter and also in table 5.1, a high percentage of the membrane proteins exhibit confined motion. Theory of the confined diffusion has been mostly studied by either running Monte-Carlo analysis or solving the related diffusion equation. Solution for diffusion equation in different confinement geometries was first derived in the context of heat conduction problem [162], which was later used to obtain an analytical form for the MSD of confined diffusion [162, 157, 163, 164].

The work presented in this chapter has been performed in collaboration with Frashad Abdollah-Nia (Colorado State University).

TABLE 5.1. Summary of the previous experimental results for characterizations of compartmentalization of the cell plasma membrane

Cell type	**Molecule**	**Technique**	**Main results**	**Year Ref.**
HEPA-OVA	MHC [a]	Laser tweezers	The BFPs of Qa2 and H-2Db are 1.7 ± 0.2 and 0.6 ± 0.1 (micrometers ± SEM), respectively. Barriers to lateral movement are primarily on the cytoplasmic half of the membrane and are dynamic.	1991 [159]
NRK [b]	TfR [c]	SPT	Most of the movement trajectories are of the confined diffusion type, within domains of =0.25 μm^2 (500-700 nm in diagonal length).	1994 [158]
NRK [b]	TfR [c]	Laser tweezers	Boundaries are elastic structures. Confinement size is 600-800 nm in diagonal length.	1995 [160]
NRK [b,*]	TfR [c,*]	SPT	More than 80% of the receptors exhibit confined+hopped diffusion. TfR diffusion was found to be doubly compartmentalized into 710 nm compartments and then into 260 nm compartments.	2002 [105]
NRK [b]and FRSK [d]	-	Electron tomography	Almost the entire cytoplasmic surface of the upper cell membrane is covered with the actin-based membrane skeleton. The median values of the compartments area and its square root are 3.9×10^4 nm^2 and 200 nm, respectively, for NRK cells and 2.7×10^3 nm^2 and 52 nm, respectively, for FRSK cells.	2006 [161]

[a] Major histocompatibility complex (MHC) class 1 molecules that were either transmembrane- (H-2Db) or glycosylphosphatidylinositol (GPI)-anchored (Qa2) were labeled with antibody coated gold particles.

[b] Normal rat kidney fibroblastic cell

[c] Transferrin receptors

[*] Other molecules diffusion on other cell type membrane are investigated in the same paper

[d] Fetal rat skin keratinocytes.

Predictions of scape time, number of visited sites before scape based on the confinement size and shape was derived using Monte-Carlo calculations [165]. In addition to diffusion in a single confined domain, diffusion in a lattice with periodic or random barriers with or without permeation has also been studied [166, 112, 167, 168, 169]. Here we investigate the problem of diffusion in a distribution of confinement sizes, which have been partially studied before for a specific distribution of confinement sizes [169], but needs a more detailed work and generalization to other distributions.

In this chapter first we briefly review the theory for confined diffusion. Then using some of the previous findings as a base of our model, we obtain a theoretical form for the MSD of diffusion in a distribution of compartment sizes assuming zero escape probability from the compartments. Then we calculate the MSD for three specific distributions of confinement sizes, namely exponential, power-law and log-normal distributions with linear (one dimensional) and circular (two dimensional) geometries. We also compare our theoretical results with simulations for verification purpose.

5.2. Theoretical model

First we review confined diffusion in a d-dimensional domain $\mathscr{L}$ with volume V and characteristic length L and reflecting boundary condition. Probability of finding a particle at position $\mathbf{r}$ at time t is shown by $P(\mathbf{r}, \mathbf{t})$. This probability depends on the initial position of the particle $\mathbf{r}'$ at time $t = 0$ and the confinement size L. The conditional probability, $P(\mathbf{r}, t|\mathbf{r}', L)$, satisfies the diffusion equation

$$\frac{\partial P}{\partial t} = D\nabla^2 P, \tag{16}$$

where D is the diffusion coefficient. Initial condition for this problem is given by $P(\mathbf{r}, t = 0|\mathbf{r}', L) = \delta(\mathbf{r} - \mathbf{r}')$. The solution for this diffusion equation with reflecting boundaries is known for some specific geometries. For example for linear 1D confined diffusion with coordinate x and initial position x', the solution is written as the following series [162]

$$P(x, t|x', L) = \frac{1}{L} + \frac{2}{L}\sum_{n=1}^{\infty} \exp\left[- \left(\frac{n\pi}{2}\right)^2 \frac{4Dt}{L^2}\right] \cos\left(\frac{n\pi x}{L}\right) \cos\left(\frac{n\pi x'}{L}\right). \tag{17}$$

For confined diffusion in a 2D circular domain with radius R, coordinate $\mathbf{r} = (\rho, \phi)$ and initial position $\mathbf{r}' = (\rho', \phi')$, the solution for the diffusion equation is also known and is written as a series [162]

$$\begin{aligned} P(\mathbf{r}, t|\mathbf{r}', R) = {} & \frac{1}{\pi R^2} \\ & + \frac{1}{\pi R^2} \sum_{n=-\infty}^{\infty} \cos n(\phi - \phi') \sum_{m=1}^{\infty} \frac{\alpha_{nm}^2}{\alpha_{nm}^2 - n^2} \exp\left[- \alpha_{nm}^2 \frac{Dt}{R^2}\right] \frac{J_n(\alpha_{nm}\frac{\rho}{a}) J_n(\alpha_{nm}\frac{\rho'}{a})}{J_n(\alpha_{nm})^2}, \end{aligned} \tag{18}$$

where α_{1m} are the (non-zero) zeros of the derivative of the Bessel function of the first kind, $j_1'(\alpha_{1m}) = 0$.

Ensemble-averaged (EA-MSD) for diffusion in a d-dimensional compartment with characteristic length L and volume V is given by

$$\begin{aligned} \left\langle \delta^2(t)|L \right\rangle = \left\langle (\mathbf{r}(t) - \mathbf{r}')^2 |L \right\rangle &= \int\int P(\mathbf{r}') P(\mathbf{r}, t|\mathbf{r}', L)(\mathbf{r} - \mathbf{r}')^2 \, \mathrm{d}^d\mathbf{r} \, \mathrm{d}^d\mathbf{r}' \\ &= \frac{1}{V} \int\int P(\mathbf{r}, t|\mathbf{r}', L)(\mathbf{r} - \mathbf{r}')^2 \, \mathrm{d}^d\mathbf{r} \, \mathrm{d}^d\mathbf{r}', \end{aligned} \tag{19}$$

where we assume a uniform probability distribution for the initial position, $P(\mathbf{r}') \, \mathrm{d}^d\mathbf{r}' = \mathrm{d}^d\mathbf{r}'/V$. Therefore the MSD for a 1D linear confined diffusion in compartment with size L

and reflecting boundaries is obtained by substituting Eq. 17 in Eq. 19 [157],

$$\left\langle \delta^2(t)|L\right\rangle = \frac{L^2}{6}\left(1-\frac{96}{\pi^4}\sum_{n=0}^{\infty}\exp\left[-\pi^2(2n+1)^2\frac{DT}{L^2}\right]\frac{1}{(2n+1)^4}\right), \tag{20}$$

where the initial position is assumed to be uniformly distributed inside the linear domain, $P(x')=1/L$. Equation 20 can be approximated by

$$\left\langle \delta^2(t)|L\right\rangle \approx \frac{L^2}{6}\left(1-\exp\left[\frac{-12Dt}{L^2}\right]\right). \tag{21}$$

For short times, $t \ll L^2/D$, we have $\langle \delta^2(t)|L\rangle \approx 2Dt$, and diffusion is a normal Brownian motion. For long time limit, $t \gg L^2/D$, the MSD converges a constant value, $\langle \delta^2(t)|L\rangle \approx L^2/6$. Therefore the confinement size can be calculated using the MSD of the motion.

Similarly EA-MSD for 2D diffusion confined in circular compartments is obtained by substituting Eq. 18 in Eq. 19 [170, 164]

$$\left\langle \delta^2(t)|R\right\rangle = R^2\left(1-8\sum_{m=1}^{\infty}\exp\left[-\alpha_{1m}^2\frac{Dt}{R^2}\right]\frac{1}{\alpha_{1m}^2(\alpha_{1m}^2-1)}\right), \tag{22}$$

where the initial position is assumed to be uniformly distributed inside the circular domain. Equation (22) can be approximated by

$$\left\langle \delta^2(t)|R\right\rangle \approx R^2\left(1-e^{\frac{-4Dt}{R^2}}\right). \tag{23}$$

For short times, $t \ll R^2/D$, we have $\langle \delta^2(t)|R\rangle \approx 4Dt$, and diffusion is a normal Brownian motion. For long time limit, $t \gg R^2/D$, the MSD converges a constant value, $\langle \delta^2(t)R\rangle \approx R^2$, that depends on the confinement size.

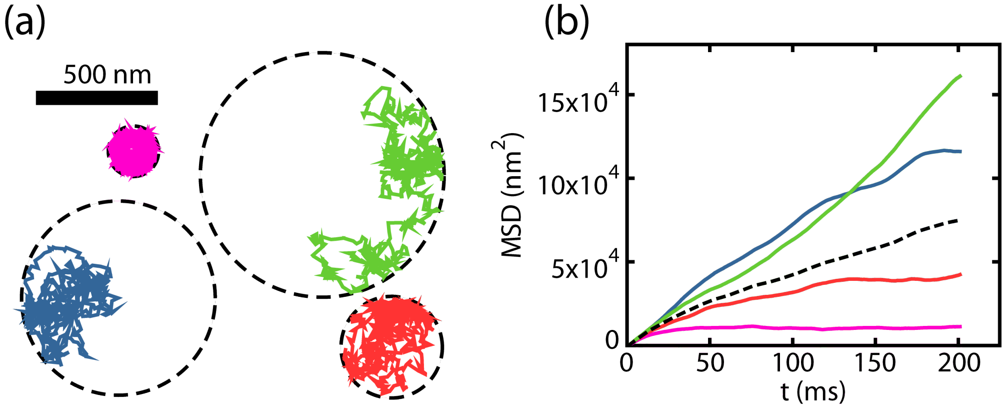

FIGURE 5.1. Illustration of the modeled system. (a) Trajectories of confined diffusion in circular domains with different confinement lengths. (b) Mean square displacement of the trajectories shown in (a). The dashed line shows the ensemble-averaged MSD for the illustrated trajectories.

Here we wish to study the diffusion in a meshwork with a distribution of confinement sizes, $P(L)$. Figure 5.1(a) illustrates the modeled system. Each trajectory is confined within a domain with a specific size and the escape probability is zero. Even if in a real system the particles are able to escape from confinement, the zero scape probability assumption is still reasonable if the average survival time of the particles inside compartments is larger than the measurement time. For this case the EA-MSD of 1D diffusion in a distribution of confinement sizes is

$$\left\langle \delta^2(t) \right\rangle = \int_0^\infty \left\langle \delta^2(t) | L \right\rangle P(L) \, \mathrm{d}L. \tag{24}$$

and for 2D case the only difference is that the L needs to be replaced by R. Figure 5.1(b) shows the MSD of each trajectory shown in fig. 5.1(a) as well as the EA-MSD of the four individual MSD trajectories. In this manuscript we calculate the EA-MSD for diffusion in linear and circular domains with a exponential, Pareto and log-normal size distributions. From now on we will refer to EA-MSD as MSD for simplicity of notation.

5.3. One dimensional (1D) diffusion

The exact form of the MSD for 1D diffusion in a distribution of confinement sizes, $P(L)$, is obtained by substitution of the Eq. 20 in Eq. 24

$$\left\langle \delta^2(t) \right\rangle = \int_0^\infty \frac{L^2}{6}\left(1 - \frac{96}{\pi^4}\sum_{n=0}^{\infty} \exp[-\pi^2(2n+1)^2\frac{DT}{L^2}]\frac{1}{(2n+1)^4}\right)P(L)dL \tag{25}$$

and the approximate form is given by substitution of the Eq. 21 in Eq. 24

$$\left\langle \delta^2(t) \right\rangle = \int_0^\infty \frac{L^2}{6}\left(1 - \exp\left(\frac{-12Dt}{L^2}\right)\right)P(L)dL. \tag{26}$$

In the next three sections we compare the obtained theoretical MSD with the simulation result for three distribution of confinement sizes: exponential, Pareto and log-normal. We also obtain the asymptotic behavior of the MSD in each case.

Exponential distribution of confinement sizes (1D) : The first distribution that we investigate is exponential distribution of confinement sizes:

$$P(L) = \frac{1}{\lambda}e^{-L/\lambda} \tag{27}$$

By substituting this distribution into either the exact or approximate form of the MSD, given by Eq. (25) and Eq. (26) respectively, we can obtain the MSD. Both integrals can be solved numerically. In Fig. 5.2(a) we compare the exact and approximate theoretical MSDs to the simulation results and observe good agreement between theory and simulation (Parameters used in simulation and theory: time interval for each step $\Delta t = 1$ ms, standard deviation of step size $\sigma = 20$ nm, diffusion coefficient $D = \sigma^2/2\Delta t = 200$ nm^2/ms, $\lambda = 450$

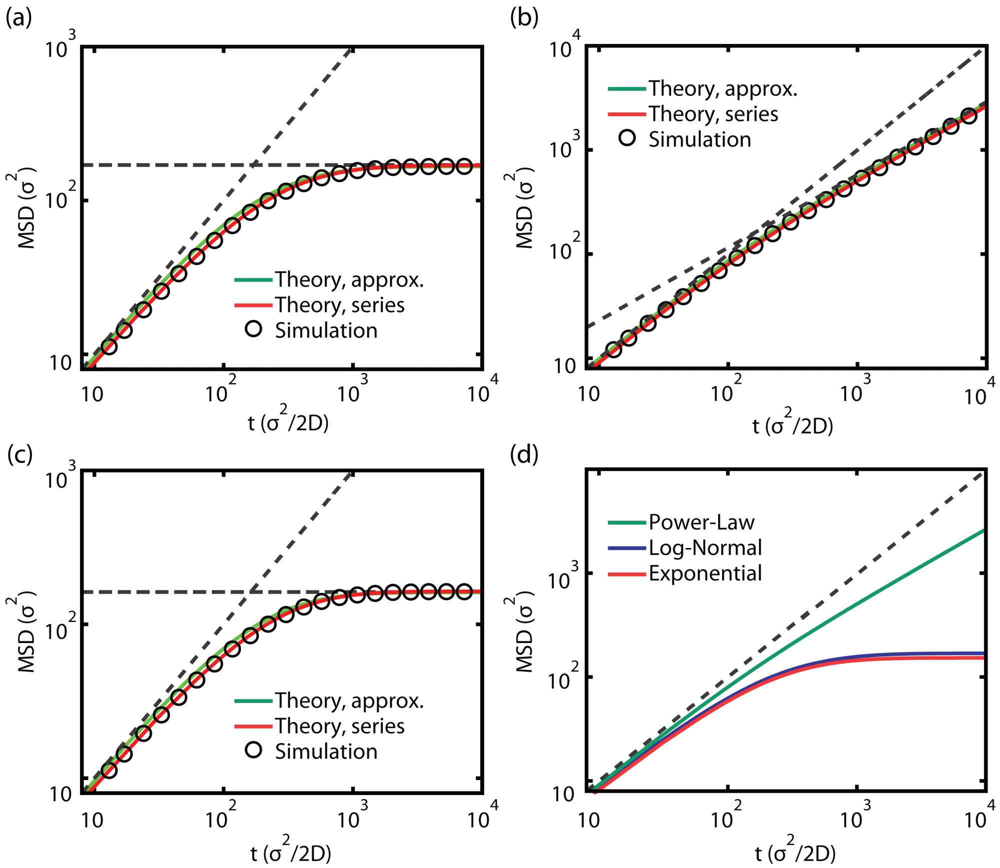

FIGURE 5.2. MSD for confined diffusion in linear domains. MSD for confined diffusion in linear domains for (a) exponential ($\lambda = 0.005$, $L_{min} = 20\sigma$), (b) Pareto ($\alpha = 0.6$, $L_{min} = 20\sigma$) and (c) log-normal ($\gamma = 0.25$, $\mu = 6.4$) distribution of confinement sizes. Red line: the approximate solution (Eq. (38)). Green line: exact solution using the first 100 terms of Eq. (37). Circles: Simulation results (10^5 trajectories). Dashed line in (a), (b) and (c): Asymptotic behavior of the MSDs. (d) Comparison of the MSDs of diffusion in the three distribution of confinement sizes. The dashed line shows MSD for the normal diffusion, MSD$\propto t$.

nm. Although the exact solution is closer to the simulation results, the approximate solution is only slightly off and can be used in empirical applications.

We also obtain the asymptotic behavior of the MSD using Eq. (26). We define a relaxation time $\tau_1 = \langle L \rangle^2 / 12D$ where $\langle L \rangle = \lambda = 450$ nm is the average confinement size For short times,

$t \ll \tau_1$, $e^{\frac{-12Dt}{L^2}} \approx 1 - \frac{12Dt}{L^2}$ and the MSD becomes:

$$\left\langle \delta x^2(t) \right\rangle = \frac{2Dt}{\lambda} \int_0^\infty e^{-L/\lambda} dL = 2Dt. \tag{28}$$

Since for short times the random walker does not feel the effect of the walls and diffusion is normal Brownian motion, this result is not surprising. For long time limit, $t \gg \tau_1$, we have $1 - e^{\frac{-12Dt}{L^2}} \approx 1$ and MSD becomes:

$$\left\langle \delta x^2(t) \right\rangle = \frac{1}{6\lambda} \int_0^\infty L^2 e^{-L/\lambda} dL = \frac{\lambda^2}{3}, \tag{29}$$

this means for long times the MSD converges to a constant value that depends on the system parameter λ.

Pareto distribution of confinement sizes 1D : Another interesting distribution with possible empirical applications is power-law or Pareto distribution:

$$P(L) = \begin{cases} 0, & \text{if } L < L_{min} \\ \frac{\alpha L_{min}^\alpha}{L^{1+\alpha}}, & \text{if } L \geq L_{min}, \end{cases} \tag{30}$$

where $0 < \alpha \leq 1$. Similar to the exponential distribution, the exact and approximate MSD for 1D diffusion in this distribution of compartment sizes could be found using Eq. (25), Eq. (26) respectively, the results are shown in Fig. 5.2(b). Investigating the asymptotic behavior of MSD could also be very informative. For short times MSD becomes:

$$\left\langle \delta x^2(t) \right\rangle = 2Dt \int_{L_{min}}^\infty \frac{\alpha L_{min}^\alpha}{L^{1+\alpha}} dL = 2Dt, \tag{31}$$

as expected for a short time limit where the particle does not feel the effects of the barriers. In order to obtain the asymptotic behavior of the MSD for long times, we look at the analytical solution for MSD using the approximate form of the MSD, Eq. (26):

$$\begin{aligned}\langle \delta^2(t) \rangle &= \frac{\alpha L_{\min}^{\alpha}}{6} \int_{L_{\min}}^{\infty} L^{1-\alpha}(1 - e^{\frac{-12Dt}{L^2}})dL \\ &= \frac{\alpha L\text{min}^{\alpha}}{12}(12Dt)^{\beta}\Big(-\Gamma[-\beta] + \Gamma[-\beta, \frac{12Dt}{L_{\min}^2}]\Big) + \frac{\alpha}{2-\alpha}L_{\min}^2,\end{aligned} \tag{32}$$

where $\Gamma(z)$ and $\Gamma(z, a)$ are the complete and incomplete gamma functions respectively and $\beta = 1 - \alpha/2$. In Eq. (32) for $t \gg \frac{L_{\min}^2}{4D}$ the incomplete gamma function converges to zero and the MSD can be approximated by

$$\langle \delta^2(t) \rangle \approx -\frac{\alpha L_{\min}^{\alpha}}{12}(12Dt)^{\beta}\Gamma[-\beta], \tag{33}$$

therefore, for long times the MSD scales as $t^{\beta} = t^{1-\alpha/2}$.

Log-normal distribution of confinement sizes 1D : The log-normal distribution is characterized as a sub-exponential or heavy-tailed distribution in the sense that the tail of the distribution decreases more slowly than any exponential tail [138].

$$P(L) = \frac{1}{L\gamma\sqrt{2\pi}} \exp\Big[-\frac{(\ln(L) - \mu)^2}{2\gamma^2}\Big]. \tag{34}$$

Exact and approximate forms of the MSD is obtained using Eq. (25), Eq. (26) respectively. Theoretical and simulation results are shown in Fig. 5.2(c). The parameters used in simulation and theory are: $\Delta t = 1$ ms, $\sigma = \sqrt{2D\Delta t} = 20$ nm, $\mu = 5.8$, $\gamma = 0.8$. For this distribution the average confinement size is $\langle L \rangle = \exp{(\mu + \gamma^2/2)} \simeq 450$ nm.

For short times, $t \ll \tau$, we have $e^{\frac{-4Dt}{L^2}} \approx 1 - \frac{4Dt}{L^2}$ and the MSD becomes:

$$\left\langle \delta^2(t) \right\rangle = \frac{2Dt}{\gamma\sqrt{2\pi}} \int_0^\infty \frac{\exp(-\frac{(\ln(L)-\mu)^2}{2\gamma^2})}{L} dL = 2Dt. \tag{35}$$

For $t >> \tau$ we have : $1 - e^{\frac{-4Dt}{L^2}} \approx 1$ and the MSD is:

$$\left\langle \delta^2(t) \right\rangle = \frac{1}{6\gamma\sqrt{2\pi}} \int_0^\infty L \exp(-\frac{(\ln(L)-\mu)^2}{2\gamma^2}) dL = \frac{\exp\left(2\gamma^2 + 2\mu\right)}{6}, \tag{36}$$

this means that for long times the MSD converges to a constant value that depends on the distribution parameters γ and μ.

5.4. Two dimensional (2D) diffusion

The exact form of the MSD for confined diffusion in circular domain with a distribution of confinement radii, $P(R)$, is obtained by substitution of the Eq. 22 in Eq. 24

$$\left\langle \delta^2(t) \right\rangle = \int_0^\infty R^2 \left(1 - 8 \sum_{m=1}^{\infty} \exp\left[-\alpha_{1m}^2 \frac{Dt}{R^2}\right] \frac{1}{\alpha_{1m}^2(\alpha_{1m}^2 - 1)}\right) P(R) dR. \tag{37}$$

And the approximate form is obtained by substitution of the Eq. 23 in Eq. 24

$$\left\langle \delta^2(t) \right\rangle = \int_0^\infty R^2 \left(1 - e^{\frac{-4Dt}{R^2}}\right) P(R) dR. \tag{38}$$

In the next three sections we compare the obtained theoretical MSD with the simulation result for three distribution of confinement sizes: Normal, Pareto and log-normal. We also obtain the asymptotic behavior of the MSD in each case.

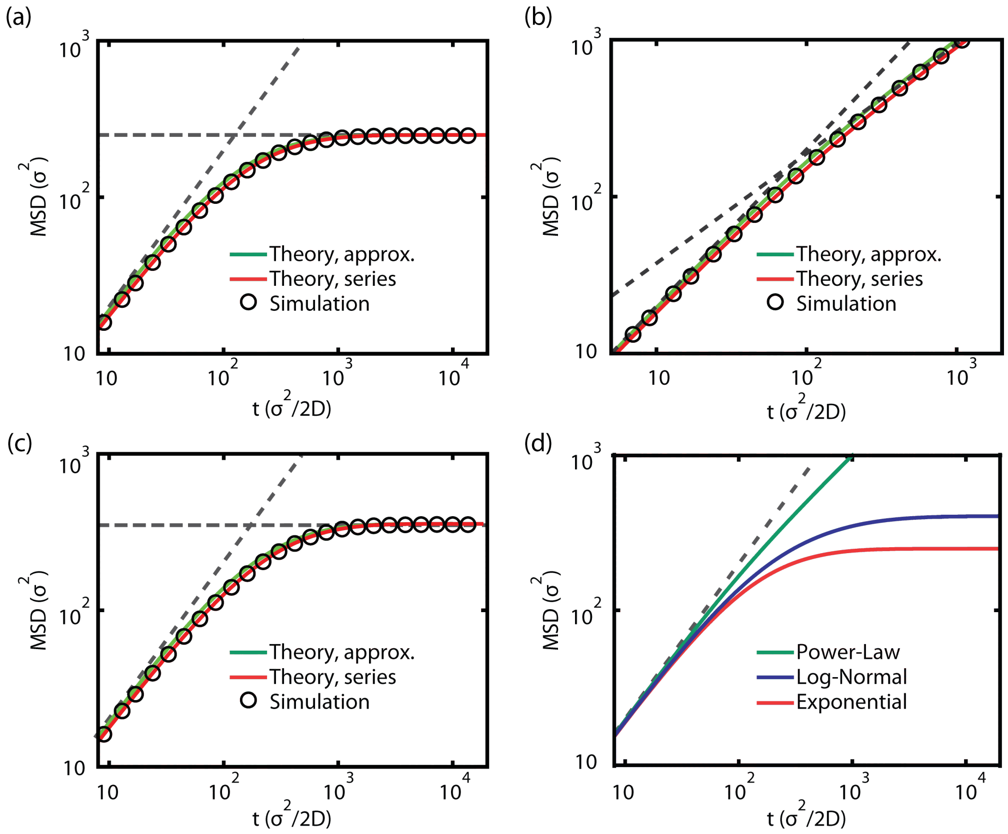

Figure 5.3. MSD for confined diffusion in circular domains. MSD for confined diffusion in circular domains for (a) exponential ($\lambda = 0.01$, $R_{min} = 10\sigma$), (b) Pareto ($\alpha = 0.6$, $R_{min} = 10\sigma$) and (c) log-normal ($\mu = 5.5$, $\gamma = 0.66$) distribution of confinement sizes. Red line: the approximate solution (eq. (38)). Green line: exact solution using the first 100 terms of eq. (37). Circles: Simulation results (10^5 trajectories). Dashed line in (a), (b) and (c): Asymptotic behavior of the MSDs. (d) Comparison of the MSDs of diffusion in the three distribution of confinement sizes. The dashed line shows MSD for the normal diffusion, MSD$\propto t$.

Exponential distribution of confinement radii : The first case that we investigate is diffusion in an exponential distribution of radii of circular confinement domains:

$$P(R) = \frac{1}{\lambda} e^{-R/\lambda}. \tag{39}$$

By substituting this distribution into either the exact or approximate form of the MSD, given by Eq. (37) and Eq. (38) respectively, we can obtain the MSD. Both integrals can be solved numerically. In Fig. 5.3(a) we compare the exact and approximate theoretical MSDs to the simulation results and observe good agreement between theory and simulation (Parameters used in simulation and theory: time interval for each step $\Delta t = 1$ ms, standard deviation of step size in x and y direction= 20 nm, diffusion coefficient $D = \sigma^2/2\Delta t = 200$ nm^2/ms, $\lambda = 200$ nm. Although the exact solution is closer to the simulation results, the approximate solution is only slightly off and can be used in empirical applications.

We also obtain the asymptotic behavior of the MSD using Eq. (38). We define a relaxation time $\tau = \langle R \rangle^2 / 4D$ where $\langle R \rangle = \lambda = 200$ nm is the average confinement size. For short times, $t \ll \tau$, we have $e^{\frac{-4Dt}{R^2}} \approx 1 - \frac{4Dt}{R^2}$ and the MSD becomes:

$$\left\langle \delta^2(t) \right\rangle = \frac{4Dt}{\lambda} \int_0^\infty e^{-R/\lambda} dR = 4Dt. \tag{40}$$

Since for short times the particle does not feel the effect of the confinement and diffusion is a free Brownian motion, this result is not surprising. For long time limit, $t \gg \tau$, we have : $1 - e^{\frac{-4Dt}{R^2}} \approx 1$ and the MSD becomes:

$$\left\langle \delta^2(t) \right\rangle = \frac{1}{\lambda} \int_0^\infty R^2 e^{-R/\lambda} dR = 2\lambda^2. \tag{41}$$

This means for long times the MSD converges to a constant value that depends on the distribution parameter λ.

Pareto distribution of confinement radii : Another interesting distribution that has potential for empirical applications is the power-law or Pareto distribution:

$$P(R) = \begin{cases} 0, & \text{if } R < R_{\text{min}}. \\ \frac{\alpha R_{\text{min}}^{\alpha}}{R^{1+\alpha}}, & \text{if } R \geq R_{\text{min}}, \end{cases} \tag{42}$$

where $\alpha \in (0, 1]$. Similar to the exponential distribution, the exact and approximate MSD for diffusion in this distribution of compartment sizes can be obtained by substituting $P(R)$ in Eqs. (37) and (38). The results are shown in Fig. 5.3(b).

Investigating the asymptotic behavior of MSD can also be very informative. For short times, $t << R_{\text{min}}^2/4D$, MSD becomes:

$$\left\langle \delta^2(t) \right\rangle = 4Dt \int_{R_{\text{min}}}^{\infty} \frac{\alpha R_{\text{min}}^{\alpha}}{R^{1+\alpha}} dR = 4Dt, \tag{43}$$

as expected for a short time limit where the particle does not feel the effects of the barriers. In order to obtain the asymptotic behavior of the MSD for long times, we look at the analytical solution for MSD using the approximate form of the MSD, Eq. (38):

$$\begin{aligned} \left\langle \delta^2(t) \right\rangle &= \alpha R_{\text{min}}^{\alpha} \int_{R_{\text{min}}}^{\infty} R^{1-\alpha} (1 - e^{\frac{-4Dt}{R^2}}) dR \\ &= \frac{\alpha R\text{min}^{\alpha}}{2} (4Dt)^{\beta} \Big(- \Gamma[-\beta] + \Gamma[-\beta, \frac{4Dt}{R_{\text{min}}^2}] \Big) + \frac{\alpha}{2-\alpha} R_{\text{min}}^2, \end{aligned} \tag{44}$$

where $\Gamma(z)$ and $\Gamma(z, a)$ are the complete and incomplete gamma functions respectively and $\beta = 1 - \alpha/2$. In Eq. (44) for $t >> \frac{R_{\text{min}}^2}{4D}$ the incomplete gamma function converges to zero and the MSD can be approximated by

$$\left\langle \delta^2(t) \right\rangle \approx -\frac{\alpha R_{\text{min}}^{\alpha}}{2} (4Dt)^{\beta} \Gamma[-\beta], \tag{45}$$

therefore, for long times the MSD scales as $t^{\beta} = t^{1-\alpha/2}$.

Log-normal distribution of confinement radii : The log-normal distribution is characterized as a sub-exponential or heavy-tailed distribution in the sense that the tail of the distribution decreases more slowly than any exponential tail [138].

$$P(R) = \frac{1}{R\gamma\sqrt{2\pi}} \exp\left[-\frac{(\ln(R)-\mu)^2}{2\gamma^2} \right]. \tag{46}$$

Exact and approximate forms of the MSD is obtained by replacing this distribution into Eqs. (37) and (38) respectively. Theoretical and simulation results are shown in Fig. 5.3(c). The parameters used in simulation and theory are: $\Delta t = 1$ ms, $\sigma = \sqrt{2D\Delta t} = 20$ nm, $\mu = 4.7$, $\gamma = 1.1$. For this distribution the average confinement size is $\langle R \rangle = \exp\left(\mu + \gamma^2/2\right) \simeq 200$ nm.

For short times, $t \ll \tau$, we have $e^{\frac{-4Dt}{R^2}} \approx 1 - \frac{4Dt}{R^2}$ and the MSD becomes:

$$\left\langle \delta^2(t) \right\rangle = \frac{4Dt}{\gamma\sqrt{2\pi}} \int_0^{\infty} \frac{\exp(-\frac{(\ln(R)-\mu)^2}{2\gamma^2})}{R} dR = 4Dt. \tag{47}$$

For $t >> \tau$ we have : $1 - e^{\frac{-4Dt}{R^2}} \approx 1$ and the MSD becomes:

$$\left\langle \delta^2(t) \right\rangle = \frac{1}{\gamma\sqrt{2\pi}} \int_0^{\infty} R \exp(-\frac{(\ln(R)-\mu)^2}{2\gamma^2}) dR = \exp\left(2\gamma^2 + 2\mu\right) \tag{48}$$

this means that for long times the MSD converges to a constant value that depends on the distribution parameters γ and μ.

5.5. Discussion

Here we obtain a theoretical form for the MSD of diffusion in a distribution of confinement sizes. We calculated the MSD for three different distributions : exponential, Pareto and log-normal. We observed that for diffusion in circular domains the exponential and log-normal distribution of confinement sizes would result to different MSD curves even if they have the same average value. However for the case of the confined linear diffusion the tail of the log-normal distribution did not have a considerable effect on the MSD. By investigating the role of distribution of confinement sizes, we hope to assist future works which aim to obtain a full theoretical model for the highly complex problem of diffusion on the cell membrane.

5.6. Methods

5.6.1. Simulation. In order to verify the obtained theoretical model, we performed simulations of diffusion in various distributions of confinement sizes. In our simulations, written in MATLAB, each trajectory is a 1D or 2D random walk where the x and y components of each step are drawn from a normal distribution $N(0, \sigma^2)$. Each trajectory is confined in a linear domain with size L drawn from the distribution $P(L)$ for 1D case or in a circular domain with radius R drawn from the distribution $P(R)$ for 2D diffusion. Distribution of confinement sizes were generated using the inverse transform sampling method. Since our theory is developed starting from a continues diffusion equation, Eq. (16), the minimum compartment size has to be much larger than the standard deviation of the simulation step size. In this work we assume L_{min} and R_{min} is 10σ. The diffusion coefficient, D, is calculated from σ using the equation $\sigma^2 = 2D\Delta t$ where Δt is the time length for one step. In order to make the results generally applicable, all of the lengths and times are given in units of σ and $\sigma^2/2D$ respectively. Every trajectory starts from a uniformly distributed random initial position inside the confinement domain. Reflective boundary conditions were applied to impose confined diffusion.

CHAPTER 6

PLASMA MEMBRANE PROTEIN DYNAMICS AT THE KV2.1/ER/PM JUNCTION

6.1. Introduction

The endoplasmic reticulum (ER) is the largest organelle in the cell stretching from the nuclear envelope to the cell cortex in a system of tubules and sheets (cisterns) [171]. Morphology of the ER complex in animal cells is shaped by several mechanisms including the association with microtubules and molecular motors and it is stabilized by integral ER membrane proteins [172]. Even though the interface between ER and actin cytoskeleton is not very well understood, it is recognized that the actin cytoskeleton plays important roles in the regulation of ER morphology [173, 174, 175]. More importantly, it has been shown that a dense cortical actin network is crucial to stabilize the ER/PM junctions [176, 177]. Furthermore, the actin-associated motors myosin-Ic (myo1c) and myosin-Va have been shown to play important roles in the ER-actin interface in mammalian cells [178]. Therefore it seems possible that in addition to directly compartmentalizing the plasma membrane, which was studied in chapter 4, actin skeleton and associated proteins have a indirect role in regulating membrane dynamics by shaping the ER/PM junctions morphology.

In animal cells, ER is the primary storage site for intracellular Ca^{2+} that can be released as Ca^{2+} signals. The generation of Ca^{2+} signals is typically controlled by communication mechanisms between the ER and the surface of the cell, i.e., the plasma membrane (PM) [34]. As a consequence, endoplasmicER/PM contact sites are prevalent structures across different cell types, and they have essential functions in Ca^{2+} signaling and lipid trafficking [35]. The

---

The work in this chapter has been performed in collaboration with Michael Tamkun. The CD4 experiments, used in section 6.2.2, were performed by Yaping Moshier.

ER/PM junctions also function as trafficking hubs for insertion and removal of plasma membrane proteins suggesting a coupling mechanism between Ca^{2+} signals and protein traffic regulation [36]. Furthermore, it has been observed that the voltage gated potassium channel Kv2.1 aggregates and interacts with the endoplasmic reticulum, dramatically increasing ER/PM junction surface area and structurally changing the junction morphology [37]. Interactions of the potassium channel Kv2.1 with the ER/PM junctions on the cell membrane brings up an interesting question : whether other membrane proteins also interact with the ER/PM junctions.

In this chapter we first study the regulation of the cortical actin-myosin meshwork and observed that the inhibition of the myosin proteins decreases the mobility of the Kv2.1/ER/PM junctions. Furthermore, using single particle tracking and imaging Kv2.1 enriched ER/PM junction, we show that two membrane proteins, ADRB2 (a G protein-coupled receptor that mediates cellular responses) and the glycoprotein CD4, aggregate at Kv2.1/ER/PM junctions.

6.2. Results

6.2.1. Inhibition of the Myosin II motor protein decreases the mobility of Kv2.1 clusters. The actin cytoskeleton is a highly dynamic structure where remodeling is continuously taking place by the concerted action of nucleators (e.g., formin and Arp2/3 complex), molecular motors that induce contractility (e.g., myosin II), cross-linkers (e.g., filamin) severing proteins (e.g., ADF/cofilin), and proteins that regulate actin assembly (e.g., profilin). The mechanistic roles of the actin cytoskeleton in shaping the ER and regulating its dynamics in mammalian cells remain mostly unclear. Two types of proteins have been identified as key players in linking the actin cytoskeleton to the ER: formins [179, 180] and myosins

[175, 181]. The actin-associated motors myosin-Ic (myo1c) and myosin-Va have been shown to play important roles in the ER-actin interface in mammalian cells [178]. Comparison of the wide-field images of the ER before and after myo1c depletion, has shown that myo1c manipulations lead to loss of sheets and ER network distribution deficiency in Huh-7 cells [181].

Here we study the effect of inhibiting the activity of the myosin II motor protein by using the pharmacological reagent blebbistatin that specifically inhibits myoII activity [182]. We labeled the Kv2.1 channels with GFP and imaged the Kv2.1 clusters in control cells and also the cells treated with 10 μM blebbistatin [Figs. 6.1 (a) and (b)]. We did not observe any noticeable change in size distribution of the Kv2.1 clusters upon blebbistatin treatment as shown in Figs. 6.1 (c) and (d). We tracked the center of mass of the Kv2.1 clusters. Only the clusters that were clearly separated from other clusters during the movie were tracked as shown in Figs. 6.1 (a) and (b). Time average MSD, TA-MSD, was calculated using the following equation:

$$\overline{\delta^2(\Delta)} = \frac{1}{T-\Delta}\int_0^{T-\Delta} |\mathbf{r}(t+\Delta) - \mathbf{r}(t)|^2 \mathrm{d}t, \tag{49}$$

where T is the total experimental time, $\mathbf{r}$ the particle position, and Δ the lag time, i.e., the time difference over which the MSD is computed. Figures 6.1 (e) and (f) show the TA-MSD of the individual Kv2.1 clusters computed for lag times up to 100 frames or 3000 ms. When a particle displays Brownian diffusion, the MSD is linear in lag time, i.e., $\overline{\delta^2(\Delta)} = 2dD\Delta$, where D is the diffusion coefficient and d is the space dimension. In contrast, anomalous diffusion is characterized by a different MSD scaling, namely MSD $= 2dK_\alpha\Delta^\alpha$, where α is the anomalous exponent and K_α is the generalized diffusion coefficient. Anomalous diffusion

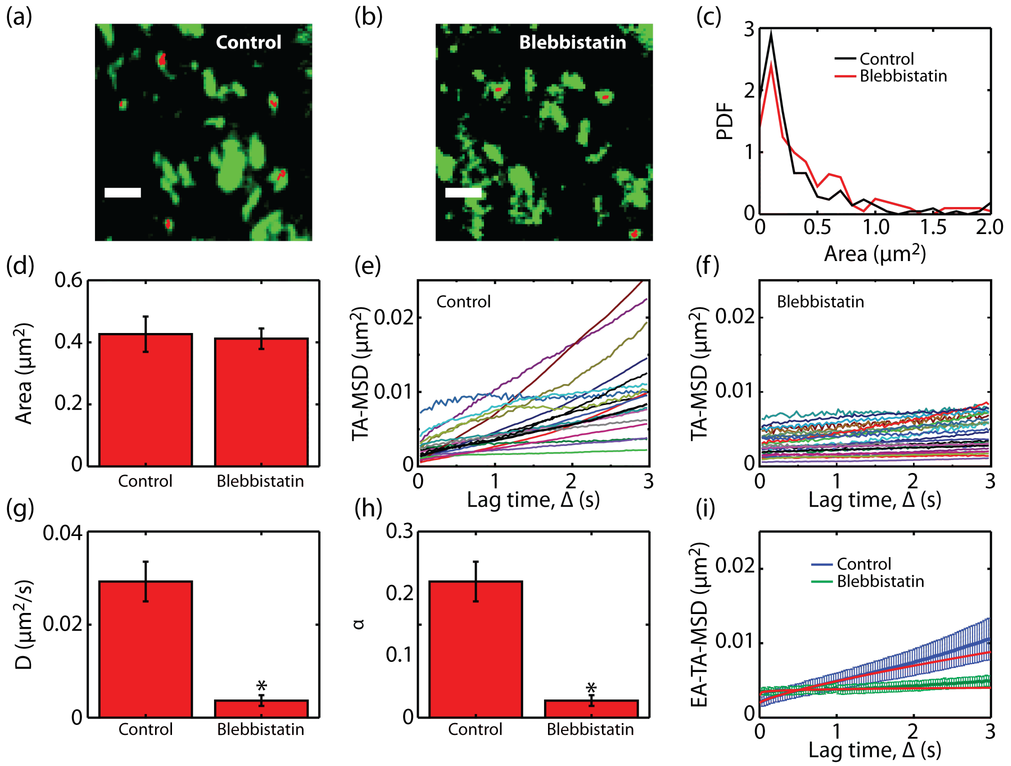

FIGURE 6.1. Effect of the myosin II depletions on morphology and mobility of Kv2.1/ER/PM junctions. (a) Kv2.1 cluster trajectories (in red) overlaid on the cluster image in control cells. Scale bar is 2 μm. (b) Kv.1 cluster trajectories (in red) overlaid on Kv2.1 cluster image in the same cell shown in (a) after treatment with 10 μ blebbistatin. Scale bar is 2 μm. (c) Distribution of Kv2.1 cluster in control cells (4 cells, 211 clusters) and cells treated with 10 μ blebbistatin (3 cells, 201 clusters). (d) Average Kv2.1 cluster area in control and blebbistatin treated cells. (e) TA-MSD of Kv2.1 clusters in control cells (4 cells, 20 clusters). (f) TA-MSD of Kv2.1 clusters in cells with 10 μM blebbistatin treatment (3 cells, 30 clusters). (g) Average diffusion coefficient of the trajectories shown in (e) and (f) for Kv2.1 clusters in control and blebbistatin treated cells. Error bars are standard error of the mean. Asterisks indicate differences with $p < 0.001$. (h) Average anomalous exponent, α, of the trajectories shown in (e) and (f) for Kv2.1 clusters in control and blebbistatin treated cells. Error bars are standard error of the mean. Asterisks indicate differences with $p < 0.001$. (i) Ensemble averaged TA-MSD of Kv2.1 clusters in control (4 cells, 20 clusters) and blebbistatin treated cells (3 cells, 30 clusters). Error bars indicate 95% confidence interval. Red lines show the fit of the first 1s, 33 frames, of the EA-TA-MSDs to the anomalous diffusion MSD equation plus error, $4K_\alpha\Delta^\alpha + \sigma^2$, where σ is the localization accuracy. For control cells $\alpha = 0.778$, $K_\alpha = 0.0007\ \mu m^2/s^{0.778}$ and $\sigma = 0.002\ \mu m^2$. For cells treated with 10 μ of blebbistatin $\alpha = 0.190$, $K_\alpha = 0.0002\ \mu m^2/s^{0.190}$ and $\sigma = 0.003\ \mu m^2$.

is classified as subdiffusion when $0 < \alpha < 1$ and superdiffusion when $\alpha > 1$. Mobility of the Kv2.1 clusters was characterized by diffusion coefficient and anomalous exponent. Diffusion coefficients were obtained by fitting a linear function to the first 10 points of the TA-MSDs, obtained from trajectories with minimum length equal to 20 frames, in linear MSD versus lag time plot, where the slope is $4D$. Anomalous exponent, α, was obtained by fitting a linear function to first 10 points of the TA-MSD versus lag time log-log plot where the slope is α. We observed that the diffusion coefficient and anomalous exponent of the Kv2.1 clusters dramatically decreases upon treatment with blebbistatin [Figures 6.1 (g) and (h)]. We obtained EA-TA-MSD by averaging over TA-MSD of all Kv2.1 cluster tracks before, 211 clusters in 4 cells, and after blebbistatin treatment, 201 clusters in 3 cells, as shown in Fig. 6.1 (i). In experimental data the MSD is always accompanied by a noise component originating from localization accuracy, namely, EA-TA-MSD= $4K_\alpha \Delta^\alpha + 4\sigma^2$, where σ is the localization accuracy. To find the noise level, we perform a linear extrapolation of the EA-TA-MSDs to the $\Delta = 0$ axis to find the y-axis intercept. We found that $4\sigma^2 = 0.002$ μm^2 for EA-TA-MSD of KV2.1 cluster tracks in control cell and $4\sigma^2 = 0.003$ μm^2 for EA-TA-MSD of cluster tracks in blebbistatin treated cells which corresponds to $\sigma = 22$ nm and $\sigma = 27$ nm cluster localization accuracy in these cells. Then we subtracted the noise level from the EA-TA-MSDs. Finally we fitted a linear function to EA-TA-MSD versus lag time log-log plot where slope is the anomalous exponent α and intercept is the logarithm of the generalized diffusion coefficient K_α multiplied by 4. We found that $\alpha = 0.778$ and $K_\alpha = 0.0007$ $\mu m^2/s^{0.778}$ for kv2.1 cluster EA-TA-MSD in control cells which were higher than $\alpha = 0.190$ and $K_\alpha = 0.0002$ $\mu m^2/s^{0.190}$ for kv2.1 cluster EA-TA-MSD in blebbistatin treated cells.

6.2.2. Aggregation of the membrane proteins on the Kv2.1/ER/PM junctions. As discussed in the introduction, we know that at least one membrane protein, Kv2.1 potassium channels, interact with the ER/PM junctions. The question that we want to address in this section is that whether other membrane proteins interact with the junctions as well. We chose two membrane proteins in order to study their interactions with th ER/PM junctions: the adrenergic receptor beta-2 (ADRB2) and cluster of differentiation 4 (CD4) which is a glycoprotein. ADRB2, is a well-characterized member of the G protein-coupled receptor family. ADRB2 senses epinephrine, a hormone and neurotransmitter, whose signaling, via a downstream L-type Ca^{2+} channel ($Ca_v1.2$) interaction, mediates physiologic responses such as smooth muscle relaxation [183]. It is known that the beta adrenergic receptors assemble with Cav1.2 channels to start the signaling cascade but the dynamics of this association and how these complexes relate to the Kv2.1/ER/PM junction is unknown. CD4 is a transmembrane receptor glycoprotein found on the surface of immune cells. CD4 has a very short cytoplasmic/intracellular tail [184]. Therefore, comparison between diffusion of CD4 with other membrane proteins with longer intracellular domains is a good control measurement for investigation of the effect of the intracellular structures, such as ER/PM junctions, on the membrane proteins diffusion. We simultaneously imaged Kv2.1 clusters, labeled with green fluorescent protein (GFP), and individual membrane proteins, either ADRB2 or CD4, labeled with either CF640 fluorescent protein or QDs, in order to study the interactions between the Kv2.1/ER/PM junctions and the membrane proteins. Figure 6.2 (a), (b) and (c) show a snapshot of the GFP tagged Kv2.1 clusters, a snapshot of the beta-2 adrenergic receptors and overlay of these two snapshots in one HEK293 cell respectively. Filtered and thresholded Kv2.1 cluster image in the cell shown in Fig. 6.2 (a) is shown in Fig. 6.2 (d).

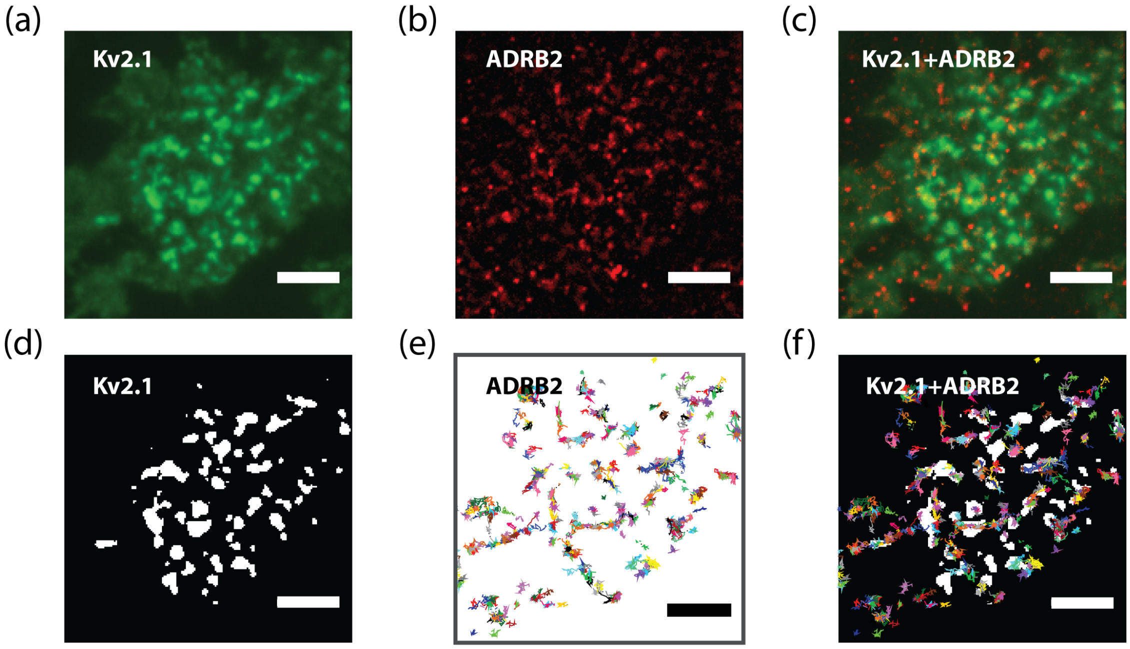

FIGURE 6.2. Kv2.1 clusters and beta receptors. (a) A snapshot of the GFP tagged Kv2.1 clusters in one HEK293 cell. (b) A snapshot of the beta-2 adrenergic receptors, ADRB2, labeled with CF640 in the same cell as (a). (c) Snapshot of Kv2.1 clusters shown in (a) overlaid on ADRB2 snapshot shown in (b). (d) Kv2.1 clusters shown in (a) detected using top-hat filter and a hard threshold. (e) Trajectories of the ADRB2. (f) Trajectories of ADRB2 overlaid on Kv2.1 clusters shown in white. Scale bars are 5 μm.

Individual membrane proteins were image and tracked in every frame. Trajectories of the beta-2 receptors in the cell shown in Fig. 6.2 (a) are shown in Fig. 6.2 (e). Then the trajectories were overlaid on the thresholded Kv2.1 cluster image [Fig. 6.2 (f)]. Similarly, Figs. 6.3 (a), (b) and (c) show a snapshot of the GFP tagged Kv2.1 clusters, a snapshot of the CDF glycoproteins and overlay of these two snapshots in one HEK293 cell respectively. Filtered and thresholded Kv2.1 cluster image in the cell shown in Fig. 6.3 (a) is shown in Fig. 6.3 (d). Individual CDF glycoproteins were image and tracked in every frame. Trajectories of the CD4 in the cell shown in Fig. 6.3 (a) are shown in Fig. 6.3 (e). Then the trajectories were overlaid on the thresholded Kv2.1 cluster image [Fig. 6.3 (f)].

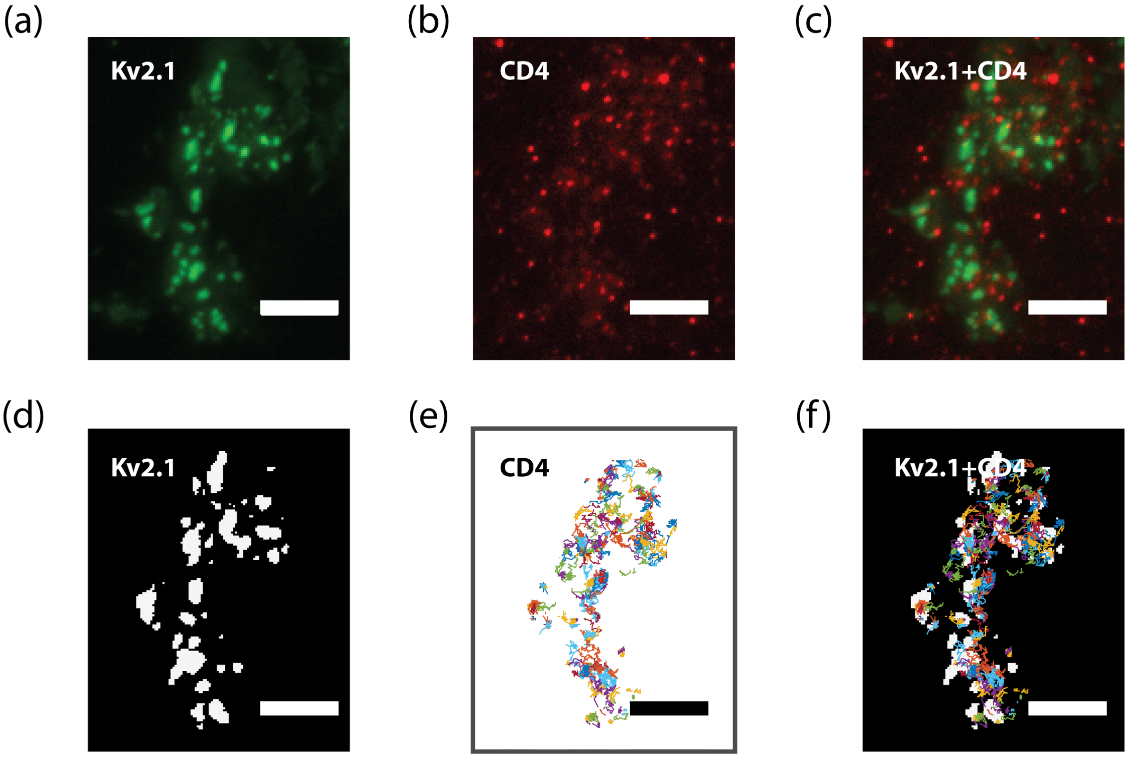

FIGURE 6.3. Kv2.1 clusters and CD4 glycoproteins. (a) A snapshot of the GFP tagged Kv2.1 clusters in one HEK293 cell. (b) A snapshot of the CD4 glycoproteins labeled with QDs in the same cell as (a). (c) Snapshot of Kv2.1 clusters shown in (a) overlaid on CD4 snapshot shown in (b). (d) Kv2.1 clusters shown in (a) detected using top-hat filter and a hard threshold. (e) Trajectories of the CD4 glycoproteins. (f) Trajectories of CD4 overlaid on Kv2.1 clusters shown in white. Scale bars are 5 μm.

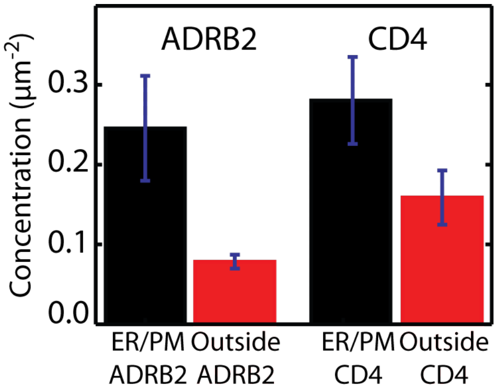

FIGURE 6.4. Concentration of the ADRB2 (4 cells) and CD4 (6 cells) membrane proteins on ER/PM junctions and outside the junctions. Error bars indicate standard error of mean.

Detected positions of membrane proteins were characterized as "on" and "off" cluster if the detected positions were inside or outside clusters respectively. We observed that the concentration of both ADRB2 and CD4 proteins are higher on the Kv2.1 clusters, 0.25 ± 0.07 μm^{-2}, compared to 0.08 ± 0.01 μm^{-2} off cluster for the beta receptors and 0.28 ± 0.05 μm^{-2} on cluster compared to 0.16 ± 0.03 μm^{-2} off cluster for the CD4 glycoproteins, which means that these proteins aggregate within Kv2.1/ER/PM junctions [Fig. 6.4]. The observed difference between the concentration of the membrane proteins on and off Kv2.1 cluster is higher for ADRB2 compared to CD4 proteins. This could be caused by the longer ADRB2 intracellular domain in comparison to the short CD4 intracellular tail.

We also compared the mobility of the beta receptors inside and outside clusters. Figures 6.5 (a) and 6.5 (b) show the TA-MSD for ADRB2 inside and outside Kv2.1 clusters which were calculated using Eq. 49 for trajectories with minimum length equal to 20 frames or 1s. Figure 6.5 (c) shows the distribution of on and off cluster trajectory lengths. Average trajectory length is 2.5 ± 0.4 s , mean ± SE, for on cluster tracks ($n = 661$ tracks) and 2.6 ± 0.3 s for off cluster tracks ($n = 1440$ tracks). We obtained EA-TA-MSD by averaging over TA-MSD of all on cluster tracks, 661 trajectories in 4 cells, and off cluster tracks, 1440 trajectories in 4 cells, as shown in Fig. 6.5 (d). As explained before, we calculated the noise for the EA-TA-MSD and found that $4\sigma^2 = 0.003$ μm^2 for both on cluster and cluster tracks which corresponds to $\sigma = 27$ nm localization accuracy. Then we subtracted the noise level from the EA-TA-MSDs and fitted a linear function to EA-TA-MSD versus lag time log-log plot where slope is the anomalous exponent α and intercept is the logarithm of the generalized diffusion coefficient K_α multiplied by 4. We found that $\alpha = 0.95$ and $K_\alpha = 0.09$ $\mu m^2/s^{0.95}$ for off cluster tracks and $\alpha = 0.90$ and $K_\alpha = 0.05$ $\mu m^2/s^{0.90}$ for on cluster tracks.

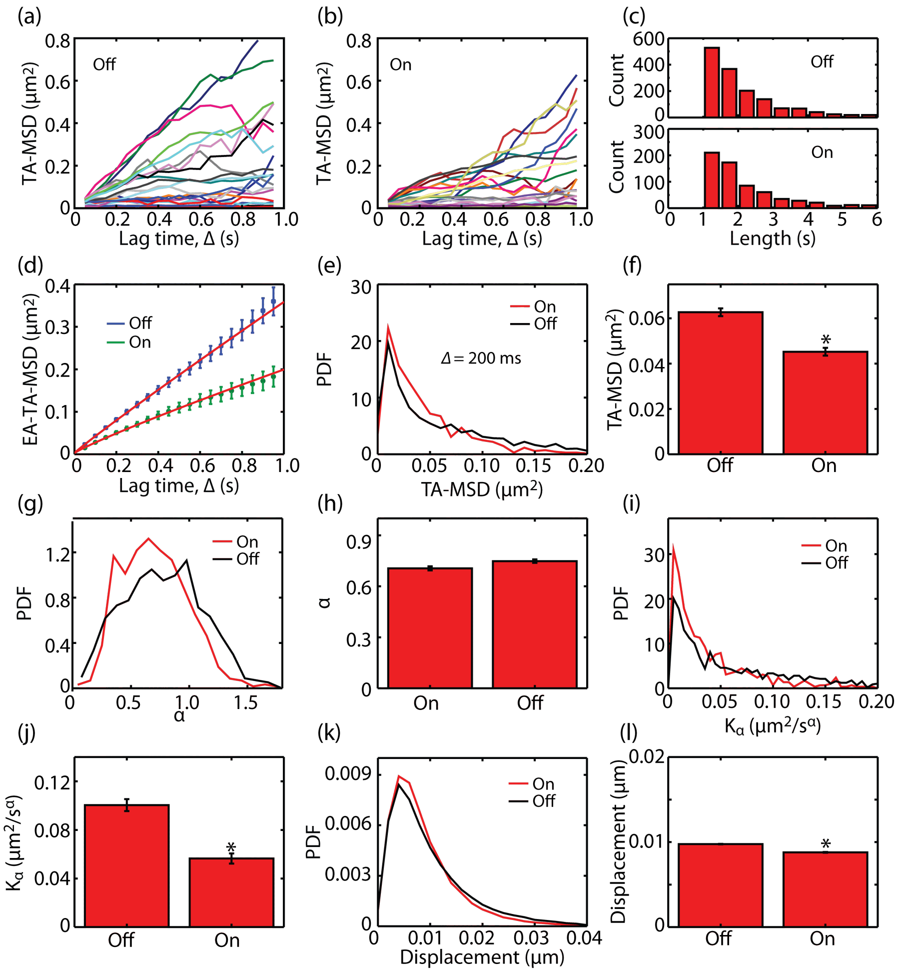

FIGURE 6.5. Comparison of diffusion of the beta receptors on and off Kv2.1 clusters. (a) TA-MSD of 20 ADRB2 trajectories that are outside, off, Kv2.1 cluster. (b) TA-MSD of 20 ADRB2 trajectories that are inside, on, Kv2.1 cluster. (d) Ensemble averaged TA-MSD of ADRB2 trajectories on (4 cells, 661 trajectories) and off (4 cells, 1440 trajectories) Kv2.1 cluster. Error bars indicate 95% confidence interval. Red lines show the fit of the EA-TA-MSDs to the anomalous diffusion MSD equation plus error, $4K_\alpha\Delta^\alpha + 4\sigma^2$, where σ is the localization accuracy. (e) PDF of the MSDs of ADRB2 trajectories calculated at lag time $\Delta = 200$ ms for the trajectories on cluster (4 cells, 661 trajectories) and off cluster (4 cells, 1400 trajectories). (f) Average MSD at lag time $\Delta = 200$ ms for the same trajectories as (e). (g) PDF of the anomalous exponent, α, for the same ADRB2 trajectories as (e). (h) Average α for the same ADRB2 trajectories as (g). (i) PDF of the generalized diffusion coefficient, K_α or the same ADRB2 trajectories as (e). (j) Average K_α for the same ADRB2 trajectories as (i). (k) PDF of the displacements during one frame, 50 ms, for the trajectories on cluster (4 cells, 661 trajectories, 29149 displacements in total) and off cluster (4 cells, 1400 trajectories, 75340 displacements in total). (l) Average displacement for one frame, 40 ms, for the same trajectories as (k). Error bars are standard error of the mean. Asterisks indicate differences with $p < 0.001$.

Figures 6.5 (e) and 6.5 (f) show that the time average MSD, Eq. 13, calculated at lag time $\Delta = 200$ ms is significantly lower for trajectories that are inside clusters. We fit a linear function to first 10 points of the TA-MSD versus lag time log-log plot of the individual tracks, the slope gave us the α value and the intercept was the logarithm of the $4K_\alpha$. Anomalous exponent α is similar for trajectories on and off Kv2.1 clusters [Figs. 6.5 (g) and 6.5 (h)] which means that the beta receptors undergo the same type of diffusion on and off clusters. We also observed that the generalized diffusion coefficient, K_α, is significantly lower for the receptors on cluster [Figs. 6.5 (i) and 6.5 (j)]. Moreover, the distribution of the beta receptor displacement shift significantly towards lower values for the receptors that are on Kv2.1 clusters, as shown in Figs. 6.5 (k) and 6.5 (l).

6.3. Discussion

We found that the mobility of the Kv2.1 clusters is drastically affected by inhibition of the myosin II motor protein. This finding proves the direct effect of the actin structure, and associated proteins, on formation and dynamics of the Kv2.1/ER/PM junctions. We also observed that different membrane proteins aggregate on the Kv2.1/ER/PM junctions, probably functioning as sites where endocytic cargoes are sorted. There are different possible reasons for this observation. One of the possible mechanisms is that the diffusion is slower within the junctions causing the membrane proteins to spend more time inside the clusters compared to outside. We proved this possibility by looking at the diffusion rate inside and outside junctions. Further experiments are necessary in order to elucidate the mechanism behind diffusion hindrances on ER/PM junctions.

BIBLIOGRAPHY

[1] M. Shastry and J. B. Udgaonkar, "The folding mechanism of barstar: evidence for multiple pathways and multiple intermediates," *J. Mol. Biol.*, vol. 247, no. 5, pp. 1013–1027, 1995.

[2] B. Schuler, E. A. Lipman, and W. A. Eaton, "Probing the free-energy surface for protein folding with single-molecule fluorescence spectroscopy," *Nature*, vol. 419, no. 6908, pp. 743–747, 2002.

[3] X. Michalet, S. Weiss, and M. Jäger, "Single-molecule fluorescence studies of protein folding and conformational dynamics," *Chem. Rev.*, vol. 106, no. 5, pp. 1785–1813, 2006.

[4] H. Frauenfelder, S. G. Sligar, and P. G. Wolynes, "The energy landscapes and motions of proteins," *Urbana*, vol. 51, no. 61801, p. 61801, 1991.

[5] S. D. Rader and D. A. Agard, "Conformational substates in enzyme mechanism: The 120 k structure of α-lytic protease at 1.5 å resolution," *Prot. Sci.*, vol. 6, no. 7, pp. 1375–1386, 1997.

[6] M. C. Deller and E. Y. Jones, "Cell surface receptors," *Curr. Opin. Struct. Biol.*, vol. 10, no. 2, pp. 213–219, 2000.

[7] Y. Sako, S. Minoghchi, and T. Yanagida, "Single-molecule imaging of egfr signalling on the surface of living cells," *Nat. Cell Biol.*, vol. 2, no. 3, pp. 168–172, 2000.

[8] X. Michalet, F. Pinaud, L. Bentolila, J. Tsay, S. Doose, J. Li, G. Sundaresan, A. Wu, S. Gambhir, and S. Weiss, "Quantum dots for live cells, in vivo imaging, and diagnostics," *Science*, vol. 307, no. 5709, pp. 538–544, 2005.

[9] Q. Sun, Y. A. Wang, L. S. Li, D. Wang, T. Zhu, J. Xu, C. Yang, and Y. Li, "Bright, multicoloured light-emitting diodes based on quantum dots," *Nat. Photon.*, vol. 1, no. 12, pp. 717–722, 2007.

[10] M. Kuno, D. Fromm, H. Hamann, A. Gallagher, and D. Nesbitt, "Nonexponential blinking kinetics of single cdse quantum dots: A universal power law behavior," *J. Chem. Phys.*, vol. 112, p. 3117, 2000.

[11] K. Shimizu, R. Neuhauser, C. Leatherdale, S. Empedocles, W. Woo, and M. Bawendi, "Blinking statistics in single semiconductor nanocrystal quantum dots," *Phys. Rev. B*, vol. 63, no. 20, p. 205316, 2001.

[12] P. A. Frantsuzov, S. Volkan-Kacso, and B. Janko, "Universality of the fluorescence intermittency in nanoscale systems: experiment and theory," *Nano Lett.*, vol. 13, no. 2, pp. 402–408, 2013.

[13] C. Galland, Y. Ghosh, A. Steinbrück, M. Sykora, J. A. Hollingsworth, V. I. Klimov, and H. Htoon, "Two types of luminescence blinking revealed by spectroelectrochemistry of single quantum dots," *Nature*, vol. 479, no. 7372, pp. 203–207, 2011.

[14] M. Pelton, D. G. Grier, and P. Guyot-Sionnest, "Characterizing quantum-dot blinking using noise power spectra," *Appl. Phys. Lett.*, vol. 85, no. 5, pp. 819–821, 2004.

[15] B. Mandelbrot, "Some noises with spectrum, a bridge between direct current and white noise," *Information Theory, IEEE Transactions on*, vol. 13, no. 2, pp. 289–298, 1967.

[16] M. S. Keshner, "1/f noise," *Proc. IEEE*, vol. 70, no. 3, pp. 212–218, 1982.

[17] S. Kogan, *Electronic noise and fluctuations in solids.* Cambridge Univ. Press, New York, 2008.

[18] M. Niemann, H. Kantz, and E. Barkai, "Fluctuations of 1/f noise and the low-frequency cutoff paradox," *Phys. Rev. Lett.*, vol. 110, no. 14, p. 140603, 2013.

[19] S. A. Diaz and M. Di Ventra, "Deconstructing 1/f noise and the universal crossover to non-1/f behavior," *arXiv preprint arXiv:1309.1907*, 2013.

[20] M. Caloyannides, "Microcycle spectral estimates of 1/f noise in semiconductors," *J. Appl. Phys.*, vol. 45, no. 1, pp. 307–316, 1974.

[21] B. B. Mandelbrot and J. R. Wallis, "Some long-run properties of geophysical records," *Water resources research*, vol. 5, no. 2, pp. 321–340, 1969.

[22] M. B. Weissman, "1/ f noise and other slow, nonexponential kinetics in condensed matter," *Rev. Mod. Phys.*, vol. 60, no. 2, pp. 537–571, 1988.

[23] P. Dutta and P. M. Horn, "Low-frequency fluctuations in solids: 1/f noise," *Rev. Mod. Phys.*, vol. 53, no. 3, 1981.

[24] Y. Lavi, M. A. Edidin, and L. A. Gheber, "Dynamic patches of membrane proteins," *Biophys. J.*, vol. 93, no. 6, pp. L35–L37, 2007.

[25] Y. Lavi, N. Gov, M. Edidin, Edidin, and L. A. Gheber, "Lifetime of major histocompatibility complex class-i membrane clusters is controlled by the actin cytoskeleton," *Biophys. J.*, vol. 102, no. 7, pp. 1543–1550, 2012.

[26] M. V. Gudheti, N. M. Curthoys, T. J. Gould, D. Kim, M. S. Gunewardene, K. A. Gabor, J. A. Gosse, C. H. Kim, J. Zimmerberg, and S. T. Hess, "Actin mediates the nanoscale membrane organization of the clustered membrane protein influenza hemagglutinin," *Biophys. J.*, vol. 104, no. 10, pp. 2182–2192, 2013.

[27] M. Sheetz, “Membrane skeletal dynamics: role in modulation of red cell deformability, mobility of transmembrane proteins, and shape.,” in *Seminars in Hematology*, vol. 20, pp. 175–188, 1983.

[28] M. J. Saxton and K. Jacobson, “Single-particle tracking: applications to membrane dynamics,” *Annu. Rev. Biophys. Biomol. Struct.*, vol. 26, no. 1, pp. 373–399, 1997.

[29] K. Ritchie, R. Iino, T. Fujiwara, K. Murase, and A. Kusumi, “The fence and picket structure of the plasma membrane of live cells as revealed by single molecule techniques (review),” *Mol. Memb. Biol.*, vol. 20, no. 1, pp. 13–18, 2003.

[30] A. Kusumi, C. Nakada, K. Ritchie, K. Murase, K. Suzuki, H. Murakoshi, R. S. Kasai, J. Kondo, and T. Fujiwara, “Paradigm shift of the plasma membrane concept from the two-dimensional continuum fluid to the partitioned fluid: high-speed single-molecule tracking of membrane molecules,” *Annu. Rev. Biophys. Biomol. Struct.*, vol. 34, pp. 351–378, 2005.

[31] G. Guigas and M. Weiss, “Sampling the cell with anomalous diffusionthe discovery of slowness,” *Biophys. J.*, vol. 94, no. 1, pp. 90–94, 2008.

[32] A. P. Minton, “How can biochemical reactions within cells differ from those in test tubes?,” *J. Cell Sci.*, vol. 119, no. 14, pp. 2863–2869, 2006.

[33] L. E. Sereshki, M. A. Lomholt, and R. Metzler, “A solution to the subdiffusion-efficiency paradox: Inactive states enhance reaction efficiency at subdiffusion conditions in living cells,” *Europhys. Lett.*, vol. 97, no. 2, p. 20008, 2012.

[34] J. Soboloff, M. Madesh, and D. L. Gill, “Sensing cellular stress through stim proteins,” *Nat. Chem. Biol.*, vol. 7, no. 8, pp. 488–492, 2011.

[35] S. Carrasco and T. Meyer, “Stim proteins and the endoplasmic reticulum-plasma membrane junctions,” *Annu. Rev. Biochem.*, vol. 80, pp. 973–1000, 2011.

[36] P. D. Fox, C. J. Haberkorn, A. V. Weigel, J. L. Higgins, E. J. Akin, M. J. Kennedy, D. Krapf, and M. M. Tamkun, “Plasma membrane domains enriched in cortical endoplasmic reticulum function as membrane protein trafficking hubs,” *Mol. Biol. Cell*, vol. 24, no. 17, pp. 2703–2713, 2013.

[37] P. D. Fox, C. J. Haberkorn, E. J. Akin, P. J. Seel, D. Krapf, and M. M. Tamkun, “Induction of stable er–plasma-membrane junctions by kv2.1 potassium channels,” *J. Cell Sci.*, vol. 128, no. 11, pp. 2096–2105, 2015.

[38] F. N. Hooge, “Discussion of recent experiments on 1/f noise,” *Physica*, vol. 60, p. 130, 1972.

[39] I. Eliazar and J. Klafter, “A unified and universal explanation for Lévy laws and 1/f noises,” *Proc. Natl. Acad. Sci. USA*, vol. 106, no. 30, pp. 12251–12254, 2009.

[40] B. Mandelbrot, “Some noises with spectrum, a bridge between direct current and white noise,” *IEEE Trans. Inform. Theory*, vol. 13, p. 289, 1967.

[41] A. Sornette and D. Sornette, “Self-organized criticality and earthquakes,” *Europhys. Lett.*, vol. 9, no. 3, p. 197, 1989.

[42] I. Csabai, “1/f noise in computer network traffic,” *J. Phys. A: Math. Gen.*, vol. 27, no. 12, p. L417, 1994.

[43] J. M. Halley, “Ecology, evolution and 1/f noise,” *Trends in Ecology & Evolution*, vol. 11, no. 1, pp. 33–37, 1996.

[44] D. L. Gilden, T. Thornton, and M. W. Mallon, “1/f noise in human cognition,” *Science*, vol. 267, no. 5205, pp. 1837–1839, 1995.

[45] M. S. Keshner, "1/f noise," *Proc. IEEE*, vol. 70, p. 212, 1982.

[46] S. Kogan, *Electronic noise and fluctuations in solids.* Cambridge Univ. Press, New York, 1996.

[47] J. B. Johnson, "The Schottky effect in low frequency circuits," *Phys. Rev.*, vol. 26, no. 1, p. 71, 1925.

[48] S. Sadegh, E. Barkai, and D. Krapf, "1/f noise for intermittent quantum dots exhibits non-stationarity and critical exponents," *New Journal of Physics*, vol. 16, no. 11, p. 113054, 2014.

[49] M. A. Caloyannides, "Microcycle spectral estimates of 1/f noise in semiconductors," *J. Appl. Phys.*, vol. 45, p. 307, 1974.

[50] S. M. Bezrukov and M. Winterhalter, "Examining noise sources at the single-molecule level: 1/f noise of an open maltoporin channel," *Phys. Rev. Lett.*, vol. 85, no. 1, p. 202, 2000.

[51] Z. Siwy and A. Fuliński, "Origin of 1/f noise in membrane channel currents," *Phys. Rev. Lett*, vol. 89, no. 158101, p. 1, 2002.

[52] D. Krapf, "Nonergodicity in nanoscale electrodes," *Phys. Chem. Chem. Phys.*, vol. 15, p. 459, 2013.

[53] A. R. Bizzarri and S. Cannistraro, "$1/f^\alpha$ noise in the dynamic force spectroscopy curves signals the occurrence of biorecognition," *Phys. Rev. Lett.*, vol. 110, p. 048104, 2013.

[54] A. A. Balandin, "Low-frequency 1/f noise in graphene devices," *Nat. Nanotechnol.*, vol. 8, no. 8, pp. 549–555, 2013.

[55] M. Kuno, D. P. Fromm, H. F. Hamann, A. Gallagher, and D. J. Nesbitt, "Nonexponential "blinking" kinetics of single CdSe quantum dots: A universal power law behavior," *J. Chem. Phys.*, vol. 112, p. 3117, 2000.

[56] K. T. Shimizu, R. G. Neuhauser, C. A. Leatherdale, S. A. Empedocles, W. K. Woo, and M. G. Bawendi, "Blinking statistics in single semiconductor nanocrystal quantum dots," *Phys. Rev. B*, vol. 63, p. 205316, 2001.

[57] P. A. Frantsuzov, S. Volkán-Kacsó, and B. Jankó, "Universality of the fluorescence intermittency in nanoscale systems: experiment and theory," *Nano Lett.*, vol. 13, p. 402, 2013.

[58] X. Brokmann, J.-P. Hermier, G. Messin, P. Desbiolles, J. P. Bouchaud, and M. Dahan, "Statistical aging and nonergodicity in the fluorescence of single nanocrystals," *Phys. Rev. Lett.*, vol. 90, p. 120601, 2003.

[59] P. Frantsuzov, M. Kuno, B. Jankó, and R. A. Marcus, "Universal emission intermittency in quantum dots, nanorods and nanowires," *Nat. Phys.*, vol. 4, p. 519, 2008.

[60] F. D. Stefani, J. P. Hoogenboom, and E. Barkai, "Beyond quantum jumps: blinking nanoscale light emitters," *Phys. Today*, vol. 2, p. 34, 2009.

[61] M. Pelton, D. G. Grier, and P. Guyot-Sionnest, "Characterizing quantum-dot blinking using noise power spectra," *Appl. Phys. Lett.*, vol. 85, p. 819, 2004.

[62] C. H. Crouch, O. Sauter, X. Wu, R. Purcell, C. Querner, M. Drndic, and M. Pelton, "Facts and artifacts in the blinking statistics of semiconductor nanocrystals," *Nano Lett.*, vol. 10, p. 1692, 2010.

[63] M. Nirmal, B. Dabbousi, M. Bawendi, J. Macklin, J. Trautman, T. Harris, and L. Brus, "Fluorescence intermittency in single cadmium selenide nanocrystals," *Nature*, vol. 383, no. 6603, pp. 802–804, 1996.

[64] P. Manneville, "Intermittency, self-similarity and 1/f spectrum in dissipative dynamical systems," *J. Phys. (Paris)*, vol. 41, p. 1235, 1980.

[65] L. Silvestri, L. Fronzoni, P. Grigolini, and P. Allegrini, "Event-driven power-law relaxation in weak turbulence," *Phys. Rev. Lett.*, vol. 102, p. 014502, 2009.

[66] J. P. Hoogenboom, J. Hernando, E. M. van Dijk, N. F. van Hulst, and M. F. García-Parajo, "Power-law blinking in the fluorescence of single organic molecules," *Chem. Phys. Chem.*, vol. 8, no. 6, pp. 823–833, 2007.

[67] M. Niemann, I. G. Szendro, and H. Kantz, "$1/f^{\beta}$ noise in a model for weak ergodicity breaking," *Chem. Phys.*, vol. 375, no. 2, pp. 370–377, 2010.

[68] G. Margolin and E. Barkai, "Nonergodicity of a time series obeying Lévy statistics," *J. Stat. Phys.*, vol. 122, p. 137, 2006.

[69] M. Niemann, H. Kantz, and E. Barkai, "Fluctuations of 1/f noise and the low-frequency cutoff paradox," *Phys. Rev. Lett.*, vol. 110, p. 140603, 2013.

[70] A. Godec and R. Metzler, "Linear response, fluctuation-dissipation, and finite-system-size effects in superdiffusion," *Phys. Rev. E*, vol. 88, no. 1, p. 012116, 2013.

[71] M. Pelton, G. Smith, N. F. Scherer, and R. A. Marcus, "Evidence for a diffusion-controlled mechanism for fluorescence blinking of colloidal quantum dots," *Proc. Natl. Acad. Sci. USA*, vol. 104, pp. 14249–14254, 2007.

[72] C. Godrèche and J. M. Luck, "Statistics of the occupation time of renewal processes," *J. Stat. Phys.*, vol. 104, no. 3-4, pp. 489–524, 2001.

[73] J. Klafter and I. M. Sokolov, *First Steps in Random Walks.* Oxford Univ. Press, New York, 2011.

[74] J.-H. Jeon, E. Barkai, and R. Metzler, “Noisy continuous time random walks,” *J. Chem. Phys.*, vol. 139, no. 12, p. 121916, 2013.

[75] G. Messin, J. Hermier, E. Giacobino, P. Desbiolles, and M. Dahan, “Bunching and antibunching in the fluorescence of semiconductor nanocrystals,” *Opt. Lett.*, vol. 26, no. 23, pp. 1891–1893, 2001.

[76] K. Zhang, H. Chang, A. Fu, A. P. Alivisatos, and H. Yang, “Continuous distribution of emission states from single CdSe/ZnS quantum dots,” *Nano Lett.*, vol. 6, no. 4, pp. 843–847, 2006.

[77] P. Spinicelli, S. Buil, X. Quelin, B. Mahler, B. Dubertret, and J.-P. Hermier, “Bright and grey states in CdSe-CdS nanocrystals exhibiting strongly reduced blinking,” *Phys. Rev. Lett.*, vol. 102, no. 13, p. 136801, 2009.

[78] C. Galland, Y. Ghosh, A. Steinbrck, M. Sykora, J. A. Hollingsworth, V. I. Klimov, and H. Htoon, “Two types of luminescence blinking revealed by spectroelectrochemistry of single quantum dots,” *Nature*, vol. 479, p. 203, 2011.

[79] N. Amecke and F. Cichos, “Intermediate intensity levels during the emission intermittency of single cdse/zns quantum dots,” *J. Luminesc.*, vol. 131, no. 3, pp. 375–378, 2011.

[80] G. Zumofen and J. Klafter, “Power spectra and random walks in intermittent chaotic systems,” *Physica D*, vol. 69, p. 436, 1993.

[81] H. Scher, G. Margolin, R. Metzler, J. Klafter, and B. Berkowitz, “The dynamical foundation of fractal stream chemistry: The origin of extremely long retention times,” *Geophysical Research Letters*, vol. 29, no. 5, pp. 5–1, 2002.

[82] J. P. Bouchaud, “Weak ergodicity breaking and aging in disordered systems,” *J. Phys. I (France)*, vol. 2, p. 1705, 1992.

[83] S. Burov, R. Metzler, and E. Barkai, “Aging and nonergodicity beyond the Khinchin theorem,” *Proc. Natl. Acad. Sci. USA*, vol. 107, no. 30, pp. 13228–13233, 2010.

[84] J.-P. Bouchaud and A. Georges, “Anomalous diffusion in disordered media: statistical mechanisms, models and physical applications,” *Phys. Rep.*, vol. 195, no. 4, pp. 127–293, 1990.

[85] R. Metzler and J. Klafter, “The restaurant at the end of the random walk: recent developments in the description of anomalous transport by fractional dynamics,” *J. Phys. A: Mathematical and General*, vol. 37, no. 31, p. R161, 2004.

[86] A. V. Weigel, B. Simon, M. M. Tamkun, and D. Krapf, “Ergodic and nonergodic processes coexist in the plasma membrane as observed by single-molecule tracking,” *Proc. Natl. Acad. Sci. USA*, vol. 108, no. 16, pp. 6438–6443, 2011.

[87] S. A. Tabei, S. Burov, H. Y. Kim, A. Kuznetsov, T. Huynh, J. Jureller, L. H. Philipson, A. R. Dinner, and N. F. Scherer, “Intracellular transport of insulin granules is a subordinated random walk,” *Proc. Natl. Acad. Sci. USA*, vol. 110, no. 13, pp. 4911–4916, 2013.

[88] S. Burov, S. A. Tabei, T. Huynh, M. P. Murrell, L. H. Philipson, S. A. Rice, M. L. Gardel, N. F. Scherer, and A. R. Dinner, “Distribution of directional change as a signature of complex dynamics,” *Proc. Natl. Acad. Sci. USA*, vol. 110, no. 49, pp. 19689–19694, 2013.

[89] X. Brokmann, J.-P. Hermier, G. Messin, P. Desbiolles, J.-P. Bouchaud, and M. Dahan, “Statistical aging and nonergodicity in the fluorescence of single nanocrystals,” *Phys. Rev. Lett.*, vol. 90, no. 12, p. 120601, 2003.

[90] Y. He, S. Burov, R. Metzler, and E. Barkai, “Random time-scale invariant diffusion and transport coefficients,” *Phys. Rev. Lett.*, vol. 101, no. 5, p. 058101, 2008.

[91] K. Murase, T. Fujiwara, Y. Umemura, K. Suzuki, R. Iino, H. Yamashita, M. Saito, H. Murakoshi, K. Ritchie, and A. Kusumi, “Ultrafine membrane compartments for molecular diffusion as revealed by single molecule techniques,” *Biophys. J.*, vol. 86, no. 6, pp. 4075–4093, 2004.

[92] S. Manley, J. M. Gillette, G. H. Patterson, H. Shroff, H. F. Hess, E. Betzig, and J. Lippincott-Schwartz, “High-density mapping of single-molecule trajectories with photoactivated localization microscopy,” *Nat. Methods*, vol. 5, no. 2, pp. 155–157, 2008.

[93] C. Di Rienzo, E. Gratton, F. Beltram, and F. Cardarelli, “Fast spatiotemporal correlation spectroscopy to determine protein lateral diffusion laws in live cell membranes,” *Proc. Natl. Acad. Sci. USA*, vol. 110, no. 30, pp. 12307–12312, 2013.

[94] P.-F. Lenne, L. Wawrezinieck, F. Conchonaud, O. Wurtz, A. Boned, X.-J. Guo, H. Rigneault, H.-T. He, and D. Marguet, “Dynamic molecular confinement in the

plasma membrane by microdomains and the cytoskeleton meshwork," *EMBO J.*, vol. 25, no. 14, pp. 3245–3256, 2006.

[95] V. Ruprecht, S. Wieser, D. Marguet, and G. J. Schütz, "Spot variation fluorescence correlation spectroscopy allows for superresolution chronoscopy of confinement times in membranes," *Biophys. J.*, vol. 100, no. 11, pp. 2839–2845, 2011.

[96] A. Honigmann, V. Mueller, H. Ta, A. Schoenle, E. Sezgin, S. W. Hell, and C. Eggeling, "Scanning sted-fcs reveals spatiotemporal heterogeneity of lipid interaction in the plasma membrane of living cells," *Nat. Comm.*, vol. 5, 2014.

[97] E. Barkai, Y. Garini, and R. Metzler, "Strange kinetics of single molecules in living cells," *Physics Today*, vol. 65, no. 8, pp. 29–35, 2012.

[98] F. Höfling and T. Franosch, "Anomalous transport in the crowded world of biological cells," *Rep. Prog. Phys.*, vol. 76, no. 4, p. 046602, 2013.

[99] R. Metzler, J.-H. Jeon, A. G. Cherstvy, and E. Barkai, "Anomalous diffusion models and their properties: non-stationarity, non-ergodicity, and ageing at the centenary of single particle tracking," *Phys. Chem. Chem. Phys.*, vol. 16, no. 44, pp. 24128–24164, 2014.

[100] D. Krapf, "Mechanisms underlying anomalous diffusion in the plasma membrane," *Curr. Top. Membr.*, vol. 75, pp. 167–207, 2015.

[101] S. Sadegh, J. L. Higgins, P. C. Mannion, M. M. Tamkun, and D. Krapf, "Plasma membrane is compartmentalized by a self-similar cortical actin meshwork," *Phys. Rev. X*, vol. 7, no. 1, p. 011031, 2017.

[102] J. A. Dix and A. Verkman, "Crowding effects on diffusion in solutions and cells," *Annu. Rev. Biophys.*, vol. 37, pp. 247–263, 2008.

[103] T. V. Ratto and M. L. Longo, "Anomalous subdiffusion in heterogeneous lipid bilayers," *Langmuir*, vol. 19, no. 5, pp. 1788–1793, 2003.

[104] C. Manzo, J. A. Torreno-Pina, P. Massignan, G. J. Lapeyre Jr, M. Lewenstein, and M. F. G. Parajo, "Weak ergodicity breaking of receptor motion in living cells stemming from random diffusivity," *Phys. Rev. X*, vol. 5, no. 1, p. 011021, 2015.

[105] T. Fujiwara, K. Ritchie, H. Murakoshi, K. Jacobson, and A. Kusumi, "Phospholipids undergo hop diffusion in compartmentalized cell membrane," *J. Cell Biol.*, vol. 157, no. 6, pp. 1071–1082, 2002.

[106] A. V. Weigel, M. M. Tamkun, and D. Krapf, "Quantifying the dynamic interactions between a clathrin-coated pit and cargo molecules," *Proc. Natl. Acad. Sci. USA*, vol. 110, no. 48, pp. E4591–E4600, 2013.

[107] D. W. Tank, E.-S. Wu, and W. W. Webb, "Enhanced molecular diffusibility in muscle membrane blebs: release of lateral constraints.," *J. Cell Biol.*, vol. 92, no. 1, pp. 207–212, 1982.

[108] D. M. Andrade, M. P. Clausen, J. Keller, V. Mueller, C. Wu, J. E. Bear, S. W. Hell, B. C. Lagerholm, and C. Eggeling, "Cortical actin networks induce spatio-temporal confinement of phospholipids in the plasma membrane–a minimally invasive investigation by sted-fcs," *Sci. Rep.*, vol. 5, 2015.

[109] K. K. Deal, S. K. England, and M. M. Tamkun, "Molecular physiology of cardiac potassium channels," *Physiol. Rev.*, vol. 76, no. 1, pp. 49–67, 1996.

[110] B. B. Mandelbrot and J. W. Van Ness, "Fractional brownian motions, fractional noises and applications," *SIAM REV.*, vol. 10, no. 4, pp. 422–437, 1968.

[111] W. Deng and E. Barkai, “Ergodic properties of fractional brownian-langevin motion,” *Phys. Rev. E*, vol. 79, no. 1, p. 011112, 2009.

[112] M. J. Saxton, “Anomalous diffusion due to obstacles: a monte carlo study.,” *Biophys. J.*, vol. 66, no. 2 Pt 1, pp. 394–401, 1994.

[113] D. Ben-Avraham and S. Havlin, *Diffusion and reactions in fractals and disordered systems.* Cambridge University Press, Cambridge, 2000.

[114] A. V. Weigel, S. Ragi, M. L. Reid, E. K. Chong, M. M. Tamkun, and D. Krapf, “Obstructed diffusion propagator analysis for single-particle tracking,” *Phys. Rev. E*, vol. 85, no. 4, p. 041924, 2012.

[115] J. Szymanski and M. Weiss, “Elucidating the origin of anomalous diffusion in crowded fluids,” *Phys. Rev. Lett.*, vol. 103, no. 3, p. 038102, 2009.

[116] D. Ernst, M. Hellmann, J. Köhler, and M. Weiss, “Fractional brownian motion in crowded fluids,” *Soft Matter*, vol. 8, no. 18, pp. 4886–4889, 2012.

[117] G. Guigas, C. Kalla, and M. Weiss, “The degree of macromolecular crowding in the cytoplasm and nucleoplasm of mammalian cells is conserved,” *FEBS Lett.*, vol. 581, no. 26, pp. 5094–5098, 2007.

[118] M. Weiss, “Single-particle tracking data reveal anticorrelated fractional brownian motion in crowded fluids,” *Phys. Rev. E*, vol. 88, no. 1, p. 010101, 2013.

[119] H. Scher and E. W. Montroll, “Anomalous transit-time dispersion in amorphous solids,” *Phys. Rev. B*, vol. 12, no. 6, p. 2455, 1975.

[120] M. Magdziarz, A. Weron, K. Burnecki, and J. Klafter, “Fractional brownian motion versus the continuous-time random walk: A simple test for subdiffusive dynamics,” *Phys. Rev. Lett.*, vol. 103, no. 18, p. 180602, 2009.

[121] G. Rangarajan and M. Ding, “First passage time distribution for anomalous diffusion,” *Phys. Lett. A*, vol. 273, no. 5, pp. 322–330, 2000.

[122] V. Tejedor, O. Bénichou, R. Voituriez, R. Jungmann, F. Simmel, C. Selhuber-Unkel, L. B. Oddershede, and R. Metzler, “Quantitative analysis of single particle trajectories: mean maximal excursion method,” *Biophys J.*, vol. 98, no. 7, pp. 1364–1372, 2010.

[123] M. Weiss, M. Elsner, F. Kartberg, and T. Nilsson, “Anomalous subdiffusion is a measure for cytoplasmic crowding in living cells,” *Biophys. J.*, vol. 87, no. 5, pp. 3518–3524, 2004.

[124] Y. Meroz, I. M. Sokolov, and J. Klafter, “Test for determining a subdiffusive model in ergodic systems from single trajectories,” *Phys. Rev. Lett.*, vol. 110, no. 9, p. 090601, 2013.

[125] A. M. VanDongen, G. C. Frech, J. A. Drewe, R. H. Joho, and A. M. Brown, “Alteration and restoration of k+ channel function by deletions at the n-and c-termini,” *Neuron*, vol. 5, no. 4, pp. 433–443, 1990.

[126] A. Tsuji and S. Ohnishi, “Restriction of the lateral motion of band 3 in the erythrocyte membrane by the cytoskeletal network: dependence on spectrin association state,” *Biochemistry*, vol. 25, no. 20, pp. 6133–6139, 1986.

[127] M. Edidin, M. C. Zuniga, and M. P. Sheetz, “Truncation mutants define and locate cytoplasmic barriers to lateral mobility of membrane glycoproteins.,” *Proc. Natl. Acad. Sci. U.S.A.*, vol. 91, no. 8, pp. 3378–3382, 1994.

[128] N. L. Andrews, K. A. Lidke, J. R. Pfeiffer, A. R. Burns, B. S. Wilson, J. M. Oliver, and D. S. Lidke, “Actin restricts fcϵ ri diffusion and facilitates antigen-induced receptor immobilization,” *Nat. Cell Biol.*, vol. 10, no. 8, pp. 955–963, 2008.

[129] J. Wiedenmann, S. Ivanchenko, F. Oswald, F. Schmitt, C. Röcker, A. Salih, K.-D. Spindler, and G. U. Nienhaus, “Eosfp, a fluorescent marker protein with uv-inducible green-to-red fluorescence conversion,” *Proc. Natl. Acad. Sci. USA*, vol. 101, no. 45, pp. 15905–15910, 2004.

[130] I. Izeddin, C. G. Specht, M. Lelek, X. Darzacq, A. Triller, C. Zimmer, and M. Dahan, “Super-resolution dynamic imaging of dendritic spines using a low-affinity photoconvertible actin probe,” *PLoS ONE*, vol. 6, no. 1, p. e15611, 2011.

[131] J. Riedl, A. H. Crevenna, K. Kessenbrock, J. H. Yu, D. Neukirchen, M. Bista, F. Bradke, D. Jenne, T. A. Holak, Z. Werb, *et al.*, “Lifeact: a versatile marker to visualize f-actin,” *Nat. Methods*, vol. 5, no. 7, pp. 605–607, 2008.

[132] B. Treanor, D. Depoil, A. Gonzalez-Granja, P. Barral, M. Weber, O. Dushek, A. Bruckbauer, and F. D. Batista, “The membrane skeleton controls diffusion dynamics and signaling through the b cell receptor,” *Immunity*, vol. 32, no. 2, pp. 187–199, 2010.

[133] J. A. Torreno-Pina, C. Manzo, M. Salio, M. C. Aichinger, A. Oddone, M. Lakadamyali, D. Shepherd, G. S. Besra, V. Cerundolo, and M. F. Garcia-Parajo, “The actin cytoskeleton modulates the activation of inkt cells by segregating cd1d nanoclusters on antigen-presenting cells,” *Proc. Natl. Acad. Sci*, vol. 113, no. 6, pp. E772–E781, 2016.

[134] M. J. Rust, M. Bates, and X. Zhuang, “Sub-diffraction-limit imaging by stochastic optical reconstruction microscopy (storm),” *Nat. Methods*, vol. 3, no. 10, pp. 793–796, 2006.

[135] G. T. Dempsey, J. C. Vaughan, K. H. Chen, M. Bates, and X. Zhuang, “Evaluation of fluorophores for optimal performance in localization-based super-resolution imaging,” *Nat. Methods*, vol. 8, no. 12, pp. 1027–1036, 2011.

[136] K. Xu, H. P. Babcock, and X. Zhuang, “Dual-objective storm reveals three-dimensional filament organization in the actin cytoskeleton,” *Nat. Methods*, vol. 9, no. 2, pp. 185–188, 2012.

[137] F. Meyer and S. Beucher, “Morphological segmentation,” *J. Vis. Commun. Image Represent.*, vol. 1, no. 1, pp. 21–46, 1990.

[138] C. Klüppelberg, “Subexponential distributions and integrated tails,” *J. Appl. Probab.*, pp. 132–141, 1988.

[139] A. N. Kolmogorov, “On the logarithmically normal law of distribution of the size of particles under pulverisation,” *Dokl. Akad. Nauk SSSR*, vol. 31, pp. 99–101, 1941.

[140] B. Epstein, “The mathematical description of certain breakage mechanisms leading to the logarithmico-normal distribution,” *J. Franklin Inst.*, vol. 244, no. 6, pp. 471–477, 1947.

[141] B. B. Mandelbrot, *The fractal geometry of nature*, vol. 173. Macmillan, London, 1983.

[142] S. Lovejoy, “Area-perimeter relation for rain and cloud areas,” *Science*, vol. 216, no. 4542, pp. 185–187, 1982.

[143] A. Imre and J. Bogaert, “The fractal dimension as a measure of the quality of habitats,” *Acta Biotheor.*, vol. 52, no. 1, pp. 41–56, 2004.

[144] P. S. Addison, *Fractals and chaos: an illustrated course.* CRC Press, 1997.

[145] W. Newman, D. Turcotte, and A. Gabrielov, “Fractal trees with side branching,” *Fractals*, vol. 5, no. 04, pp. 603–614, 1997.

[146] R. E. Horton, “Erosional development of streams and their drainage basins; hydrophysical approach to quantitative morphology,” *Geol. Soc. Am. Bull.*, vol. 56, no. 3, pp. 275–370, 1945.

[147] D. Pantaloni, R. Boujemaa, D. Didry, P. Gounon, and M.-F. Carlier, “The arp2/3 complex branches filament barbed ends: functional antagonism with capping proteins,” *Nat. Cell Biol.*, vol. 2, no. 7, pp. 385–391, 2000.

[148] K. Gowrishankar, S. Ghosh, S. Saha, C. Rumamol, S. Mayor, and M. Rao, “Active remodeling of cortical actin regulates spatiotemporal organization of cell surface molecules,” *Cell*, vol. 149, no. 6, pp. 1353–1367, 2012.

[149] K. M. O’Connell, A. S. Rolig, J. D. Whitesell, and M. M. Tamkun, “Kv2. 1 potassium channels are retained within dynamic cell surface microdomains that are defined by a perimeter fence,” *J. Neurosci.*, vol. 26, no. 38, pp. 9609–9618, 2006.

[150] K. Jaqaman, D. Loerke, M. Mettlen, H. Kuwata, S. Grinstein, S. L. Schmid, and G. Danuser, “Robust single-particle tracking in live-cell time-lapse sequences,” *Nat. Methods*, vol. 5, no. 8, pp. 695–702, 2008.

[151] C. S. Smith, N. Joseph, B. Rieger, and K. A. Lidke, “Fast, single-molecule localization that achieves theoretically minimum uncertainty,” *Nat. Methods*, vol. 7, no. 5, pp. 373–375, 2010.

[152] J. C. Russ, *The image processing handbook*. CRC press, Boca Raton, 2015.

[153] J.-V. Small, K. Rottner, P. Hahne, K. I. Anderson, *et al.*, “Visualising the actin cytoskeleton,” *Microsc. Res. Tech.*, vol. 47, no. 1, pp. 3–17, 1999.

[154] M. Ovesnỳ, P. Křížek, J. Borkovec, Z. Švindrych, and G. M. Hagen, “Thunderstorm: a comprehensive imagej plug-in for palm and storm data analysis and super-resolution imaging,” *Bioinformatics*, vol. 30, no. 16, pp. 2389–2390, 2014.

[155] C. Ortiz De Solórzano, E. Garcia Rodriguez, A. Jones, D. Pinkel, J. W. Gray, D. Sudar, and S. J. Lockett, "Segmentation of confocal microscope images of cell nuclei in thick tissue sections," *J. Microsc.*, vol. 193, no. 3, pp. 212–226, 1999.

[156] J. Cheng and J. C. Rajapakse, "Segmentation of clustered nuclei with shape markers and marking function," *IEEE Trans. Biomed. Engr.*, vol. 56, no. 3, pp. 741–748, 2009.

[157] A. Kusumi, Y. Sako, and M. Yamamoto, "Confined lateral diffusion of membrane receptors as studied by single particle tracking (nanovid microscopy). effects of calcium-induced differentiation in cultured epithelial cells.," *Biophysical journal*, vol. 65, no. 5, p. 2021, 1993.

[158] Y. Sako and A. Kusumi, "Compartmentalized structure of the plasma membrane for receptor movements as revealed by a nanometer-level motion analysis.," *J. Cell Biol.*, vol. 125, no. 6, pp. 1251–1264, 1994.

[159] M. Edidin, S. C. Kuo, and M. P. Sheetz, "Lateral movements of membrane glycoproteins restricted by dynamic cytoplasmic barriers," *Science*, vol. 254, no. 5036, pp. 1379–1383, 1991.

[160] Y. Sako and A. Kusumi, "Barriers for lateral diffusion of transferrin receptor in the plasma membrane as characterized by receptor dragging by laser tweezers: fence versus tether.," *J. Cell Biol.*, vol. 129, no. 6, pp. 1559–1574, 1995.

[161] N. Morone, T. Fujiwara, K. Murase, R. S. Kasai, H. Ike, S. Yuasa, J. Usukura, and A. Kusumi, "Three-dimensional reconstruction of the membrane skeleton at the plasma membrane interface by electron tomography," *J. Cell Biol.*, vol. 174, no. 6, pp. 851–862, 2006.

[162] H. S. Carslaw and J. C. Jaeger, *Conduction of heat in solids*. Oxford: Clarendon Press, 1959, 2nd ed., 1959.

[163] M. J. Saxton, “Lateral diffusion in an archipelago. single-particle diffusion,” *Biophys. J.*, vol. 64, no. 6, pp. 1766–1780, 1993.

[164] T. Bickel, “A note on confined diffusion,” *Physica A*, vol. 377, no. 1, pp. 24–32, 2007.

[165] M. J. Saxton, “Single-particle tracking: effects of corrals,” *Biophys. J.*, vol. 69, no. 2, pp. 389–398, 1995.

[166] J. G. Powles, M. Mallett, G. Rickayzen, and W. Evans, “Exact analytic solutions for diffusion impeded by an infinite array of partially permeable barriers,” vol. 436, no. 1897, pp. 391–403, 1992.

[167] S. Wieser, M. Moertelmaier, E. Fuertbauer, H. Stockinger, and G. J. Schütz, “(un) confined diffusion of cd59 in the plasma membrane determined by high-resolution single molecule microscopy,” *Biophys. J.*, vol. 92, no. 10, pp. 3719–3728, 2007.

[168] T. Auth and N. S. Gov, “Diffusion in a fluid membrane with a flexible cortical cytoskeleton,” *Biophys. J.*, vol. 96, no. 3, pp. 818–830, 2009.

[169] G. J. Lapeyre Jr, “Anomalous diffusion from brownian motion with random confinement,” *arXiv preprint*, vol. 1504.07158, 2015.

[170] P. S. Riseborough and P. Hanggi, “Diffusion on surfaces of finite size: Mössbauer effect as a probe,” *Surf. Sci.*, vol. 122, no. 3, pp. 459–473, 1982.

[171] A. R. English, N. Zurek, and G. K. Voeltz, “Peripheral er structure and function,” *Curr. Opin. Cell Biol.*, vol. 21, no. 4, pp. 596–602, 2009.

[172] Y. Shibata, J. Hu, M. M. Kozlov, and T. A. Rapoport, “Mechanisms shaping the membranes of cellular organelles,” *Annu. Rev. Cell Dev. Biol.*, vol. 25, pp. 329–354, 2009.

[173] D. Poteryaev, J. M. Squirrell, J. M. Campbell, J. G. White, and A. Spang, “Involvement of the actin cytoskeleton and homotypic membrane fusion in er dynamics in caenorhabditis elegans,” *Mol. Biol. Cell.*, vol. 16, no. 5, pp. 2139–2153, 2005.

[174] Y. Wang, M. P. Mattson, and K. Furukawa, “Endoplasmic reticulum calcium release is modulated by actin polymerization,” *J. Neurochem.*, vol. 82, no. 4, pp. 945–952, 2002.

[175] W. Wagner, S. D. Brenowitz, and J. A. Hammer III, “Myosin-va transports the endoplasmic reticulum into the dendritic spines of purkinje neurons,” *Nat. Cell Biol.*, vol. 13, no. 1, pp. 40–48, 2011.

[176] A. V. Weigel, P. D. Fox, E. J. Akin, K. H. Ecklund, M. M. Tamkun, and D. Krapf, “Size of cell-surface kv2. 1 domains is governed by growth fluctuations,” *Biophys. J.*, vol. 103, no. 8, pp. 1727–1734, 2012.

[177] H. Takeshima, S. Komazaki, M. Nishi, M. Iino, and K. Kangawa, “Junctophilins: a novel family of junctional membrane complex proteins,” *Mol. Cell.*, vol. 6, no. 1, pp. 11–22, 2000.

[178] M. Joensuu and E. Jokitalo, “Er sheet–tubule balance is regulated by an array of actin filaments and microtubules,” *Exp. Cell. Res.*, vol. 2, no. 337, pp. 170–178, 2015.

[179] E. S. Chhabra, V. Ramabhadran, S. A. Gerber, and H. N. Higgs, “Inf2 is an endoplasmic reticulum-associated formin protein,” *J. Cell Sci.*, vol. 122, no. 9, pp. 1430–1440, 2009.

[180] D. D. Shaye and I. Greenwald, "The disease-associated formin inf2/exc-6 organizes lumen and cell outgrowth during tubulogenesis by regulating f-actin and microtubule cytoskeletons," *Dev. cell*, vol. 32, no. 6, pp. 743–755, 2015.

[181] M. Joensuu, I. Belevich, O. Rämö, I. Nevzorov, H. Vihinen, M. Puhka, T. M. Witkos, M. Lowe, M. K. Vartiainen, and E. Jokitalo, "Er sheet persistence is coupled to myosin 1c–regulated dynamic actin filament arrays," *Mol. Biol. Cell.*, vol. 25, no. 7, pp. 1111–1126, 2014.

[182] J. Limouze, A. F. Straight, T. Mitchison, and J. R. Sellers, "Specificity of blebbistatin, an inhibitor of myosin ii," *J. Muscle Res. Cell Motil*, vol. 25, no. 4-5, pp. 337–341, 2004.

[183] M. I. Kotlikoff and K. E. Kamm, "Molecular mechanisms of beta-adrenergic relaxation of airway smooth muscle," *Annu. Rev. Physiol.*, vol. 58, no. 1, pp. 115–141, 1996.

[184] S. C. Harrison, "Cd4: Structure and interactions of an immunoglobulin superfamily adhesion molecule," *Acc. Chem. Res.*, vol. 26, pp. 449–449, 1993.

APPENDIX A

PROTOCOLS

This appendix provides protocols used for the experiments presented in this thesis, including setup alignment and sample preparation. Protocols A.1, A.2, A.3 and A.4 were adopted from Aubrey Weigel's thesis. Protocols A.5 and A.6 were written in part by Xinran Xu.

A.1. TIRF microscope alignment

Most of experiments presented in this thesis were performed in our custom-built TIRF setup. The setup needs to be properly aligned before each experiment in order to obtain the best quality images of the sample.

(1) Turn on lasers
(2) Check beam alignment before the last telescope. Make sure it is centered on each mirror, lens, scope, and is not being clipped. Do this for each laser being implemented
(3) All lasers need to be co-aligned at the last telescope
(4) Choose one laser in order to align the last two stirring mirrors and the focusing lens so that the laser is enters the objective centered and perpendicular
(5) Remove focusing lens from path
(6) Untighten main adjustment mirrors (S1 and S2)
(7) Place an iris on last stand of scope before S1. Close the iris to reduce beam size to allow for easier beam alignment

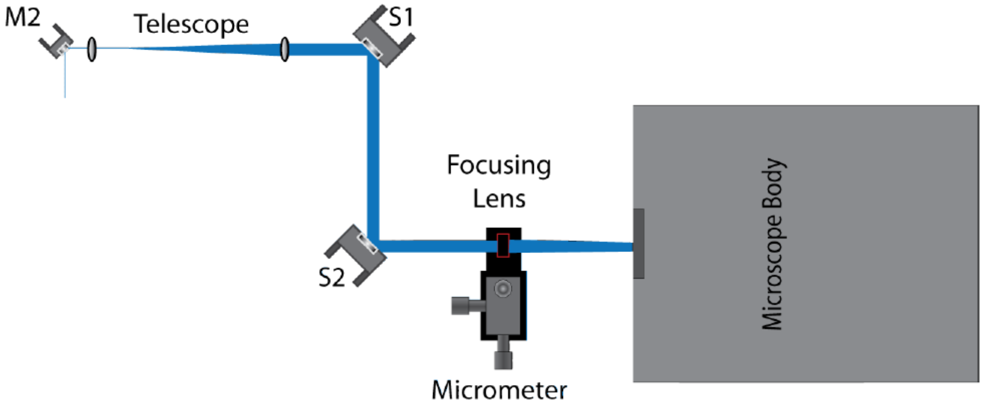

FIGURE A.1. General schematic of TIRF microscope. Mirrors S1 and S2 steer the beam into the focusing lens and then into the microscope. The focusing lens is on a micrometer for fine tune adjusting.

(8) Attach alignment tube to threads by which the objective attaches

(9) Close bottom iris of the alignment tube, adjust S1 such that the highest beam brightness on ceiling is achieved.

(10) Open bottom iris and close the top iris of the alignment tube. Adjust S2 such that the highest beam brightness is achieved.

(11) Continue alternating the adjustment between tube irises and corresponding mirrors until an optimal brightness is achieved with both iris closed.

(12) Remove alignment tube, center the cross-hair on the ceiling to aligned beam as a marker for later steps. Do not touch the steering mirrors until after the focusing lens is in place.

(13) Replace the focusing lens back in its positions.

(14) Make sure that the reflection of the beam off the focusing lens aligns to the original beam on mirror S2

(15) Use an aperture on the focusing lens and make sure the beam passes through the center using only the micrometer (do not use the steering mirrors)

(16) Mount the objective. If using the objective heater you can put this on the objective now as well.

(17) Re-center the laser on the ceiling using S2

(18) Adjust mirror S1 to center the beam on the lens

(19) Repeat steps 17 and 18 until the beam is going through the center of the focusing lens and aligned to the cross-hair on the ceiling

(20) Tighten the screws on the mirror adjustment knobs to hold mirror placement. Be careful not shift the beam or mirror position while doing this

(21) Remove irises

(22) Check filter box to ensure the proper dichroic and filters are in place for the experiment

A.2. Splitting cells

The experiments presented in chapter 3, 4, and 5 of thesis were performed in HEK293 cells (American Type Culture Collection). We only use cellls between passage 42 and 50 in our experiments. The cells confluence level need to be checked everyday. Once the cells are $\sim 80\%$ confluent we split the cells:

(1) Label 4 dishes with
    (a) Your name/initials
    (b) Date
    (c) Cell type
    (d) Passage number

(2) UV new sterile culture dishes that cells will be split into.

(3) Add10 mL DMSO + 10% FBS (with phenol red) with 10x antibiotic media into each dish

(4) Place dishes in incubator until ready to start step 7

(5) Aspirate media from dish of confluent cells

(6) Pipette 4mL of Trypsin EDTA into dish

(7) Once cells have lifted from bottom of dish split into new sterile cell culture dishes (1 mL in each dish)

A.3. Cell transfection

Transfection means introducing foreign DNA into an eukaryotic cell. There are different methods to do transfection including chemical-based transfection and non-chemical methods. The transfection method that we use is electroporation which is a non-chemical methods. In the electroporation method a transient increase in the permeability of cell membrane is achieved by exposing the cells to short pulses of an intense electric field. Here is a step by step protocol:

(1) Put tansfection media (DMEM + 10% FBS, without phenol red, with 10x antibiotic) and Trypsin in 37°C water bath 30 min before starting the transfection

(2) UV the 35 mm petri dishes

(3) Add 1 mL Matrigel to each dish and incubate them in the incubator for 30 minutes

(4) Remove Matrigel coated dishes from the incubator. Aspirate Matrigel from dishes. Replace with 1 mL of DMEM + 10% FBS (no phenol red, with antibiotic)

(5) Prepare the plasmid solution (200 μL Optimem and plasmids) and put the solution in water bath

(6) Aspirate media from dish of confluent cells

(7) Pipette 4mL of Trypsin EDTA into dish

(8) Once cells have lifted from bottom of dish add 10 mL of transfection media to the dish

(9) Pipette up and down once or twice to wash off any remaining cells stuck to the dish

(10) Place 14 mL mixture of cells, Trypsin and media into a 15 mL conical

(11) Centrifuge at 1.5 rpm for 3 min

(12) Bring Optimem-plasmid solution prepared in step 5 into the biosafety cabinet

(13) Aspirate media/Trypsin from 15mL conical tube with cell pellet, take care not to disturb the pellet of cells

(14) Re-suspend the cells with the Optimem-plasmid solution and pipette up and down once or twice using shear force to break up any clumps of cells

(15) Place suspended cells into electroporator cuvette

(16) Electroporate

   (a) Pre-set protocols

   (b) Mammalian cells

   (c) HEK293 cells

   (d) Pulse

(17) Place $\sim 10 - 20$ mL of transfected cells into the center of the imaging dishes (This varies depending on how long the cells have to grow until imaging and how confluent the dish of cells was to start with. i.e. the more cells to start with the less needed in each dish - or - the longer they have to grow the less cells in each dish)

(18) Gently vortex the dish so that the cells are evenly dispersed throughout the dish

(19) Place cells back in the incubator

A.4. Live cell imaging preparation

1. Heat the Imaging Saline in water bath at 37 °C
2. If not labeling with QDs simply rinse 3-6x with Imaging Saline and leave 1 mL of Imaging Saline on final rinse in dish for imaging.
3. If labeling with QDs prepare QD solution: 1:10000 QD in 1% BSA in Imaging Saline
    - (a) 1% (by volume) BSA and Imaging Saline
        - (i) Measure out ∼ 10 mg BSA
        - (ii) Place BSA and Imaging Saline into micro-centrifuge tube. iii. Vortex until BSA is completely dissolved.
    - (b) 1:10000 QD in 1% BSA
        - (i) 5 μL of 1:100 QD in 1% BSA in Imaging Saline
            - (A) 1 μL QD
            - (B) 100 μL Imaging Saline
            - (C) Vortex
        - (ii) 500 μL of Imaging Saline
        - (iii) Vortex
    - (c) Place QD solution in water bath.
4. Aspirate media from dish of cells and rinse 6x with Imaging Saline to remove media.
    - (a) Be careful not to suck all the media off the dish, leaving the cells dry.
    - (b) Do not suck off media from middle, suck from the sides where there are no cells.
    - (c) When rinsing do not add Imaging Saline too quickly or with too much force or directly the middle of the dish. These actions can wash away the cells.

    (d) On last rinse remove *ALL* Imaging Saline.

(5) *QUICKLY* place 500 μL of the QD solution into the dish of cells and place in the incubator for 10 minutes.
(6) Remove the QD solution then rinse 3x with Imaging Saline to remove any unbound QDs.
(7) On the final rinse leave 1 mL of Imaging Saline in the dish for imaging.

A.5. Cell fixation and labeling

In chapter 3 we used STROM images of fixed cells in order to charachterize the cortical actin structure. Here is the proocol that we used to fix the cells:

(1) Aspirate the media, fix and permeabilize the cells using $\sim$ 1000 μL of 0.3% glutaraldehyde and 0.25% Triton X-100 in cytoskeleton buffer (CB) for 1-2 min at RT (room temperature).
(2) Wash with CB three times for 5 min each at RT
(3) Add 2% Glutaraldehyde in CB for 15 min
(4) Wash with CB two times for 10 min each at RT
(5) Treat samples with $\sim$ 1000 μL of 0.1% $NaBH_4$ (freshly-prepared in PBS) for 7 min at RT to reduce background fluorescence.
(6) Wash with PBS two times, each time allowing for 5 min incubation at RT
(7) Prepare diluted Phalloidin staining solution right before use. Dilute 50 μL of the Alexa 647-Phalloidin stock solution into 1000 μL PBS and apply $\sim$ 1000 μL to each coverslip.
(8) Place the stained samples in aluminum foil wrapped container to protect from light. Incubate at 4 °C for overnight (Moisture chambers are recommended).

A.6. STORM imaging

(1) Briefly wash the fixed and labeled, with Alexa 647-Phalloidin, sample once with PBS. Immediately mount the sample for STORM imaging with GLOX imaging buffer. Glox imaging buffer preparation:
  (a) Prepare buffer A (10 mM Tris (pH 8.0) + 50 mM NaCl) and buffer B (50 mM Tris-HCI (pH 8.0) + 10 mM NaCl + 10 % Glucose)
  (b) Prepare Glox solution (250 μL):
    (i) 14 mg Glucose Oxidase + 50 μL Catalase (17 mg/ml) + 200 l Buffer A
    (ii) Vortex to dissolve Glucose Oxidase
    (iii) Spin down 14,000 rpm
    (iv) Only use supernatant
    (v) Store at 4°C for up to 2 weeks
    (vi) In case of reusing spin down at 14,000 rpm again
  (c) On ice, add 14 μL GLOX, 14 μL 2-mercaptoethanol and 1380 μL Buffer B

(2) A continuous illumination of 638 nm laser, full power, is used to excite the Alexa Flour 647.

(3) if the density of blinking fluorophores is not adequate use violet laser, with ND2 usually, to excite more fluorophores.

APPENDIX B

SOFTWARE

This appendix provides protocols used for the data analysis presented in this thesis, including single particle tracking, MSD analysis and image registration. Protocol B.5 was written in part by Xinran Xu.

B.1. Single particle tracking using u-track

Particle detection and tracking were performed in MATLAB using u-track [150]. Here is a step by step protocol to use this code for single particle tracking:

(1) Add the u-track folder and sub-folders to MATLAB directory

(2) Run the code *scriptDetectGeneral.m*

  (a) Inputs

    (i) movieParam.imageDir (the path to the folder of images to be tracked)

    (ii) movieParam.filenameBase (base name of the images)

    (iii) movieParam.firstImageNum (number of the first frame to be detected)

    (iv) movieParam.lastImageNum (number of the last frame to be detected)

    (v) detectionParam.visual (1 if want to check the detections in each frame, 0 otherwise)

    - (vi) detectionParam.alphaLocMax (between 0 and one, smaller values would detect particles with higher signal to noise ratio (SNR) and vice versa)
    - (vii) saveResults.dir (the path to the folder where the detection results would be saved)
    - (viii) saveResults.filename (name of output mat file)
  - (b) Outputs
    - (i) A mat file with detection parameters and results
- (3) Run the code *scriptTrackGeneralold.m*
  - (a) Inputs
    - (i) gapCloseParam.timeWindow (maximum number of frames allowed for gap closing)
    - (ii) gapCloseParam.mergeSplit (flag for merging and splitting, 0 for no merging and splitting of tracks and 1 for allowing merge and split)
    - (iii) gapCloseParam.minTrackLen (minimum track segment length used in the gap closing, merging and splitting step)
    - (iv) parameters.linearMotion (flag for linear motion, 0 or 1)
    - (v) parameters.minSearchRadius (minimum search radius lower limit, the distance in pixel that code search in each step to find the next position of the particle)
    - (vi) parameters.maxSearchRadius (maximum search radius lower limit, the distance in pixel that code search in each step to find the next position of the particle)

        - (vii) saveResults.dir (the path to the folder where the tracking results would be saved)
        - (viii) saveResults.filename (name of output mat file)
    - (b) Outputs
        - (i) A mat file with tracking parameters and results
- (4) Copy and paste the following into the command window directly:

  $[trackedFeatureInfo, trackedFeatureIndx, trackStartRow, numSegments]$

  $= convStruct2MatIgnoreMS(tracksfinal);$
- (5) When finished, save trackedFeatureInfo from the workplace as trackedFeatureInfo.mat
- (6) Run the code *write_trajectories_utrack.m*.
    - (a) Inputs
        - (i) A mat file output of previous step : trackedFeatureInfo
        - (ii) fid (file name that the output is saved into)
    - (b) Outputs
        - (i) A text file with tracks (XYI)

B.2. MSD analysis

In chapters 4 and 5 we use MD analysis in order to characterize diffusion. Here is a step by step protocol for calculating MSD (TA-MSD) and EA-TA-MSD:

- (1) Delete the trajectories that are shorter than some specif length using the code *FindLongTrajectories-2.vi*
    - (a) Inputs:
        - (i) XYI trajectory text file output of u-track

    - (ii) Minimum size in frames
  - (b) Output:
    - (i) Trajectories with length longer than the minimum size as a text file

(2) Run the code *MSD-UTrack-NoLastFrame.vi*
  - (a) Inputs:
    - (i) Number of intervals (number of intervals used for MSD calculations, usually one third of the minimum length used in the first step is a good number)
    - (ii) frame time (s) (movie exposure time)
    - (iii) Camera pixel size (nm)
    - (iv) XYIfile (output of UTrack). Example:
  - (b) Output:
    - (i) A text file of lengths of trajectories
    - (ii) A text file of MSDs (St Dev is the error of calculated MSD)

(3) Run the code *analyze automatic linear MSDs no first row_linear.vi*
  - (a) Inputs:
    - (i) MSD file (3.b.ii)
    - (ii) Number of points to perform the fitting on (usually 10)
    - (iii) Method of fitting (Usually least square) second column is the intercepts and the third column is the residues). Example:
  - (b) Outputs:

        (i) Diffusion coefficients text file. The first column is the diffusion coefficients, the second column is the intercepts and the third column is the residues).

(4) Run the code select and average MSDs.vi to calculate EA-TA-MSD
    (a) Inputs:
        (i) Lengths (3.b.i)
        (ii) MSDs (3.b.ii)
        (iii) Diffusion coefficients (4.b.i)
        (iv) Minimum acceptable diffusion coefficient (minimum D)
        (v) Minimum acceptable length (minimum length)
    (b) Outputs:
        (i) EA-TA-MSD
(5) Run the code *Weighted_Average_MSD.m* to calculate weighted average MSD of all your movies
    (a) Input:
        (i) Directory (path to the folder containing all (and only) EATAMSDs of different movies)
    (b) Output:
        (i) A matrix with 5 columns:
        (ii) t
        (iii) Weighted average MSD
        (iv) Standard deviation

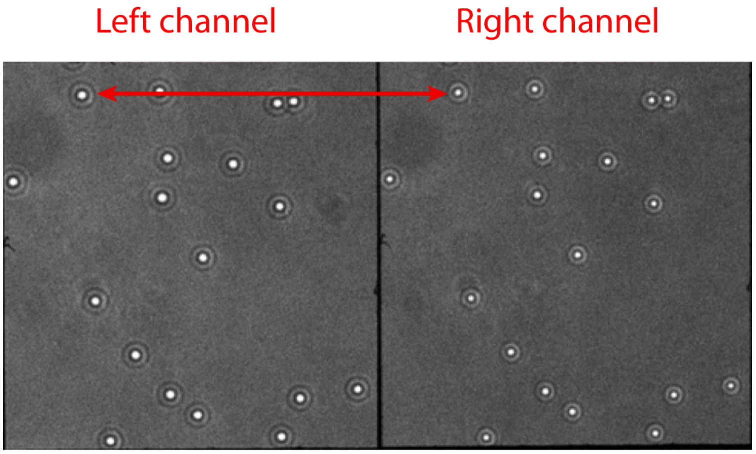

FIGURE B.1. Bead image example.

(v) Total number of tracks

(vi) Standard error of the mean

B.3. Image registration

There are different methods to register the images of two channel of the camera. In this work we registered images using bead images or white-light images.

B.3.1. Image registration using bead images.

(1) The first step in overlaying different channels is having a good white light bead image. A drop of bead solution (1-1000 of 1.7μm polystyrene beads in de ionized water) is placed on imaging dish and is dried using nitrogen gas. Quick drying is necessary so that the beads don't get aggregated. The bead image is taken only using white light in a region that has high number of well separated beads. Take the images slightly out of focus so you have two or three clear ring pattern around the beads as shown in Fig. B.1.

(2) The offset equation is found by first localizing the beads in two channel and then finding the offset between corresponding beads as a function of position in one of

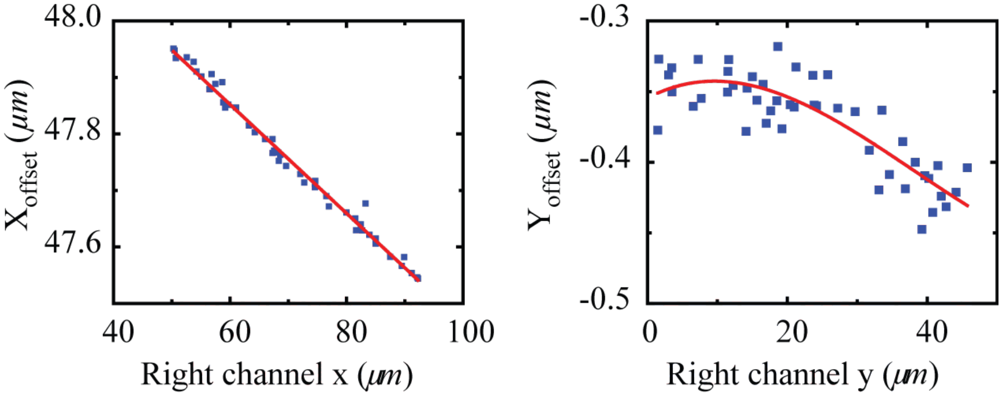

FIGURE B.2. An example of X_{offset} vs x_{right} and Y_{offset} vs y_{right} scatter plots.

the channels (right):

$$\begin{aligned} x_{\text{offset}}(x_{\text{right}}) &= x_{\text{right}} - x_{\text{left}} \\ y_{\text{offset}}(y_{\text{right}}) &= y_{\text{right}} - y_{\text{left}}. \end{aligned} \tag{50}$$

Figure B.2 shows an example of x_{offset} vs x_{right} and y_{offset} vs y_{right} scatter plot. The equation can now be found by fitting appropriate function to the offset data. We call these equations $f(x_r)$ and $g(y_r)$. Steps to calculate these equations:

(a) Open *Autocorrelation Moving multiple ROI 2- BWS v2.vi* code

(b) Drag and put the bead image folder in the input file location. Change the start frame and end of frames to what you need and ROI size to size of your beads (It should include all of the ring patterns around the bead). Run the code.

(c) Select the first bead in the left channel and click "check ROI" button then select the same bead in the right channel and check ROI and do the same steps for the other beads. Note that it is important to keep this sequence in selecting the bead: bead in left channel then the same bead in the right channel. After selecting all of the beads hit ”continue”.

   (d) The output of this code is a text file including X,Y,I of the first bead in the left channel (coordinate in nm), XYI of the first bead in the right channel, XYI of the second bead in the left channel and so on.

   (e) Open the MATLAB code (find-offset.m). Use the output of the previous code as input and change the ROI size to what you have used in step 2 and camera pixel size to your camera pixel size. Output of this code is X-offsets vs x-right and Y-offsets vs y-right. The output also shows a equation for fit to x-offsets and the average value of Y-offset. You could use the output text files to find the best fit (for example in Origin) or use the output values of the code for mean Y-offset and X-offset equation. For my case because I had a parabolic shape in my Y-offset data I used a polynomial fit $Ay^2 + By + C$ and a linear fit for X-offset.

(3) If the image has height=h and width=w pixels, then we split the image such that right and left channels has height=h and width=$w/2$. I used ImageJ software to perform this part, steps:

   (a) Import the two channel images to ImageJ

   (b) Open Cairn Image Splitter (Instructions to install this plugin

   (c) draw a rectangle with these coordinates: width=w/2, height=h, X coordinate=0, Y coordinate=0. (To make a rectangle in ImageJ: Edit¿selection¿specify)

   (d) Click on ”select first channel” button in Cairn plugin.

    (e) Draw another rectangle with the same height and width as first rectangle and X coordinate=w/2 and Y coordinate=0.
    (f) Click on "select second channel" button in Cairn plugin. Then click OK in the plugin.
    (g) three set of images will appear: first channel, second channel and overlay of these two channels. Save the first and second channel image sequence.
    (h) detect and track the particles in two channels using Utrack software as usual.

(4) Run the LabVIEW code to perform this part: *offset correction.vi*. Input for this code is XYI trajectory files of the particles in the right channel and parameters from offset equation: A,B,C from Y-offset equation and x-offset-slope, x-intercept from X-offset equation and total width of the images before splitting (w) divided by two. The output is offset corrected trajectories of the right channel trajectories.

B.3.2. Image registration using white-light images.

(1) take a two channel white light image of the cell prior to experiment, then perform the experiment without changing any camera alignment. Repeat this for every imaged cell.
(2) Open the white-light image in imageJ and divide to half and save each half (right and left)
(3) Open the movie that is going to be registered based on this white-light image in imageJ, divide to half and save each half (right and left halves)
(4) Run the code *ImageRegistration.m*
    (a) Inputs:

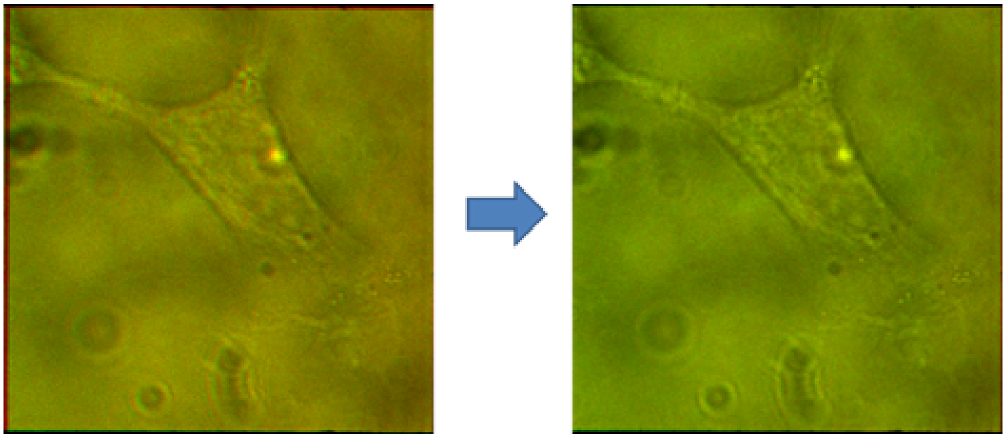

Figure B.3. Image registration using white-light images. Left: overlaid right and left channels, in green and red colors, of a white-light image of a cell before image registration. Right: overlaid right and left channels, in green and red colors, of white-light image of the same cell after image registration.

    (i) Fixed (the left half of the white-light image, tif)
    (ii) Moving (the right half of the white-light image, tif)
    (iii) Fname (path to the right half of the movie to be registered based on the white-light image)
    (iv) outputMovieName (.tif) (Name for registered right half of the movie)
    (v) outputDICimageName (.tif) (Name for the registered right half of the white-light image)
    (vi) optimizer parameters (you can change these parameters if image registration does not look good enough)

(b) Outputs:
    (i) An image of the left and right channels of the white light image along with the overlaid image before and after image registration
    (ii) Registered right half of the movie (tif)
    (iii) Registered right half of the white-light image

Note: I usually overlay the left half of the white-light image with the registered right half in imageJ to make sure the code works fine as shown in Fig. B.3 (you could also to compare it to the overlaid image of left half and right half before image registration)

B.4. PALM reconstruction

This is for the purpose of creating a reconstructed PALM image using raw TIRF images.

(1) Run the code *BuildRC8input.m* which converts the tiff files to reconstruction code input
   (a) Inputs
      (i) folder_path (path to the tiff files folder)
      (ii) tif_file (tif image name)
      (iii) ROI (size of the tiff file)
   (b) Outputs
      (i) A mat file that is the input for the next step

(2) Run the code *SR_demo_Sanaz_RC8.m*
   (a) Inputs
      (i) movie_path (path to save the reconstructed movie)
      (ii) movie_name (name of the output reconstructed movie)
      (iii) palm_frames (number of frames used in reconstruction)
      (iv) palm_gap (number of gap frames)
      (v) frameEnd (end frame for reconstruction)
      (vi) x and y offsets (from bead based image registration code)

        (vii) FileList (mat file output of the previous step)

    (b) Outputs

        (i) reconstructed movie

B.5. STORM reconstruction

(1) Install ThunderSTORM plugin if needed (*http://zitmen.github.io/thunderstorm/*).

(2) Open the movie in imageJ.

(3) open the ThunderSTORM plugin (Plugins-ThunderSTORM-Run Analysis)

(4) Click“Camera setu” at the top of “Run Analysis”, and choose the correct EM Gain for the analysis.

(5) In the “Run Analysis” tab, make sure the correct parameters are chosen. Wavelet filter is recommended with order 3 and scale 2. Gaussian is chosen for sub-pixel localization of molecules. For connectivity 8-neighbourhood is recommended.

(6) After all of the Run Analysis settings are configured, hit OK at the bottom to start reconstruction. (Depending on RAM usage, this could take anywhere from 20 to 40 minutes).

(7) After the initial reconstruction is finished, a results table should appear with options at the bottom. These are settings that are used in post processing, and some will be utilized. Before any post processing is done, “Export” the original data table to the desired folder.

(8) The first step in post processing is to “remove duplicates” from the data. The distance threshold that is used is “uncertainty”.

(9) The next step in post processing is drift correction, which is under the Drift Correction tab.

(a) When correcting the drift, either “Cross correlation” or “Fiducial marker” method is used. “Cross correlation” if there id no bead image and Fiducial markers if you have a bead image.

(b) With cross correlation selected, select “>>” just to the right, and a tab will appear. This is used to select the number of bins for drift correction and the magnification used in reconstruction. Hit “Apply” and observe the change of the preview of reconstruction which displays automatically after the drift correction. Sometimes, there are some artifacts occur even though you have right drift curve. In that case, the try other bin values, otherwise avoid any drift correction.

(c) With fiducial markers method selected, select “>>” just to the right, and a tab will appear. “Max distance” controls the lateral tolerance for identification of a marker. “Min marker visibility ratio” controls the fraction of frames wherein the molecule must be detected to be considered as a fiducial marker. “Trajectory smoothing factor” controls smoothness of the drift trajectory. Typical values for these three parameters are 50, 0.1, 0.25 separately.

(d) The final post processing step is to merge the data. This is simply done hitting the “Merge” tab and selecting Merge.

(e) Now, export this post-processed results table just like the original.

(f) After the second export, hit “Visualization” on the bottom of your post-processed results table.

(g) Save the image that is produced from the visualization as a Tiff file in the same folder as the exported result tables.

B.6. Generating Mittag-Leffler distribution

In chapter 3, I compared my experimental data to the Mittag-Leffler distribution. Probability density function of this distribution is [see equation 7 of the reference [90]]:

$$f(x) = \frac{\Gamma^{1/\alpha}(1+\alpha)}{\alpha x^{1+1/\alpha}} l_\alpha \left[\frac{\Gamma^{1/\alpha}(1+\alpha)}{x^{1/\alpha}} \right], \tag{51}$$

where α is the distribution parameter, $\Gamma(s)$ is the gamma function and $l_\alpha(t)$ is the one-sided Lévy stable PDF. I wrote a code called *ML.m* in MATLAB which generates this distribution for a given α value:

```
% ML code
N=190;
 alpha=0.8;
x=0.01:0.01:2.5;
A=(gamma(1+alpha)^(1/alpha))/alpha;
 [Q,M]=size(x);
 for  i=1:M
B(i)=A/(x(i)^(1+1/alpha));
Lx(i)=(gamma(1+alpha)^(1/alpha))*(1/x(i)^(1/alpha));
C(i)=levy(Lx(i),N,alpha);
MLD(i,1)=B(i)*C(i);
end
```

```
% Code for the levy function
function [y] = levy(x,N,alpha)
Levy=0;
for j=1:N
l(j)=((-1)^(j+1)/(factorial(j)*x^(1+alpha*j)))*gamma(1+alpha*j)*sin(pi*alpha*j);
Levy=Levy+l(j);
end
y=Levy/pi;
end
```

B.7. Box counting fractal dimension

This protocol is for calculating the Hausdorff dimension for the PALM images of actin with box counting method.

(1) Reconstruct the PALM movie (reconstruction protocol)
(2) Open the reconstructed movie in ImageJ
(3) Convert to 8bit
(4) Crop the image and save the ROI and cropped image (if necessary)
(5) Subtract the background in ImageJ (process-subtract background)
(6) Save the image as tif file
(7) Run the code: *DetectActinStructure.m* to threshold the image and save the image
    (a) Inputs:

        (i) Filtered reconstructed 8bit actin image (output of step 6)
        (ii) Threshold value ($0 < th < 1$)
    (b) Outputs:
        (i) Binary actin image

(8) Run the code: *FractalDimension.m* to calculate the fractal dimension using box counting method
    (a) Inputs: Binary filtered reconstructed 8bit actin image (output of step 7)
    (b) Outputs: Fractal dimension

B.8. Turning angle distribution

In chapter 4 the turning angle distribution was used to probe the anti-correlation in motion. Here is a step by step protocol for calculating the distribution.

(1) Put all the trajectory text files (output of UTrack) of all the movies that need to be included in the turning angle analysis in one folder.
(2) Run the turn_angles.m code
    (a) Inputs:
        (i) Directory (to the folder created at step 1)
        (ii) Delta (a matrix of the lag times in frames to calculate the turning angles)
    (b) Outputs:
        (i) Text files for the turning angles for every entry of delta. Note: I have noticed that when I run the code for all of the movies at the

same time it introduces a lot of zeros in the turning angles but it does not happen if run the code separately for each movie.

(3) Import the turning angle file one by one to an origin file.

(4) Compute the PDF:

   (a) Select the angles column and compute the frequency count: statistics-frequency count open dialog. Then use these parameters (you could play with parameters until results are satisfying)

      (i) Specify Binning range by = Bin centers

      (ii) Minimum bin beginning = 5

      (iii) Maximum bin center = 175

      (iv) Bin size = 10

      (v) And add relative frequency to quantities to compute.

   (b) Calculate the PDF by dividing the relative frequency by bin size.

B.9. MSD vs distance from actin

In chapter 4 the MSD versus distance from actin was used to show the confinement of the membrane proteins within the actin domains. Here is a step by step protocol for calculating the MSD vs distance from actin.

(1) Run the code *DisplacementVsDistanceFromActin.m*

   (a) Inputs:

      (i) EDM file (from actin, output of EDM_Sanaz.m with th=0.01)

      (ii) Tracks (output of utrack)

        (iii) sliding_time_window (sliding time window used for original PALM movie)
        (iv) PALM end frame number
        (v) pixel_size=13; (nm (in the reconstructed movie))
        (vi) delta (time lag to calculate the displacement (in frames), the code calculates the
        (vii) displacement and also the average EDM and MAX EDM during these number of frames)
    (b) Output:
        (i) A text file of displacement, average EDM and maxEDM.
(2) Then I calculate the 3D histogram of square displacement vs maxEDM in origin. Finally for each EDM I calculate the weighted average square displacement (the counts are the weights)

B.10. Obtaining Kv2.1 cluster intensity and morphological properties using ImageJ

In chapter 6 we compared the kv2.1 cluster size before and after blebbistatin treatment. Here is step by step protocol to find cluster intensity and morphological properties:

(1) Detect clusters:
    (a) Open the Kv2.1 cluster image in ImageJ
    (b) Convert to 8 bit
    (c) Save the image as tif file
    (d) Run the code *ClusterDetection.m*
        (i) Inputs

        (A) 8 bit cluster image
        (B) Output file name
        (C) Threshold value (between 0 and 1)
    (ii) Output
        (A) Detected cluster image (tif)

(2) Create non-binary cluster image:
    (a) Open both detected cluster image and the 8 bit raw cluster image in ImageJ
    (b) Divide the detected cluster image by 255 to make sure that the clusters in the detected image have intensity equal to 1 and everywhere else is zero.
    (c) Multiply the detected binary image with the raw image (Process-Image Calculator-Multiply (Create new window))

(3) Analyze clusters:
    (a) Duplicate the non-binary cluster image. Threshold one of the images. We duplicate the image so that the binary mask that we create from the copy can be used to sample the original image to obtain intensity.
    (b) Invert the thresholded image so that the clusters be zero and everywhere else 255 (Edit-Invert) and then convert to binary (Process-Binary-Make Binary).
    (c) Select "Set Measurements" to tell ImageJ what data to collect. For example area and intensity. "Redirect To" instructs ImageJ to use the ROI data from the binary image, but gather intensity values from a different window. In this case the non-binary cluster image.
    (d) Select "Analyze Particles" and fill in the remaining required information.

    (e) Click “OK” and the ImageJ finds the ROIs on the original image and generates a data results window.

B.11. Separating tracks to on and off clusters

In chapter 6 we separated the membrane protein track to inside, “on”, or outside “off” Kv2.1 clusters. Protocol to perform this separation:

(1) Register the Kv2.1 cluster movie using white light image registration method described in section B.3.2.

(2) Detect Kv2.1 clusters:
    (a) Open the registered Kv2.1 cluster movie in image J.
    (b) Average every 50 frames in image J (Image-stacks-tools-Grouped Z project-group size is 50)
    (c) Convert to 8 bit.
    (d) Save the averaged movie.
    (e) In the averaged image using freehand selection tool make a ROI around the cell.
    (f) Save the ROI (Analyze-tools-ROI manager-save)
    (g) Clear outside the ROI (Edit-Clear outside)
    (h) Save the image as tif.
    (i) Run the code *ClusterDetection2.m*
        (i) Inputs
            (A) The averaged registered Kv2.1 cluster movie
            (B) Output File Name
        (ii) Outputs:

            - (A) Detected Cluster movie
    - (j) Open the filtered image in image J and also the ROI and clear outside then save with the same name.
- (3) Track the membrane protein movie (BAR or CD4)
    - (a) Open the protein movie in image J
    - (b) Open the saver ROI and clear outside
    - (c) Save the movie (Save as image sequence)
    - (d) Detect and track using U-Track
- (4) Separate tracks to on/off cluster
    - (a) Run the code *SeperateTracks-on-off-clusters-2.m*
        - (i) Inputs
            - (A) Fname (Averaged, registered, cleared, detected Kv2.1 clustter movie)
            - (B) tracks-file (output of U-Track)
            - (C) N (number of frames that the cluster movie was averaged)
        - (ii) Outputs
            - (A) An image showing the on/ off cluster tracks along with clusters (for the first N frames) and percentage of channels on clusters and the same image but with corrected orientation.
            - (B) Two text file of tracks on and off clusters.